

Source Driven Transient Natural Convection In Enclosures

by

Douglas T. Reindl

A thesis submitted in partial fulfillment of the  
requirements for the degree of

Doctor of Philosophy  
(Mechanical Engineering)

at the

UNIVERSITY OF WISCONSIN-MADISON

1992

## Acknowledgements

Several people have contributed to this work in one way or another. The Professors in the Solar Energy Laboratory have, by far, been key contributors and deserve a great deal of credit. In addition to being an outstanding teacher, Sandy Klein has made my life easier by writing software programs like EES and FEHT. Sandy was also more than willing and able to help when roadblocks in my work came up. I feel fortunate to have had John Mitchell as one of my advisors. John always has ideas and useful suggestions in tackling problems. He is an excellent motivator and has maintained a great deal of interest in this work. I would like to extend a special thanks to my major advisor Bill Beckman. It has truly been, not only a rewarding experience working with you over the past five years but also, a pleasure. I like Bill's aggressive attitude toward teaching and research as well as his accurate a priori predictions of results. In addition to work, we have also played quite a few rounds of golf and I think Bill may have the edge in the win column but not by many. You and Sylvia were very hospitable hosts during our visit to France. We had a fantastic time.

Bill, John, and Sandy you all have taught me a great deal! Thanks.

The Solar Energy Lab is quite an interesting place. During my stay at the lab, I have gotten to know a lot of the students. A good deal of credit goes to the current and former students that have made the lab not only liveable but an enjoyable place to work. Some of the many students that helped me in one way or another include: Tim, Mark, Harald, Manni, Blake, Frank, Juergen E., Florian, Justus, Todd, Eberhard, Paul K., Mark R., Ruth, Chris W., Alte, Jim K., Paul R., Martin, Jim S., Bob S., Dean, Osama, Krista, Robert L., Osman, Steve E., Bob G., Jurgen G., and Jorg. Thanks to my office partner and the current TRNSYS engineer, Jeff Thornton. Whether it's golfing, water skiing, playing basketball, or spring turkey hunting we

have had some great times. It was helpful to have someone around the lab, like Dick Boor, with a work ethic similar to mine and the ability to share ideas on projects or whatever. I would also like to acknowledge Nate Blair for his help on the experiments and flow visualization work during the tail end of this project. Finally, I would like to thank Shirley Quamme for having the expertise on how to get things done in a bureaucratic University.

A great deal of credit goes to a friend and colleague Gerald Matranga. After all, Jerry was the one who got me started in the first place and you never get anywhere unless you start.

My family has always been a very important part of my life. Much of my personal success and achievement is a consequence of a close family. I would like to thank my Mother and Father for their support in all of my work. You both have been exemplary role models and always there. I am blessed with four great brothers and sisters who have always had a positive influence on me. You will probably never know how important you have been. Last, but definitely not least, I would like to thank my wife Reneé. Thanks for putting up with me over the last five years, I love you.

This work has been supported by the Solar Applications for Buildings, Conservation and Renewable Energy Division, U. S. Department of Energy. Computational resources have been provided by the San Diego Supercomputer Center.

## Abstract

The transient heat transfer and fluid dynamic response from a heat source in two different geometric enclosures is analyzed. The first configuration is a vertical flat plate in a rectangular enclosure (a geometry arising in many electronic packaging configurations) and the second configuration is a coiled tube heat exchanger immersed in a cylindrical enclosure (a geometry that is found in many thermal storage strategies). The research is a combination of numerical, analytical, and experimental work. The numerical aspects consider solving the time dependent Navier-Stokes and energy equations by a finite element method. Experiments are performed to assess the applicability of assumptions made in the numerical models.

In the first geometric configuration, an adiabatic rectangular cavity encloses an isothermal vertical flat plate heat source. The initial condition is an isothermal quiescent flow field with a step change in plate temperature. As the initial step change in source temperature begins to influence the flow field, the heat transfer from the plate progresses through three distinct temporal regimes: pure conduction, quasi-steady, and decay. Heat transfer during the first two regimes compare well with the limiting cases of pure conduction and infinite medium solutions, respectively. Scale analysis techniques are used to predict the temporal transition points separating the three heat transfer regimes as well as identifying appropriate parameters to correlate the heat transfer during the decay period. The result is a complete piecewise correlation of the transient heat transfer from a vertical plate in an enclosure.

The second configuration is a cylindrical enclosure with an isothermal circular coil heat source. The boundary conditions are similar to those considered for the rectangular

cavity with a heated vertical flat plate. The temporal behavior of the heat transfer from the circular coil is analogous to the vertical flat plate configuration. Scale analysis techniques are again used to determine the transition points between the three heat transfer regimes and identify the relevant parameters to correlate the decay period heat transfer.

An experimental apparatus was constructed in an effort to validate the numerical computations performed on the cylindrical enclosure geometry. The apparatus consisted of a borosilicate based glass cylinder with a toroid shaped heat source. The heat source (powered with an electrical resistance heating element) is maintained at a constant temperature by varying the power supplied heating element. The derived quantities include: ambient temperature, energy supplied to the heat source, surface temperature of heat source, average Nusselt number from heat source, and bulk temperature of fluid in the enclosure. A unique method for "measuring" the enclosure bulk temperature has been established.

The behavior of the transient heat transfer response observed in the experimental apparatus was different from that in the numerical computations. The measured heat transfer appeared to follow a single regime, decay (conduction regime data were not taken). Applying the group of parameters identified by scale analysis to correlate the decay period yielded agreement with the measured heat transfer response.

## Table of Contents

Acknowledgements .....	i
Abstract .....	iii
List of Figures .....	vii
List of Tables .....	xi
Nomenclature .....	xii
Chapter 1 Introduction .....	1
1.1 Literature Survey .....	2
1.1.1 Steady State Configurations .....	2
1.1.2 Transient Configurations .....	6
1.2 Research Objectives .....	14
Chapter 2 Vertical Flat Plate In A Rectangular Enclosure .....	20
2.1 Governing Equations for Rectangular Enclosure .....	20
2.2 Solution Technique .....	24
2.3 Results .....	35
2.4 Conclusions .....	63
Chapter 3 Coiled Tube In a Cylindrical Enclosure .....	67
3.1 Governing Equations for Cylindrical Enclosure .....	69
3.2 Results .....	72
3.2.1 Limiting Cases .....	74
3.2.2 Scale Analysis .....	78
3.2.3 Flow Field Results .....	85

3.3 Conclusions .....	88
Chapter 4 Experimental Analysis .....	92
4.1 Determining Average Nusselt Number and Bulk Temperature .....	93
4.2 Experiment Configuration .....	98
4.2.1 Design .....	98
4.2.2 Data Acquisition and Control Systems .....	103
4.2.3 Assumptions .....	111
4.3 Uncertainty Analysis .....	122
4.4 Results .....	131
4.4.1 Constant Heat Flux Source .....	131
4.4.2 Constant Temperature Source .....	138
4.5 Conclusions .....	149
Chapter 5 Conclusions and Recommendations .....	153
5.1 Conclusions .....	153
5.1.1 Vertical Flat Plate In A Rectangular Enclosure .....	153
5.1.2 Coil Tube In A Cylindrical Enclosure .....	155
5.1.3 Experimental Analysis .....	156
5.2 Recommendations .....	157
5.2.1 Vertical Flat Plate In A Rectangular Enclosure .....	157
5.2.2 Coil Tube In A Cylindrical Enclosure .....	158
5.2.3 Experimental Analysis .....	161

## List of Figures

Figure 1.1: Differentially heated square cavity. ....	3
Figure 1.2: Adiabatic cavity with one sidewall heated/cooled. ....	9
Figure 1.3: Transient response of $\overline{Nu}$ from Nicolette, et al. (1985). ....	11
Figure 1.4: Transient response of $\overline{Nu}$ from Hall, et al. (1988). ....	11
Figure 1.5: Adiabatic cavity with a heated vertical plate source .....	12
Figure 1.6: Concentric isothermal cylinders used by Charmichi and Sparrow (1985) .....	13
Figure 1.7: Single coil tube in cylindrical enclosure configuration. ....	15
Figure 2.1: Computational domain for the rectangular enclosure with a flat plate. ....	20
Figure 2.2: General computational domain. ....	27
Figure 2.3: Master and actual element in computational domain. ....	33
Figure 2.4: Typical mesh for square cavity with a heated vertical flat plate. ....	36
Figure 2.5: Transient $\overline{Nu}$ for various relative plate sizes. ....	37
Figure 2.6: Transient response of $\overline{Nu}$ and $\overline{Nu}_m$ . ....	39
Figure 2.7: Mean cavity temperature for $Ra=10^6$ . ....	40
Figure 2.8: Transient $\overline{Nu}$ including pure conduction solutions for a range of Rayleigh numbers. ....	41
Figure 2.9: Transient $\overline{Nu}$ including infinite medium solutions for a range of Rayleigh numbers. ....	43
Figure 2.10: Scale analysis estimates for the conduction dominated regime. ....	46
Figure 2.11: Scale analysis estimates for the quasi-steady regime. ....	48

Figure 2.12: Piecewise heat transfer approximation results. ....	52
Figure 2.13: Stream function contours at ( $t^*=5.5$ ). ....	54
Figure 2.14: Temperature contours at ( $t^*=5.5$ ). ....	55
Figure 2.15: Stream function contours at end of quasi-steady regime. ....	56
Figure 2.16: Temperature contours at end of quasi-steady regime ....	57
Figure 2.17: Effect of vertical plate position on heat transfer. ....	58
Figure 2.18: Velocity vectors at $t^*=5.0$ and $\eta=0.25$ . ....	61
Figure 2.19: Velocity vectors at $t^*=5.0$ and $\eta=0.75$ . ....	62
Figure 3.1: Computational domain for cylindrical enclosure. ....	70
Figure 3.2: Axi-symmetric mesh for cylindrical enclosure. ....	73
Figure 3.3: Transient heat transfer for $Ra_D=10^5$ . ....	74
Figure 3.4: Transient heat transfer including pure conduction for all $Ra_D$ . ....	75
Figure 3.5: Transient heat transfer including Morgan correlation for all $Ra_D$ . ....	78
Figure 3.6: Scale estimates for duration of conduction dominated regime.....	80
Figure 3.7: Scale estimates for duration of quasi-steady regime. ....	82
Figure 3.8: Piecewise heat transfer for cylindrical enclosure. ....	84
Figure 3.9: Transient bulk temperature response for $Ra_D=10^4$ . ....	85
Figure 3.10: Contour maps at $t^*=61$ . ....	86
Figure 3.11: Contour maps at $t^*=101$ . ....	87
Figure 3.12: Contour maps at $t^*=141$ . ....	88
Figure 4.1: Experimental enclosure layout. ....	93
Figure 4.2: Temperature-specific volume behavior for water. ....	97
Figure 4.3a: Experimental enclosure (isometric). ....	99

Figure 4.3b: Experimental enclosure (cross-section). .....	100
Figure 4.4: Circular heat exchanger design. ....	102
Figure 4.5: Data acquisition system. ....	104
Figure 4.6: Capacitance probe with improper response. ....	107
Figure 4.7: Acceptable capacitance probe response. ....	108
Figure 4.8: Response from time-proportional control strategy. ....	109
Figure 4.9: Typical coil current from analog-proportional control strategy. ....	111
Figure 4.10: Temperature effect on combined fluid properties. ....	112
Figure 4.11: Temperature dependent fluid properties effect on $Ra_D$ . ....	113
Figure 4.12: Effect of property variations on $\overline{Nu}$ . ....	115
Figure 4.13: Ideal (black) body spectral intensity at $T=313K$ . ....	117
Figure 4.14: Spectral absorption coefficients for water. ....	118
Figure 4.15: Cool down data for insulated enclosure. ....	121
Figure 4.16: Bulk temp as a function of probe output. ....	122
Figure 4.17: Heat loss coefficient dependence on bulk temperature. ....	131
Figure 4.18: Energy balance with constant flux for acrylic enclosure. ....	133
Figure 4.19: Apparent bulk temperature for acrylic enclosure with and without insulation and a constant flux heat source. ....	134
Figure 4.20: Capacitance probe response during initial cool down. ....	136
Figure 4.21: Bulk temperature by measurements and energy balance with constant flux heat source (Duran <sup>®</sup> enclosure). ....	137
Figure 4.22: Typical, measured heat exchanger surface temperature. ....	139
Figure 4.23: Finite element mesh for experimental geometry. ....	140
Figure 4.24: Repeatability of the bulk temperature response. ....	141

Figure 4.25: Experimental results for $\overline{Nu}$ by measured current and time rate change in bulk temperature. ....	142
Figure 4.26: Shadowgraph setup. ....	144
Figure 4.27: Shadowgraph results.....	146
Figure 4.28: Measured and correlated heat transfer response. ....	148
Figure 4.29: Measured and correlated bulk temperature response. ....	149

## List of Tables

Table 2.1: Rectangular geometry variable non-dimensionalization .....	21
Table 2.2: Constant for Equation 2.51 with $\phi = 0.5$ and $\eta = 0.5$ . .....	51
Table 2.3: Average Constant for Equation 2.51 with $\phi = 0.5$ and $10^4 \leq Ra \leq 10^6$ . .....	59
Table 2.4: Maximum $v$ -velocitys for $Ra=10^6$ and the three vertical plate positions. ....	60
Table 3.1: Cylindrical coordinate variable non-dimensionalization .....	71
Table 3.2: Range of $\overline{Nu}$ compiled by Morgan (1975). .....	76
Table 3.3: Current Nusselt numbers with Morgan (1975) and Churchill & Chu (1975). .....	77
Table 4.1: Enclosure properties. ....	101
Table 4.2: Variable property peak velocity results. ....	115
Table 4.3a: Compilation of individual bias errors. ....	128
Table 4.3b: Compilation of individual precision errors. ....	129

## 1 Introduction

By nature, convection heat transfer results from the transport of energy by fluid flowing past an object of interest. The solution of convection problems require knowledge of both the dynamics of fluid flow and energy transfer. Convective heat transfer processes are usually subdivided into three regimes depending on the behavior of the fluid flow: forced, natural, and mixed. Forced convection occurs when the fluid flow past a surface is induced by external devices e.g., a pump. In this case, the inertia forces in the fluid flow field dominate the buoyancy forces and the required fluid flow field can be solved independent of and prior to solving the heat transfer problem (assuming constant fluid properties); thereby, reducing the complexity of numerical or analytical solutions.

In natural convection, the fluid flow is driven by the imbalance of body forces which result from the difference of hydrostatic pressure imposed on a fluid element and the weight of the fluid element. As the temperature (or concentration) in the fluid changes, density (and consequently the weight) of a fluid element changes. The resulting imbalance of pressure and weight forces sets the fluid in motion. The mutual dependence of fluid flow on temperature results in coupling the fluid flow with the energy transfer. Numerically, this imbalance produces a strong coupling between the governing differential equations for heat transfer and fluid flow and simultaneous solutions are necessary. In a mixed convection regime, both buoyancy and inertia forces are important.

Natural convection heat transfer has received considerable attention in the literature over the past years due to its importance in a number of physical processes. Some applications in which natural convection is a dominant feature include solar energy (collectors, ponds, and thermal storage), cooling of electronic equipment, building heat

transfer, and environmental processes (weather dynamics, geothermal reservoirs, etc.).

The broad class of natural convection problems encompass both steady state and time dependent configurations for bounded (enclosure) and unbounded (external) flows. There exists a large body of literature investigating external natural convection problems. Analysis of external flow problems have a distinct advantage over internal problems due to assumptions (e.g., boundary layer) which can significantly simplify the governing differential equations. For simple geometries and boundary conditions, similarity solutions can be found. In the case of bounded or enclosure problems, solutions by traditional boundary layer assumptions are not possible due to the absence of known matching conditions outside the boundary layer. Thus, the full system of governing equations must be solved simultaneously which greatly complicates the analysis.

## **1.1 Literature Survey**

The following section summarizes previous investigations of natural convection in enclosures. Both steady and transient configurations using numerical and experimental techniques are considered.

### **1.1.1 Steady State Configurations**

The simplest and one of the most comprehensively studied enclosure problems is a two dimensional rectangular cavity with differentially heated side walls and adiabatic top and bottom (also known as the double glazing problem) as depicted in Figure 1.1.

In one of the earliest studies of this problem, Batchelor (1954) considered cavities with a large range of aspect ratios ( $A = H/W$ ). The study showed that various flow regimes exist depending on the magnitude of the Rayleigh number ( $Ra = \text{buoyant forces} / \text{viscous and thermal forces}$ ,  $g\beta H^3(T_h - T_c)/\nu\alpha$ ). When  $Ra$  is small ( $Ra < 1708$ ) or the cavity slender

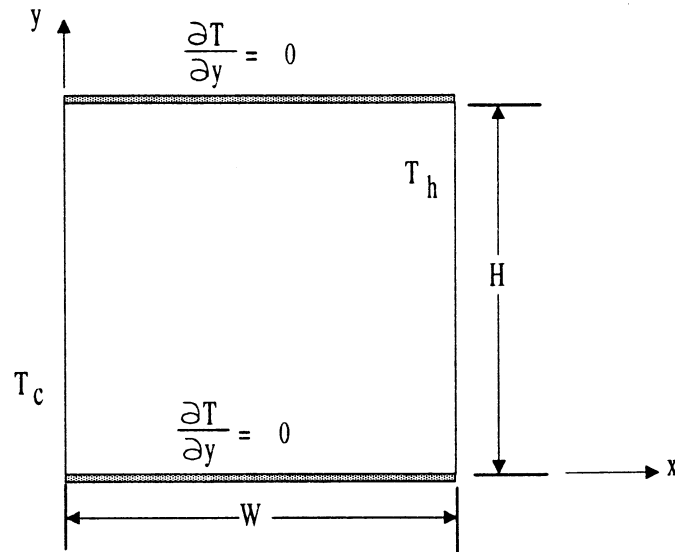


Figure 1.1: Differentially heated square cavity.

( $W \ll H$ ), the heat transfer across the cavity is dominated by pure conduction. For large  $Ra$ , the near wall region was assumed to be boundary layer flow with the matching condition outside the boundary layer obtained by assuming that the remaining core flow is isothermal with a constant vorticity. Batchelor was unable to obtain solutions for the large  $Ra$  number case (solutions were obtained later by Potts (1958)). Expressions for Nusselt number  $\overline{Nu}$  (a dimensionless average heat flux) were approximated by a power series in  $Ra$  for both limiting cases. Later experiments performed by Eckert and Carlson (1961) showed the core to be stratified which negated the isothermal core assumption used by Batchelor. The large deviations in comparing the  $\overline{Nu}$  results of Batchelor to Eckert and Carlson may be explained by the assumptions made regarding core behavior.

More recently, Han (1979) used a stream function - vorticity (SFV) formulation with central differences on a uniform grid and successive over relaxation (SOR) to solve the full set of governing equations for the enclosure problem shown in Figure 1.1. Solutions

for Nusselt numbers were obtained over a wide range of aspect ratios  $1 \leq A \leq 20$ , and Prandtl numbers ( $0.5 \leq Pr \leq 10000$ ) for  $Ra \leq 10^5$ . Temperature profiles were in good qualitative agreement with the measurements of Eckert and Carlson. Nusselt number results were within 25% of the experimental results.

Jones (1979a) used a SFV formulation to solve the cavity problem over a smaller range of aspect ratios ( $1 \leq A \leq 20$ ) and a similar range of Rayleigh numbers ( $1.94 \times 10^3 \leq Ra \leq 2.3 \times 10^5$ ). Computed temperature profiles and streamlines were in agreement with the experiments of Duxbury (1972). Comparison of average Nusselt numbers were within 13% of the Duxbury experiments. Jones (1979b) suggested that the differentially heated square problem would be suitable for validating and testing new computer codes and numerical techniques prompting a large scale computational comparison exercise by de Vahl Davis and Jones (1983a). Thirty contributors submitted solutions to the cavity problem with a unity aspect ratio and  $10^3 \leq Ra \leq 10^6$ . Various calculated and derived quantities, such as maximum stream function, velocity components, etc., were selected to be included in the comparison. An attempt to determine the "right" solution was performed by de Vahl Davis (1983b) solving a SFV formulation using refined grids ( $11 \times 11 \rightarrow 81 \times 81$  uniform meshes) and Richardson extrapolation. The solution was considered a benchmark solution and all other results submitted in the exercise were compared with this benchmark. Significant differences existed between solutions submitted and the benchmark solution. For example at  $Ra = 10^6$ , variations in the average Nusselt number ranged from -6.9 to +20% when compared to the benchmark. The differences in average Nusselt numbers were smaller at lower Rayleigh numbers. The

primary reason is because accurate solutions to the governing equations can be obtained on relatively coarse meshes at low Rayleigh numbers since the problem is largely conduction dominated throughout the entire transient.

Betts and Haroutunian (1983) used high order triangular finite elements to solve a SFV formulation to the square cavity problem. Average Nusselt number results compared within 1.5% of the benchmark solution obtained by de Vahl Davis. Several other finite difference solutions using stream function - vorticity formulations have been published (Ozoe, et al. 1985; Lin and Nansteel, 1987; and Chen, et al. 1987). Fewer primitive variable formulations to the cavity problem have been published<sup>1</sup>. (The primitive variables are  $u$ ,  $v$ ,  $P$ , and  $T$ .) Markatos and Pericleous (1984) use an upwind difference scheme to solve the governing equations in primitive variable form. A version of the semi-implicit pressure linked equation (SIMPLE) algorithm, Patankar (1972), is used to obtain a pressure field such that the corresponding velocities satisfy mass conservation. Turbulent calculations were also performed using a ( $k\sim\epsilon$ ) model when  $Ra > 10^6$ . Good agreement with the benchmark solution was obtained for the laminar case ( $\overline{Nu}$  results are within 2.5% of benchmark). Correlations were established for both the laminar and turbulent cases. Marshall, et al. (1978) used a primitive variable penalty function approach to solve the steady problem for  $Ra$  up to  $10^7$ . Over the same range as de Vahl Davis, the  $\overline{Nu}$  compared within 7% of the benchmark. The relatively large difference may be attributed to a relatively coarse mesh (64 quadratic quadrilateral elements).

---

1 The advantages and disadvantages of the stream function - vorticity versus the primitive variable formulation will be discussed in Section 2.2.

All of the work discussed thus far exclusively considered steady state solutions. The number of studies dealing with transient natural convection in similar geometries is much more limited. In some cases (e.g. Newell and Schmidt, 1970), time dependent formulations of the governing equations are solved when only steady state solutions are desired. Thus, no attempt is made to achieve temporal accuracy and features unique to the transient heat transfer and fluid flow are not observed.

### 1.1.2 Transient Configurations

One of the first studies to consider the transient behavior of the differentially heated cavity is that of Wilkes and Churchill (1966). The boundary conditions are identical to those shown in Figure 1.1; in addition they considered a linear temperature variation for the horizontal surfaces. The initial condition is a quiescent flow field at a temperature equal to the average of the hot and cold vertical surfaces. An alternating direction implicit (ADI) technique was used to solve the parabolic vorticity and energy equations while the SOR technique is used to solve the Poisson equation for stream function. Deviations in the average Nusselt numbers at steady state are as high as 43% when compared to the de Vahl Davis (1983b) benchmark. The most likely source of this large deviation from the benchmark solution is a lack of appropriate grid refinement. (The finest mesh size used is a 20x20.) Qualitatively, the transient response of  $\overline{Nu}$  follows a pure conduction solution at early times then reaches a local minimum before leveling off at its steady state value. No attempt was made to correlate the transient  $\overline{Nu}$  results.

Patterson and Imberger (1980) used scale analysis to describe the transient behavior for small aspect ratio cavities ( $A \leq 1$ ). Heat transfer regimes were classified as conductive, convective, or transitional depending the magnitude of  $Ra$  relative to unity and a critical

Rayleigh number. The critical Rayleigh number,  $Ra_c$ , is determined completely from order of magnitude or scale analysis of the governing equations ( $Ra_c = \max(Pr^2, A^{-12})$ ). When  $Ra < 1$ , the transient response is dominated by pure conduction. When  $Ra > Ra_c$ , the dominant mode of heat transfer is by convection (the early transient is always conductive) and when  $1 < Ra < Ra_c$ , the heat transfer is termed transitional in which both conduction and convection are important features. The case of  $A \leq 1$  and  $Pr > 1$  was considered and six different transient responses were identified depending on values of  $Ra$ ,  $Pr$ , and  $A$ . An oscillatory response of the flow field was identified when  $Ra > Pr^4 A^{-4}$ . In other words, velocities and temperatures in the flow field were found to oscillate as the solution proceeded to steady state. The authors attributed the oscillatory behavior to fluid "piling up" on the horizontal walls while waiting to be entrained by the vertical boundary layer flow on the opposite vertical walls. Oscillations in  $\overline{Nu}$  were demonstrated numerically when  $Ra > Pr^4 A^{-4}$ .

In an effort to determine if the oscillations predicted by Patterson and Imberger actually exist, Yewell, et al. (1982) performed experiments for low aspect ratio ( $A = 0.0625, 0.112$ ) enclosures at high Rayleigh numbers ( $10^9 \leq Ra \leq 10^{10}$ ). Two experiments with the parameter values exceeding the criterion established by Patterson and Imberger ( $Ra > Pr^4 A^{-4}$ ) were performed. In each case, the expected fluctuations in measured temperatures were not detected and Yewell, et al. were unable to confirm the wave motion predicted by Patterson and Imberger. Subsequent to the findings of Yewell, et al., Patterson (1984) imposed new limits for the generation of wave motion as  $Ra_c > \max(Pr^4 A^{-4}, A^{-12})$ . The new limit placed the experiments of Yewell, et al. into the waveless regime (both

experiments were for  $Ra < A^{-12}$ ). Patterson argues that in the extreme case of low aspect ratio enclosures the horizontal layer of fluid flow loses significant energy by conduction to the core prior to reaching the opposite wall and the fluid "pile up" does not occur.

Ivey (1984) also performed experiments in an attempt to confirm the existence of the wave motion predicted by Patterson and Imberger. The parameter values were within the range of oscillation behavior ( $RaPr^{-4}A^4 = 8.6, 3.6 \times 10^5; A = 1$ ) as predicted by Patterson and Imberger. For the case  $RaPr^{-4}A^4 = 8.6$ , no evidence of oscillating behavior was observed based on temperature measurements. For the case  $RaPr^{-4}A^4 = 3.6 \times 10^5$ , transient temperatures were highly oscillatory but apparently stochastic which suggested that the fluctuations are not produced by a regular interval wave like fluid structure. Flow visualizations revealed the existence of small eddies near the outflow corners of the cavity vertical boundary layers causing the oscillating temperatures. The eddies (as well as the temperature fluctuations) were attenuated quickly as the distance from the outflow source increased i.e. as the fluid reached the entraining boundary layer on the opposite side of the cavity. Ivey attributes this behavior to inertial effects of the flow in the discharge corner regions of the vertical walls and a case of internal hydraulic jump as discussed by Turner (1973). It is clear that regimes in transient behavior for this simple geometry are very complex and further work is required in this area.

Another configuration of the square cavity problem is shown in Figure 1.2. In this case, one vertical isothermal wall is heated or cooled at a temperature  $T_w$  with respect to the initially quiescent interior fluid at a temperature  $T_o$  and the remaining three walls are adiabatic. An advantage to this configuration is the unambiguous initial and ending fluid state in the cavity.

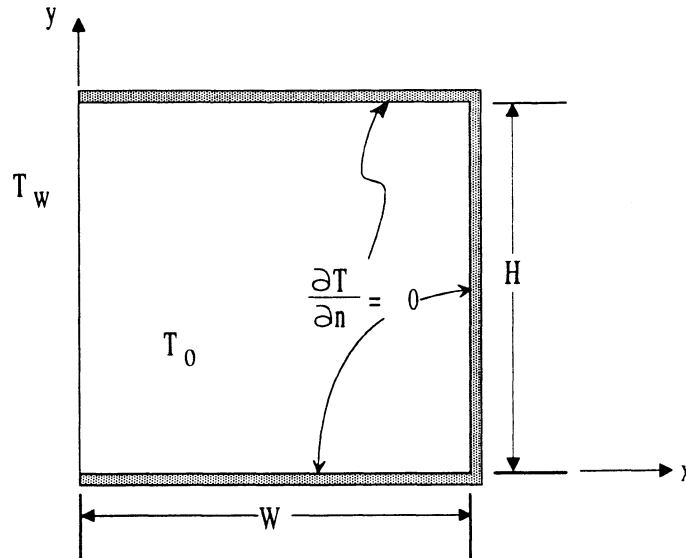


Figure 1.2: Adiabatic cavity with one sidewall heated/cooled.

Nicolette and Yang (1985) considered the configuration shown in Figure 1.2 with the sidewall cooled and the remaining walls adiabatic. They used a primitive variable formulation (based on SIMPLE) to solve the time dependent governing equations for  $10^5 \leq Ra/Pr \leq 10^7$ . Experiments were also performed. Since the initial condition of a step change in wall temperature could not be achieved experimentally, the wall temperatures measured during experiments were used as boundary conditions in the numerical computations. Calculated isotherms in the cavity compared well with interferogram measurements obtained from the experimental apparatus. Numerical computations showed the transient behavior of  $\overline{Nu}$  is dominated by pure conduction in early times before reaching a local minimum and leveling off for a short period of time then slowly decaying to zero. The authors mentioned the existence of "ripples" in the behavior of  $\overline{Nu}$  during the final decaying period. No measurements were made which would allow  $\overline{Nu}$  to be determined and no attempt was made to determine the source of the "ripple" behavior.

Although the boundary conditions make this problem quite unlike the differentially heated cavity, the "ripple" behavior in  $\overline{Nu}$  could be attributed to the wave phenomena reported by Patterson and Imberger (1980) and Ivey (1984).

Hall, et al. (1988) used scaling analysis similar to that used by Patterson and Imberger (1980) as well as numerical computations to solve the transient cavity problem shown in Figure 1.2. Scale analysis yields order-of-magnitude estimates of quantities such as  $\overline{Nu}$ , effectiveness (defined as the internal energy change fraction), time duration of the conduction dominated transient, etc. From the scaling analysis, two distinct periods were identified. As expected, the first is an early period dominated by pure conduction and the second period is predominantly convective. The predictions of  $\overline{Nu}$  and effectiveness from scale analysis compared well with the numerical computations. Numerical results are obtained by a SFV formulation with ADI method to solve the vorticity and energy equations. Successive over relaxation is used to solve the stream function equation. Interestingly, the computations of  $\overline{Nu}$  over time do not show the same features as that of Nicolette, et al. (1985). Figures 1.3 and 1.4 show the transient response of  $\overline{Nu}$  as given by the respective authors.

Although the scales in the above two figures are different, the solution of Hall, et al. does not appear to reach a local minimum followed by a brief plateau before decaying to zero. Also, neither paper discusses the potential existence (or lack thereof) of the wave motion predicted by Patterson and Imberger (1980). Thus, it is not clear that wave or oscillating motions will be generated in the absence of a second wall "driving" the fluid flow.

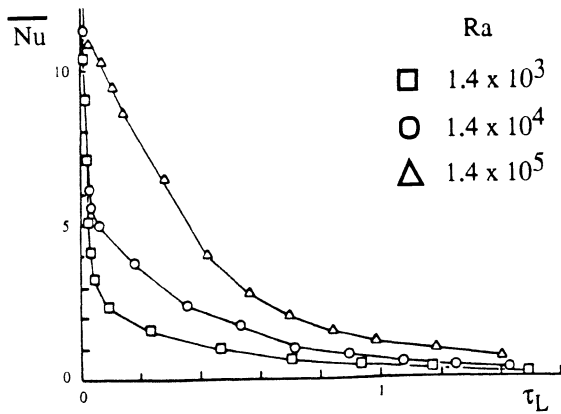


Figure 1.3: Transient response of  $\overline{Nu}$  from Nicolette, et al. (1985).

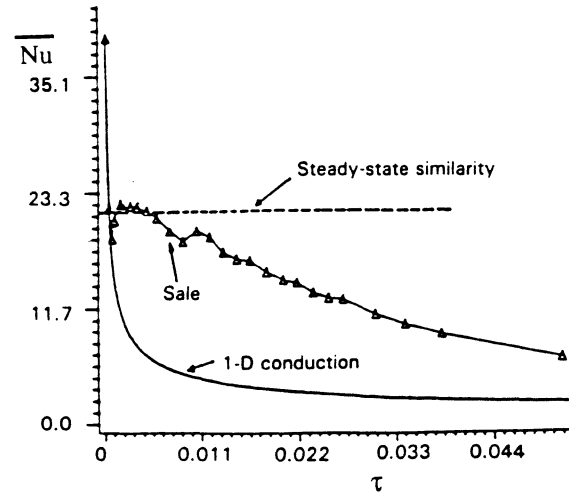


Figure 1.4: Transient response of  $\overline{Nu}$  from Hall, et al. (1988).

The previous studies focused on transient natural convection in an enclosure with bounding walls being responsible for "driving" the flow. A number of relevant applications contain sources within an enclosure which are responsible for driving the natural convection flow. For example, printed circuit boards with electronic devices generating heat are responsible for driving the flows in many electronic packaging configurations. Another example is found in solar thermal storage tanks with immersed coil heat exchangers. In this case, hot fluid circulating through a heat exchanger within the tank will drive the natural convection heat transfer process during charge and discharge. These applications dictate the need for analyzing natural convection in enclosures that contain sources. One of the simplest transient enclosure problems containing a source is an insulated rectangular cavity with a heated vertical isothermal flat plate on the interior as shown in Figure 1.5.

Khalilollahi and Sammakia (1986) considered the problem of a vertical flat plate (of height  $H/3$ ) centered in an adiabatic cavity. The overall aspect ratio ( $H/W$ ) of the cavity was 0.25 and the Rayleigh number was fixed at  $Ra = 3.35 \times 10^6$ . The authors noted the

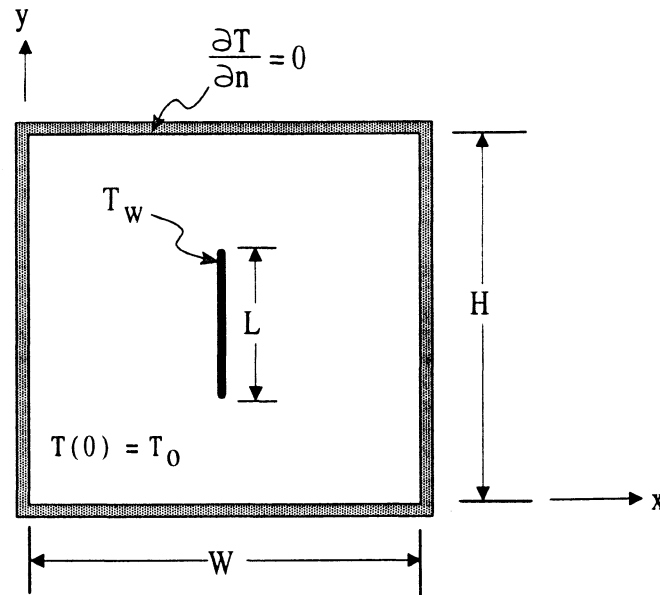


Figure 1.5: Adiabatic cavity with a heated vertical plate source.

existence of three temporal regimes. Initially, the behavior is dominated by pure conduction followed by a brief convective regime which closely agrees with the behavior of a flat plate in an infinite medium. At later times, the flow field decays as the bulk temperature in the cavity rises. The authors reported oscillations in the velocity and temperature fields similar to that predicted by Patterson and Imberger (1980) or Ivey (1984) but the study leaves several unanswered questions. When does the enclosure have a significant impact on the heat transfer from the plate or source inside the enclosure compared to a flat plate in an infinite medium? How is the behavior of the heat transfer altered with vertical and lateral positioning of the source from the centerline of the enclosure (dependence on source location)? How do the heat transfer results change with Rayleigh numbers? Can the transient heat transfer results be correlated?

Some of these questions were addressed by Charmchi and Sparrow (1982) considering the geometry of concentric vertical isothermal cylinders at steady state as shown in Figure 1.6. The cylinders have a unity aspect ratio (height/diameter) with the inner cylinder diameter ( $d_i$ ) size varying between 0.1 and 0.3 times the size of the outer enclosure diameter ( $d_o$ ). The vertical position of the inner cylinder,  $z_c$ , was varied from bottom to top along the centerline of the outer cylinder. The Rayleigh number (based on the inner cylinder diameter) was varied from 0 to  $10^5$ . The governing differential equations are solved using a primitive variable formulation (SIMPLE). Contrary to what one would expect, the authors found that the vertical position of the smaller inner cylinder ( $d_i = 0.1 d_o$ ) had little influence on  $\overline{Nu}$ . Similar independence was found for the larger diameter cylinder ( $d_i = 0.3 d_o$ ). Also, the  $\overline{Nu}$  results were compared with a correlation given by Kuehn (1976) for a vertical cylinder in a large domain. In the worst case ( $d_i = 0.3 d_o$ ), the calculated  $\overline{Nu}$  by Charmchi and Sparrow was 18% less than that given by Kuehn. Thus, it appears that the inner to outer cylinder diameter ratio should be greater than 0.3 in order for the bounding outer enclosure to have a significant effect.

In a companion study, Sparrow and Charmchi (1983) constructed an experimental apparatus to observe the effect of radial eccentricity of the inner cylinder. The results showed that the eccentricity of the inner cylinder had little influence on the average Nusselt number; consequently,  $\overline{Nu}$  was correlated as a function of  $Ra$  only and the inner cylinder height and eccentricity was disregarded. Experimental results for  $1600 \leq Ra \leq 10^5$  were compared with the numerical computations of the same geometry. The experimental data, in terms of an average Nusselt number, were higher than the predicted numerical results

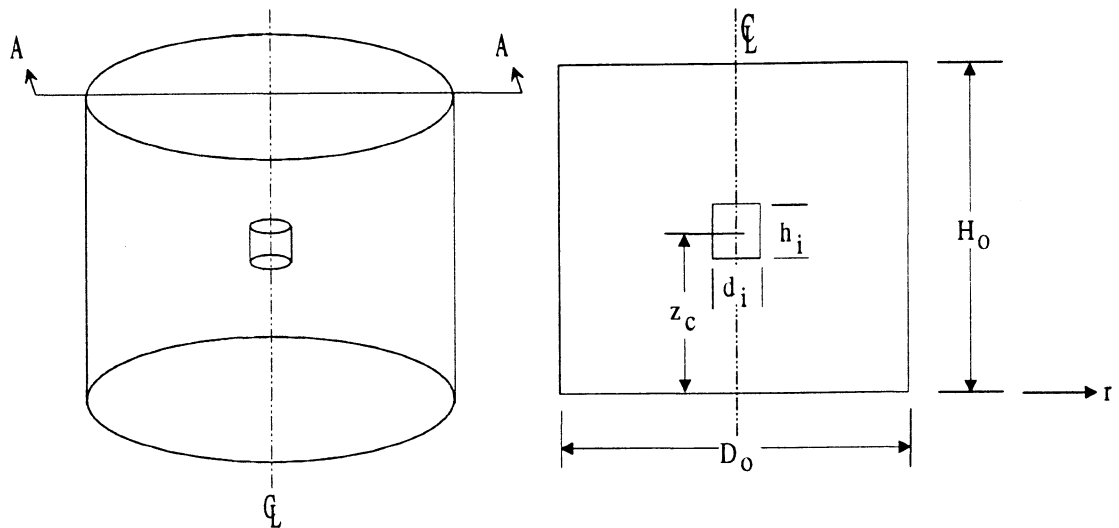


Figure 1.6: Isometric view and cross-section views of the concentric vertical isothermal cylinders used by Charmchi and Sparrow (1982);  $D_o = H_o$ ,  $d_i = h_i$ .

for low Rayleigh number cases ( $Ra \sim 1600$ ). At high Rayleigh numbers, the experimentally determined average Nusselt numbers were lower than the numerically predicted Nusselt numbers. The maximum reported deviations were within  $\pm 3\%$ .

These studies still leave unanswered questions. Will the transient heat transfer be insensitive to the source location? The size of the inner cylinder was not increased to the point where a significant effect of the enclosure was influencing the heat transfer results. How large must the inner cylinder (or other source) be in order for the enclosure to have a significant influence on heat transfer? Do the results of vertical plate and vertical cylinders extend to other geometric configurations?

## 1.2 Research Objectives

In an effort to complete and extend some of the previously reported results of natural convection from sources in enclosures, two configurations will be considered in this

investigation. The first configuration is an insulated rectangular enclosure with an isothermal vertical flat plate source as given in Figure 1.5. The configuration is similar to that of Khalilollahi and Sammakia (1986) and has applications in cooling of electronic equipment. The purpose of this portion of the investigation is to address the unanswered questions from the previous study of Khalilollahi and Sammakia such as: determining when the enclosure has a significant impact on the heat transfer from the plate or source inside the enclosure compared to a flat plate in an infinite medium; observing how the heat transfer is altered with vertical positioning of the source from the centerline of the enclosure (dependence on source location); influence of Rayleigh number on the transient heat transfer; and attempting to correlate the transient heat transfer results. Results from the rectangular enclosure geometry also provide a basis for comparison with the second configuration.

The second configuration is an insulated cylindrical enclosure with a single loop coiled tube source as shown in Figure 1.7. This configuration has applications in thermal storage tanks that contain immersed heat exchangers. To the best of the author's knowledge, this configuration has not been previously studied numerically.

The specific goals of this research include:

- 1.) Gain insight into the fundamental physics of transient fluid flow and heat transfer from sources within an enclosure.
- 2.) Identify when the bounding enclosure walls have an effect on the heat transfer from the source. Also, determine the influence of source position on the heat transfer and fluid flow field.
- 3.) Identify relevant parameters to correlate the transient heat transfer results (this may include the use of scaling analysis).
- 4.) Validate numerical results by physical experiments.

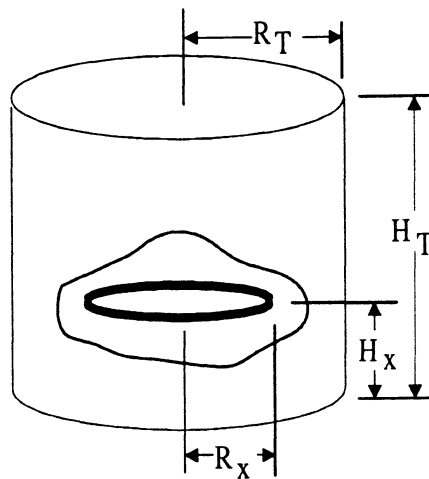


Figure 1.7: Single coil tube in cylindrical enclosure configuration.

For the rectangular enclosure with the heated vertical flat plate as given in Figure 1.5, the following parameters will be varied, Rayleigh number (based on plate length), relative vertical plate position ( $\eta = y_p/H$ ), and relative plate size ( $\phi = L/H$ ). Varying the lateral plate position will not be considered because the symmetry assumption would clearly be invalid thereby greatly increasing the computational effort.

## References

- 
- Batchelor, G. K., "Heat Transfer by Free Convection Across A Closed Cavity Between Vertical Boundaries At Different Temperatures", *Quarterly of Applied Mathematics*, Vol. XII, No. 3, pp. 209-233, October (1954).
- Betts, P. L., Haroutunian, V., "A Stream Function Finite Element Solution for Two-Dimensional Natural Convection with Accurate Representation of Nusselt Number Variations Near a Corner", *International Journal for Numerical Methods in Fluids*, **3**, pp. 605-622, (1983).
- Charmchi, M and Sparrow, E. M., "Analysis of Natural Convection in the Space between Concentric Vertical Cylinders of Different Height and Diameter", *Numerical Heat Transfer*, **5**, pp. 119-144, (1982).
- Chen, K. S., Ho, J. R., Humphrey, J. A. C., "Steady, Two-Dimensional, Natural Convection in Rectangular Enclosures with Differentially Heated Walls", *ASME Journal of Heat Transfer*, **109**, pp. 400-406, (1987).
- de Vahl Davis, G., Jones, I. P., "Natural Convection in a Square Cavity: A Comparison Exercise", *International Journal for Numerical Methods in Fluids*, **3**, pp. 227-248 (1983a).
- de Vahl Davis, G., "Natural Convection of Air in a Square Cavity: A Benchmark Numerical Solution", *International Journal for Numerical Methods in Fluids*, **3**, pp. 249-264 (1983b).
- Duxbury, D., "An Interferometric Study of Natural Convection in Enclosed Plane Air Layers", M.Sc. Thesis, University of Salford, England, (1972).
- Eckert, E. R. G., Carlson, W. O., "Natural Convection in an Air Layer Enclosed Between Two Vertical Plates With Different Temperatures", *International Journal of Heat and Mass Transfer*, **2**, pp. 106-120, (1961).
- Hall, J. D., Bejan, A., Chaddock, J. B., "Transient Natural Convection In a Rectangular Enclosure With One Heated Side Wall", *International Journal of Heat and Fluid Flow*, **9**(4), pp. 396-404, (1988).
- Han, J. T., "A Computational Method to Solve Nonlinear Elliptic Equations for Natural Convection in Enclosures", *Numerical Heat Transfer*, **2**, pp. 165-175, (1979).

Ivey, G. N., "Experiments on Transient Natural Convection in a Cavity", *Journal of Fluid Mechanics*, **144**, pp. 389-401, (1984).

Jones, I. P., "A Numerical Study of Natural Convection in an Air-Filled Cavity: Comparison With Experiment", *Numerical Heat Transfer*, **2**, pp. 193-213, (1979a).

Jones, I. P., "A Comparison Problem for Numerical Methods in Fluid Dynamics: The Double-Glazing Problem", *Numerical Methods in Thermal Problems* (edited by R. W. Lewis and K. Morgan), pp. 338-348, Pineridge Press, Swansen, U.K., (1979b).

Khalilollahi, A., Sammakia, B., "Unsteady Natural Convection Generated by a Heated Surface Within an Enclosure", *Numerical Heat Transfer*, **9**, pp. 715-730, (1986).

Kuehn, T. H., Natural Convection Heat Transfer from a Horizontal Cylinder to a Surrounding Cylindrical Enclosure, Ph.D. thesis, Dept. of Mechanical Engineering, University of Minnesota, Minneapolis, MN, (1976).

Lin, D. S., Nansteel, M. W., "Natural Convection Heat Transfer in a Square Enclosure Containing Water Near its Density Maximum", *International Journal of Heat and Mass Transfer*, **30**, pp. 2319-2329, (1987).

Markatos, N. C., Pericleous, K. A., "Laminar and Turbulent Natural Convection in an Enclosed Cavity", *International Journal of Heat and Mass Transfer*, **27**, pp. 755-772, (1984).

Marshall, R. S., Heinrich, J. C., Zienkiewicz, O. C., "Natural Convection In a Square Enclosure By A Finite Element, Penalty Function Method Using Primitive Fluid Variables", *Numerical Heat Transfer*, **1**, pp. 315-330, (1978).

Newell, M. E., Schmidt, F. W., "Heat Transfer by Laminar Natural Convection Within Rectangular Enclosures", *ASME Journal of Heat Transfer*, pp. 159-168, (1970).

Nicolette, V. F., Yang, K. T., "Transient Cooling by Natural Convection in a Two Dimensional Square Enclosure", *International Journal of Heat and Mass Transfer*, **28**(9), pp. 1721-1732, (1985).

Ozoe, H., Mouri, A., Ohmuro, M., Churchill, S. W., Lior, N., "Numerical Calculations of Laminar and Turbulent Natural Convection in Water in Rectangular Channels Heat and Cooled Isothermally on the Opposing Vertical Walls", *International Journal of Heat and Mass Transfer*, **28**, pp. 125-138, (1985).

Patankar, S. V., Spalding, D. B., "A Calculation Procedure for Heat, Mass, and Momentum Transfer in Three-Dimensional Parabolic Flows", *International Journal of Heat and Mass Transfer*, **15**, pp. 1787, (1972).

Patterson, J., Imberger, J., "Unsteady Natural Convection In a Rectangular Cavity", *Journal of Fluid Mechanics*, **100**, pp. 65-86, (1980).

Patterson, J. C., "On The Existence of an Oscillatory Approach to Steady Natural Convection in Cavities", **106**, *ASME Journal of Heat Transfer*, pp. 104-108, (1984).

Potts, G., "Heat Transfer by Laminar Free Convection in Enclosed Plane Gas Layers", *Quarterly of Mechanics and Applied Mathematics*, **11**, pp. 257-273, (1958).

Sparrow, E. M., Charmchi, M., "Natural Convection Experiments in an Enclosure Between Eccentric or Concentric Vertical Cylinders of Different Height and Diameter", *International Journal of Heat and Mass Transfer*, **26**(1), pp. 133-143, (1983).

Turner, J. S., Buoyancy Effects In Fluids Cambridge Press, pp. 179, (1973).

Wilkes, J. O., Churchill, S. W., "The Finite-Difference Computation of Natural Convection in a Rectangular Enclosure, *American Institute of Chemical Engineers Journal*, **12**(1), pp. 161-166, (1966).

Yewell, R., Poulikakos, D., Bejan, A., "Transient Natural Convection Experiments in Shallow Enclosures", *ASME Journal of Heat Transfer*, **104**, pp. 533-538, (1982).

## 2 Vertical Flat Plate In A Rectangular Enclosure

The first geometric configuration studied is the vertical flat plate in a rectangular enclosure. There are several benefits to beginning with this geometry. First, it is one of the simplest source driven transient natural convection enclosure problems that can be devised. Second, the body of literature is rich with numerical and experimental results for a flat plate in an **infinite** medium to allow comparisons to be made between the finite and infinite medium. Finally, because this type of configuration arises in various applications such as cooling of electronic equipment, it is of practical importance.

### 2.1 Governing Equations for Rectangular Enclosure

The rectangular enclosure contains a vertical flat plate which is infinitely thin and located in the center of the cavity i.e. at  $x=W/2$ . Symmetry can be used to reduce the computational domain by a factor of two. The computational domain for the rectangular enclosure is shown in Figure 2.1.

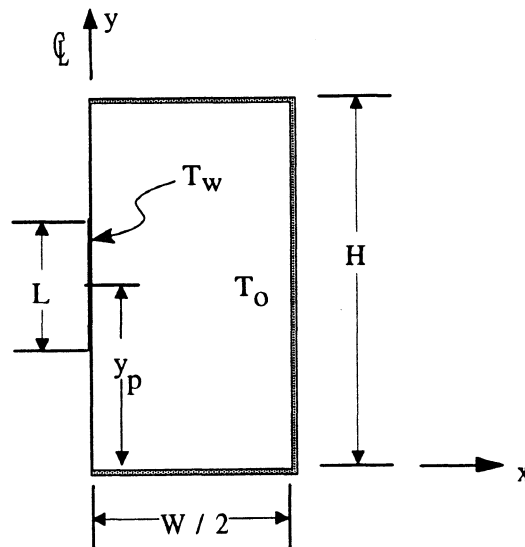


Figure 2.1: Computational domain for the rectangular enclosure with a flat plate.

The governing equations that describe the heat transfer and fluid flow for this configuration include the conservation of mass (continuity), momentum (Navier-Stokes), and energy. The equations are derived based on the following assumptions: incompressible ( $\rho \neq f(P)$ ), Newtonian fluid, low speed flow (viscous dissipation neglected), laminar, isotropic thermal conductivity, Boussinesq approximation, and fluid obeys Joule's law (enthalpy  $i = f(T)$ ). In natural convection, the only driving force for fluid flow is due to density differences caused by temperature differences in the flow field. The driving force appears as a body force term in the  $y$ -momentum equation. An approximation to relate the body force term (buoyancy force) to temperature is called the Boussinesq approximation. The use of this approximation dates back to Oberbeck (1879); however, the approximation is named after Boussinesq (1903). Gray and Giorgini (1976) develop and investigate the valid regions of the approximation for both liquids and gases. The essence of the approximation consists of the following: density is assumed constant except in the momentum body force term, all other properties are assumed constant, and viscous dissipation is negligible.

It is convenient to non-dimensionalize the governing system of equations with the variables given in Table 2.1.

$x^* = x/L$	$y^* = y/L$
$u^* = u/U$	$v^* = v/U$
$T^* = (T - T_o)/(T_w - T_o)$	$P^* = P/\rho U^2$
$t^* = tU/L$	$U = \sqrt{g\beta(T_w - T_o)L}$

Table 2.1: Rectangular geometry variable non-dimensionalization.

Based on the above assumptions, the dimensionless governing equations (dropping the \* superscript) and boundary conditions are:

Conservation of Mass:

$$\frac{\partial u}{\partial x} + \frac{\partial v}{\partial y} = 0 \quad (2.1)$$

x - Momentum:

$$\frac{\partial u}{\partial t} + u \frac{\partial u}{\partial x} + v \frac{\partial u}{\partial y} + \frac{\partial P}{\partial x} = \sqrt{\frac{Pr}{Ra}} \left[ \frac{\partial^2 u}{\partial x^2} + \frac{\partial^2 u}{\partial y^2} \right] \quad (2.2)$$

y - Momentum:

$$\frac{\partial v}{\partial t} + u \frac{\partial v}{\partial x} + v \frac{\partial v}{\partial y} + \frac{\partial P}{\partial y} = \sqrt{\frac{Pr}{Ra}} \left[ \frac{\partial^2 v}{\partial x^2} + \frac{\partial^2 v}{\partial y^2} \right] + T \quad (2.3)$$

Energy:

$$\frac{\partial T}{\partial t} + u \frac{\partial T}{\partial x} + v \frac{\partial T}{\partial y} = \frac{1}{\sqrt{RaPr}} \left[ \frac{\partial^2 T}{\partial x^2} + \frac{\partial^2 T}{\partial y^2} \right] \quad (2.4)$$

Boundary Conditions:

@ $x = 0$	$0 \leq y < (H-L)/2L$	$u = 0, \partial v / \partial x = 0$	$\partial T / \partial x = 0$
@ $x = 0$	$(H+L)/2L < y \leq H/L$	$u = 0, \partial v / \partial x = 0$	$\partial T / \partial x = 0$
@ $x = 0$	$(H-L)/2L \leq y \leq (H+L)/2L$	$u = v = 0$	$T = T_w = 1$
@ $x = W/2L$	$0 \leq y \leq H/L$	$u = v = 0$	$\partial T / \partial x = 0$
@ $y = 0$	$0 \leq x \leq W/2L$	$u = v = 0$	$\partial T / \partial y = 0$
@ $y = H/L$	$0 \leq x \leq W/2L$	$u = v = 0$	$\partial T / \partial y = 0$

Initial Conditions:

$$\text{for all } x \text{ and } y \quad u = v = 0 \quad T(0) = 0$$

A quantity of primary interest in this study is the average Nusselt number (average dimensionless heat flux)  $\overline{Nu}$  over the heated wall. The average Nusselt number is the integral of the local heat flux over the length of the vertical plate as given by

$$q = k \frac{\partial T}{\partial x} \Big|_w \quad (2.5)$$

$$q = h(T_w - T_o) \quad (2.6)$$

$$Nu_y = \frac{hy}{k} \quad (2.7)$$

where  $h$  is the heat transfer coefficient. From Equations 2.5-2.7, the local Nusselt number can be expressed as,

$$Nu_y = \frac{y}{T_w - T_o} \frac{\partial T}{\partial x} \Big|_w \quad (2.8)$$

Applying the dimensionless variables given in Table 2.1 (dropping the \* superscripts) and integrating over the length of the surface of interest (vertical plate) yields the average Nusselt number.

$$\overline{Nu} = \int_0^1 \frac{\partial T}{\partial x} \Big|_w dy \quad (2.9)$$

The average Nusselt number defined by Equation 2.9 is based on the instantaneous heat flux (given in Equation 2.5) determined from the initial temperature difference ( $T_w - T_o$ ). The average Nusselt number is commonly defined based on an instantaneous temperature difference ( $T_w - \overline{T}$ ); where the mean temperature  $\overline{T}$  is determined by volume (area for

two-dimensional domains) weighting the temperature in a neighborhood near the plate. The average Nusselt number based on mean temperature  $\overline{Nu}_m$  is given by the following expression.

$$\overline{Nu}_m = \frac{(T_w - T_o)}{(T_w - \overline{T})} \int_0^1 \frac{\partial T}{\partial x} \Big|_w dy \quad (2.10)$$

where  $\overline{T}$  is the mean or bulk temperature in the domain of interest  $\Omega$ .

$$\overline{T} = \frac{1}{\Omega} \int_{\Omega} T d\Omega \quad (2.11)$$

In the context of transient enclosure problems, the definition of average Nusselt number given by Equation 2.10 is less useful than the definition given by Equation 2.9. In both cases, the average Nusselt number is dependent on the heat flux (which is a function of time) at the wall surface but Equation 2.10 requires additional knowledge of the instantaneous bulk temperature. Such a definition creates an implicit relationship between the average Nusselt number and the entire temperature field. Because the definition of  $\overline{Nu}$  based on the initial temperature difference eliminates the additional uncertainty introduced by the bulk temperature, this definition will be applied throughout the current investigation.

## 2.2 Solution Technique

The governing differential equations represent the behavior of the dependent variables in the region of interest (which is a continuum) over time. An analytical solution to the strongly coupled system of differential equations provides values of the dependent variables at any location within the region considered at any point in time. Since an

analytical solution is not currently possible and approximate analytical solutions are of unknown accuracy, numerical methods are required to make the system tractable. A common approach is to use finite difference methods (FDM). Finite difference techniques are attractive because derivation of difference equations and analysis (error and stability) is relatively easy. One major disadvantage of the FDM is the difficulty in modelling domains with arbitrary shaped boundaries. Another method gaining popularity is the finite element method (FEM). The FEM is superior in its ability to model arbitrary shaped domains; however, analysis of FEM becomes rather complicated quickly. The flexibility of the FEM in modelling arbitrary shaped geometries is important when considering potential enclosure configurations that contain sources such as the immersed coil heat exchanger. Thus, the FEM will be employed in this investigation.

Once the numerical method is selected, the next step is to decide on a variable formulation. The literature search indicates a preference toward the stream function - vorticity (or alternate variable formulations) as compared to primitive variable (i.e.  $u$ - $v$ - $P$ ) formulations. The SFV formulation is derived by defining the stream function,  $\psi$ , as  $u = \partial\psi/\partial y$  and  $v = -\partial\psi/\partial x$ . When the definition of stream function is substituted into the continuity equation, mass conservation will be identically satisfied. Next the two momentum equations are cross differentiated and subtracted; thereby, eliminating pressure and producing a single equation which can be further simplified by applying the definition of vorticity,  $\xi = \left(\frac{\partial v}{\partial x} - \frac{\partial u}{\partial y}\right)$ . The resulting system yields a Poisson equation for stream function and two parabolic equations for vorticity and energy respectively. An obvious question at this point is: why use these auxiliary variables? The advantage of a SFV

formulation is the elimination of pressure and satisfying mass conservation. Determining the pressure field to satisfy mass conservation (the divergence of the velocity) poses one of the greatest difficulties with primitive variable formulations.

There are several disadvantages in using alternative variable formulations. First, the alternate variable formulations tend to obscure the physics of the problem at hand. Associated with this is the difficulty of determining the correct boundary conditions in the alternate variables. Third, the alternate variable approach is difficult to extend to three dimensional computational domains (probably the biggest disadvantage). Thus, it is advantageous to implement a primitive variable formulation.

As previously mentioned, a key advantage of the FEM is the ability to easily model arbitrary complex shaped domains. This flexibility makes the method extremely attractive in modelling enclosures with sources. Since the development of the FEM is rather abstract and lengthy, only the essential results will be presented. For details of the FEM, the reader is referred to one of several sources including: Zienkiewicz (1977), Becker, et al. (1981), Carey and Oden (1986), and Burnett (1988). For brevity, the derivation of the FEM will be illustrated using the dimensionless energy equation.

Consider the energy equation Equation 2.4 and general boundary conditions applied to a two-dimensional domain,  $\Omega$ , with boundary,  $\Gamma$ , as shown in Figure 2.2.

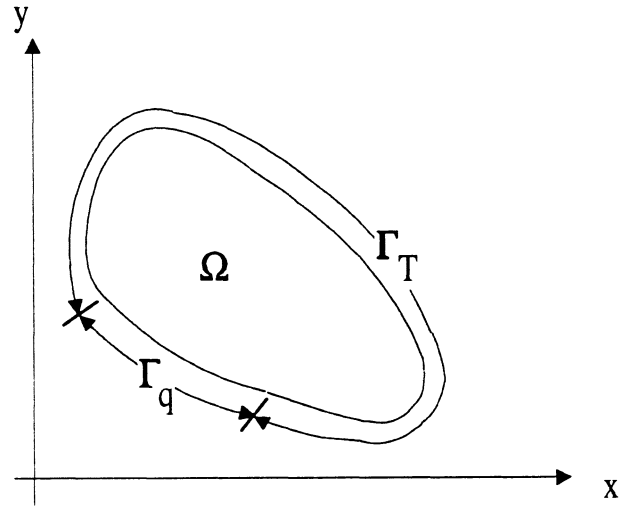


Figure 2.2: General computational domain.

Energy Equation:

$$\frac{\partial T}{\partial t} + u \frac{\partial T}{\partial x} + v \frac{\partial T}{\partial y} - \sigma \left[ \frac{\partial^2 T}{\partial x^2} + \frac{\partial^2 T}{\partial y^2} \right] = R(x, y, t) \quad (2.12)$$

Boundary Conditions:

$$T = T(x, y, t) \quad \text{on } \Gamma_T$$

$$\left( \frac{\partial T}{\partial x} n_x + \frac{\partial T}{\partial y} n_y \right) = q(x, y, t) \quad \text{on } \Gamma_q$$

where  $R(x, y, t)$  is a residual,  $\sigma = 1/\sqrt{RaPr}$ , and the first and second boundary conditions represent Dirichlet and Neumann boundary conditions respectively. In cases where the differential equation and geometry permit an exact solution by separation of variables, the dependent variable is assumed to satisfy a product solution such as  $T = \Theta(x, y)W(t)$  to separate the space and time variables. In a spirit similar to separation of variables, let the

independent variable,  $T$ , in Equation 2.12 be approximated by the following expansion

$$T(x, y, t) = \sum_{m=1}^M \theta_m(x, y) T_m(t)$$

or in vector notation

$$T(x, y, t) = \theta^T(x_i) T(t) \quad (2.13)$$

where  $\theta^T$  is the vector transpose of the spatial interpolation (often referred to as the trial or basis) function and  $T$  is a vector of  $M$  nodal point unknown temperatures. The result is an expression with the space and time variables "separated". The Galerkin weighted residual method forces the residual in Equation 2.12 to be zero over the domain in a weighted sense.

$$\int_{\Omega} w R \, d\Omega = 0 \quad (2.14)$$

where  $w$  is a weight function to be specified. Substituting the residual Equation 2.12 along with Equation 2.13 into the weighted integral Equation 2.14 results in the following:

$$\int_{\Omega} w \left[ \frac{\partial}{\partial t} (\theta^T T) + u \frac{\partial}{\partial x} (\theta^T T) + v \frac{\partial}{\partial y} (\theta^T T) - \sigma \frac{\partial^2}{\partial x^2} (\theta^T T) - \sigma \frac{\partial^2}{\partial y^2} (\theta^T T) \right] d\Omega = 0 \quad (2.15)$$

The weight function for the Galerkin method is the same as the basis function i.e.  $w = \theta$ .

Thus, the weighted integral in Equation 2.15 becomes

$$\int_{\Omega} \theta \theta^T \, d\Omega \frac{\partial T}{\partial t} + \int_{\Omega} \theta \left[ u \frac{\partial \theta^T}{\partial x} + v \frac{\partial \theta^T}{\partial y} \right] \, d\Omega T - \int_{\Omega} \sigma \theta \left[ \frac{\partial^2 \theta^T}{\partial x^2} + \frac{\partial^2 \theta^T}{\partial y^2} \right] \, d\Omega T = 0 \quad (2.16)$$

From the chain rule,

$$\theta \frac{\partial^2 \theta^T}{\partial x^2} = \frac{\partial}{\partial x} \left( \theta \frac{\partial \theta^T}{\partial x} \right) - \frac{\partial \theta}{\partial x} \frac{\partial \theta^T}{\partial x}$$

$$\theta \frac{\partial^2 \theta^T}{\partial y^2} = \frac{\partial}{\partial y} \left( \theta \frac{\partial \theta^T}{\partial y} \right) - \frac{\partial \theta}{\partial y} \frac{\partial \theta^T}{\partial y}$$

Substituting the above expressions into Equation 2.16 and applying the divergence theorem yields

$$\int_{\Omega} \theta \theta^T d\Omega \frac{\partial T}{\partial t} + \int_{\Omega} \theta \left[ u \frac{\partial \theta^T}{\partial x} + v \frac{\partial \theta^T}{\partial y} \right] d\Omega T + \int_{\Omega} \sigma \left[ \frac{\partial \theta}{\partial x} \frac{\partial \theta^T}{\partial x} + \frac{\partial \theta}{\partial y} \frac{\partial \theta^T}{\partial y} \right] d\Omega T = \oint_{\Gamma} \theta q d\Gamma \quad (2.17)$$

The last term in Equation 2.17 has been simplified from the Neumann boundary condition given above. Of course, the velocities in Equation 2.17 must also be discretized with another basis function. Equation 2.17 is known as the "weak form" of the energy equation. The nomenclature describes the relaxed or weakened conditions that the original differential equation must now satisfy. In other words, the continuous problem with an infinite number of degrees of freedom has been reduced to a discrete problem with a finite number of degrees of freedom which consists of a system of ordinary differential equations (for steady state problems, it would be just a system of nonlinear algebraic equations). For the current investigation the integrals in Equation 2.17 are carried out using Gaussian quadrature.

Upon applying the finite element approximations (Galerkin optimizing criteria, basis function selection, etc.), the system of partial differential equations (2.1-2.4) are transformed into a discrete set of ordinary differential equations as given by

$$\bar{M} \frac{dV}{dt} + \bar{K}(V)V = \bar{F} \quad (2.18)$$

where  $\overline{M}$  is a combined mass and capacitance matrix,  $\overline{K}$  is a combined momentum and thermal diffusion matrix,  $V$  is a vector of unknown nodal velocities and temperatures, and  $\overline{F}$  is the vector of forcing functions. Equation 2.18 represents a system of initial value problems for each of the nodal unknowns.

A second order implicit trapezoid rule multi-step scheme is used to integrate this system of ordinary differential equations. The first step (a predictor) is based on the Adams-Bashforth method with variable time increment as given by

$$V_{k+1}^p = V_k + \frac{\delta t_k}{2} \left\{ \left( 2 + \frac{\delta t_k}{\delta t_{k-1}} \right) \dot{V}_k - \frac{\delta t_k}{\delta t_{k-1}} \dot{V}_{k-1} \right\} \quad (2.19)$$

where  $V_{k+1}^p$  is the predicted vector of unknowns at time  $k+1$ ,  $\dot{V}_k$  is the time rate change of the unknowns at time  $k$ , and  $\delta t_k$  is the time increment at step  $k$ . The second step (a corrector) is the trapezoid rule with a variable time increment. When applied to Equation 2.18, the trapezoid rule yields

$$\overline{M} \frac{V_{k+1}^c - V_k}{\delta t_k} + \frac{1}{2} \{ \overline{K}(V_{k+1}^c) V_{k+1}^c + \overline{K}(V_k) V_k \} = \frac{1}{2} \{ \overline{F}_{k+1} + \overline{F}_k \} \quad (2.20)$$

The acceleration vectors  $\dot{V}$  in Equation 2.19 are computed recursively from the definition of the trapezoid rule by

$$\dot{V}_{k+1} = \frac{2}{\delta t_k} \{ V_{k+1} - V_k \} - \dot{V}_k \quad (2.21)$$

where  $\dot{V}_k$  is found from the previous use of Equation 2.21.

The above two step time integration scheme is able to accommodate a variable step size time increment. If a fixed time increment is specified, further simplifications are possible. Although a fixed time increment would allow the use of Richardson extrapolation

at each time step, the exorbitant computational resources required to carry out the time integration for the system of equations considered here precludes this approach. The adaptive scheme allows the time step to increase or decrease depending on the magnitude of the local time truncation error. The local time truncation error for the Adams-Bashforth method is

$$V_{k+1}^p - V(t_{k+1}) = -\frac{1}{12} \left( 2 + 3 \frac{\delta t_{k-1}}{\delta t_k} \right) \delta t_k^3 \ddot{V}_{k+1} + O(\delta t_k^4) \quad (2.22)$$

Similarly, the local time truncation error for the trapezoid rule is given by

$$E_{k+1} = V_{k+1}^c - V(t_{k+1}) = \frac{1}{12} \delta t_k^3 \ddot{V}_{k+1} + O(\delta t_k^4) \quad (2.23)$$

Combining Equations 2.22 and 2.23 yields

$$E_{k+1} = \frac{V_{k+1}^c - V_{k+1}^p}{3 \left( 1 + \frac{\delta t_{k-1}}{\delta t_k} \right)} + O(\delta t_k^4) \quad (2.24)$$

The result in Equation 2.24 can be used to estimate the size of the next time step by requiring the relative norm of the error for the next step to be less than a specified tolerance ( $\|E_{k+2}\| \leq \gamma$ ). From Equation 2.24, the following relationship for time truncation error results.

$$\frac{E_{k+2}}{E_{k+1}} = \left( \frac{\delta t_{k+1}}{\delta t_k} \right)^3 \frac{\ddot{V}_{k+2}}{\ddot{V}_{k+1}} \quad (2.25)$$

By taking norms and using the fact  $\ddot{V}_{k+2} = \ddot{V}_{k+1} + O(\delta t)$  as well as  $\|E_{k+2}\| \leq \gamma$ , Equation 2.25 results in an expression to determine the relative size of the next time increment.

$$\frac{\delta t_{k+1}}{\delta t_k} = \left( \frac{\gamma}{\|E_{k+1}\|} \right)^{1/3} \quad (2.26)$$

where higher order terms have been omitted. The norm  $\|E_{k+1}^j\|$  ( $j = u, v, T$ ) is defined based on the truncation error as given by Equation 2.24.

$$E_{k+1}^j = \frac{j_{k+1}^c - j_{k+1}^p}{3\left(1 + \frac{\delta t_{k-1}}{\delta t_k}\right)} + O(\delta t_k^4) \quad (2.27)$$

Since the order of magnitude for each variable may differ considerably, the error is approximated by defining a relative norm.

$$\|E_{k+1}\| = \left\{ \frac{1}{N_u + N_v + N_T} \left[ \sum_{i=1}^{N_u} \left( \frac{E_{k+1}^{u_i}}{|u_{k+1}^i|} \right)^2 + \sum_{i=1}^{N_v} \left( \frac{E_{k+1}^{v_i}}{|v_{k+1}^i|} \right)^2 + \sum_{i=1}^T \left( \frac{E_{k+1}^{T_i}}{|T_{k+1}^i|} \right)^2 \right] \right\}^{1/2} \quad (2.28)$$

where  $N_u, N_v, N_T$  are the respective number of free  $u$ -velocity,  $v$ -velocity, and temperature components.

By allowing a variable step size, time integration can be accomplished very efficiently. The time integration scheme results in a system of nonlinear algebraic equations to be solved at each time step. The system of nonlinear equations is solved by a quasi-Newton method.

Thus far, no mention has been made of "elements". In practice, the computational domain is divided into a number of simply shaped elements i.e. triangles, quadrilaterals, bricks, wedges, etc. These elements are defined by the basis functions as given in Equation 2.13. The network of individual elements are connected yielding a larger system of equations and the solution of the resulting system of equations provide functions which approximate values of the dependent variables over each element. The elements selected for this work are nine node quadrilaterals with a linear discontinuous pressure approximation (details of the pressure approximations will be given following discussion of element selection). The basis or trial functions are identical for both velocity and

temperature. To simplify numerical quadrature, the isoparametric approach is used. In this case, the integrations are performed on a "master" element defined over  $-1 \leq r, s \leq 1$  and the results are then mapped back to the computational domain as shown in Figure 2.3.

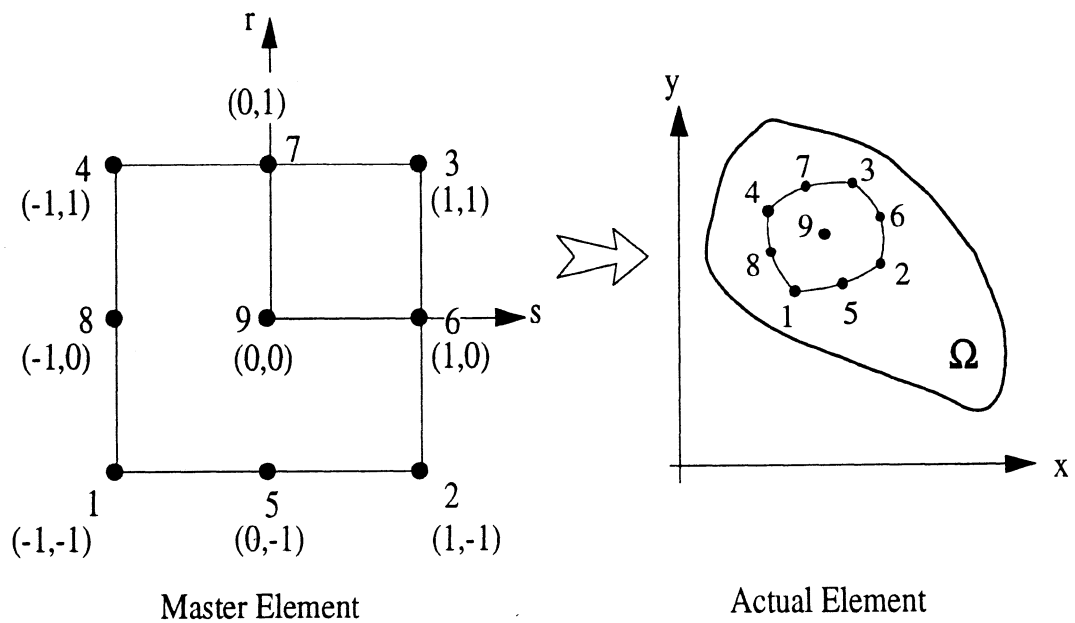


Figure 2.3: Master element and actual element in computational domain.

The basis or trial functions for the nine node quadrilateral are

$$\theta = \begin{Bmatrix} \frac{1}{4}rs(1-r)(1-s) \\ -\frac{1}{4}rs(1+r)(1-s) \\ \frac{1}{4}rs(1+r)(1+s) \\ -\frac{1}{4}rs(1-r)(1+s) \\ -\frac{1}{2}s(1-s)(1-r^2) \\ \frac{1}{2}r(1+r)(1-s^2) \\ \frac{1}{2}s(1+s)(1-r^2) \\ -\frac{1}{2}r(1-r)(1-s^2) \\ (1-r^2)(1-s^2) \end{Bmatrix} \quad (2.29)$$

The basis functions in Equation 2.29 provide a quadratic approximation for both velocity and temperature. They also have the property that allow the functions to be unity at the current node and zero at all other nodes. For example, the first function in Equation 2.29 is unity at node 1 and zero at all other nodes. In this sense, the functions are considered interpolatory. The map between the master element and the physical element is given by

$$x = \theta^T x; \quad y = \theta^T y \quad (2.30)$$

where  $\theta^T(r, s)$  is the vector transpose of basis functions as given in Equation 2.29.

As mentioned previously, pressure and its relation to satisfying the divergence of velocity presents unique difficulties in solving the Navier-Stokes equations. The penalty function approach is an attempt to alleviate problems caused by the presence of the pressure terms. The penalty method relaxes the strict continuity requirement by letting

$$\frac{\partial u}{\partial x} + \frac{\partial v}{\partial y} = -\epsilon P \quad (2.31)$$

where  $\epsilon$  is a penalty parameter. Typically, the value of the penalty parameter ranges from  $10^{-5}$  to  $10^{-9}$ . A value of  $\epsilon = 10^{-8}$  used for the penalty parameter in this investigation. Solving Equation 2.31 for pressure and substituting the result into the Navier-Stokes equations eliminates pressure. The pressure can be obtained subsequently by post-processing  $P = -1/\epsilon[\partial u/\partial x + \partial v/\partial y]$ .

The development of a finite element code was considered for this project; however, after considering all of the implementation details involved to achieve the required flexibility and efficiency, the development was abandoned. A search for commercial finite element codes led to FIDAP. FIDAP is a general purpose finite element computer program that has the ability to model a variety of incompressible fluid flow problems. FIDAP can simulate steady and transient flows with heat and/or mass transport in two-dimensional, axis symmetric, and three-dimensional geometries. It offers several choices of elements, system solution techniques, and time integration schemes such as those previously discussed.

### 2.3 Results

This section presents the results of computations performed on the rectangular cavity with a heated vertical flat plate shown in Figure 2.1. The relative plate size,  $\phi$ , and Rayleigh number are varied to observe the effects of heat transfer from the plate. In general, the heat transfer results are presented in terms of the average Nusselt number,  $\overline{Nu}$ , as calculated from Equation 2.9.

A typical mesh used to compute the solution for this configuration is shown below in Figure 2.4.

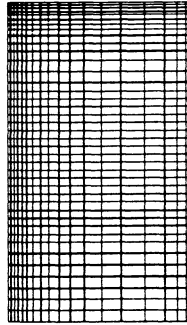


Figure 2.4: Typical mesh for square cavity with a heated vertical flat plate.

To arrive at the above mesh, considerable effort has been expended to assure that a solution independent of the mesh size is achieved by applying spatial and temporal refinement. Several indicators to track the solution convergence during mesh refinement were used including; temporal behavior of the average Nusselt number and the peak values along with the spatial location of each velocity component and stream function over all time. The mesh was refined spatially and temporally until there was little or no change in the above quantities (a technique is used in the development of a proposed transient benchmark problem by Reindl, et al. 1991).

One of the initial objectives was to determine the conditions under which the bounding walls have a significant impact on the heat transfer from the enclosure sources. To accomplish this objective, several relative plate sizes ( $\phi = L/H$ ) were investigated while observing the transient response of the average Nusselt number.

For a range of relative plate sizes from  $0.2 \leq \phi \leq 1$  and  $Ra = 10^6$ , the transient response of  $\overline{Nu}$  is shown in Figure 2.5. In each case, the transient  $\overline{Nu}$  is characterized by three regimes. Initially, the flow field is isothermal and quiescent as the plate undergoes the step change in temperature. The mode of heat transfer is by pure conduction since no fluid

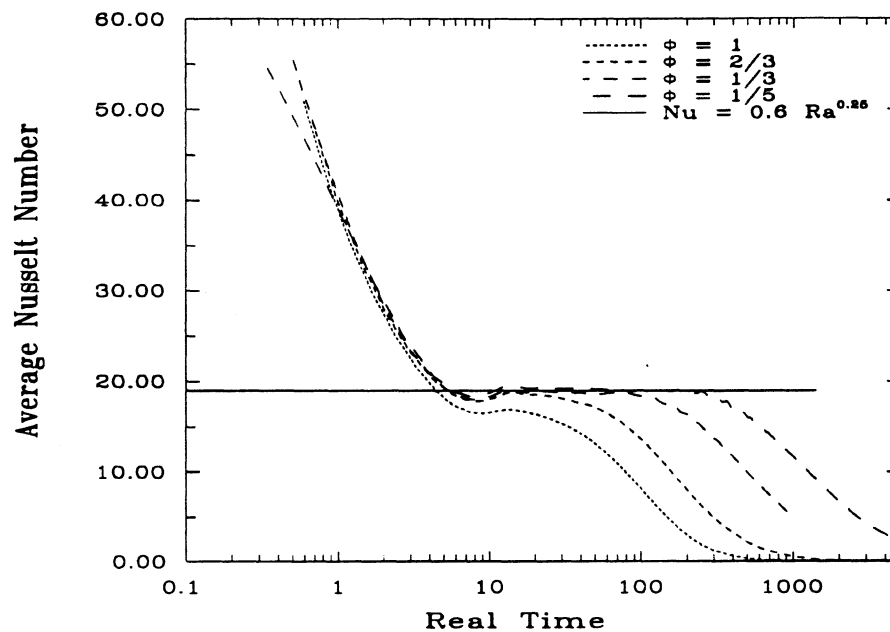


Figure 2.5: Transient  $\overline{Nu}$  for a range of relative plate sizes at  $Ra = 10^6$  and  $\eta = 0.5$ .

motion exists initially. The conduction heat transfer from the plate starts to establish a thermal boundary layer which grows with time. The average Nusselt number reaches a local minimum and subsequently begins to increase before reaching a value that is maintained during a quasi-steady period. The local minimum in  $\overline{Nu}$  corresponds to a maximum in the thermal boundary layer thickness which quickly decreases as significant fluid motion begins. As fluid motion develops, the  $\overline{Nu}$  increases to its quasi-steady value. During this quasi-steady period, thermal and momentum boundary layers are fully

established and the plate appears to behave as if it were immersed in an infinite medium. The solid line is an approximation to the heat transfer correlation for a vertical flat plate in an infinite medium (Churchill and Chu, 1975). Agreement with the correlation for a flat plate in an infinite medium confirms this behavior (for large enclosures). After some period of time, the heat input from the plate causes the bulk temperature in the cavity to rise significantly. The increase in bulk cavity temperature reduces the driving force (temperature difference across the plate) for heat transfer; consequently, the average Nusselt number begins to decay. The fluid velocities also begin to diminish.

Thus, there are three distinct regimes: conduction, quasi-steady, and a decay period. Given a sufficient period of time, the bounding enclosure will always have an effect on the transient heat transfer and fluid flow. The smaller the relative plate size, the longer the quasi-steady period can be maintained but there will be some instant in time in which the cavity temperature begins to rise and heat transfer decays. There is also a maximum relative plate size such that the quasi-steady period approaches the solution for a flat plate in an infinite medium. Based on observing the heat transfer behavior in Figure 2.5, the enclosure must be at least 1.5 times larger than the plate ( $\phi = 2/3$ ) in order for the heat transfer to approach the infinite medium case (based on a unit aspect ratio enclosure). Enclosures that are near this threshold size have very short quasi-steady periods.

The heat transfer results in Figure 2.5 represent a dimensionless heat flux or Nusselt number based on the initial temperature difference ( $T_w - T_o$ ). Figure 2.6 illustrates the difference between the average Nusselt numbers based on the initial temperature difference and the local or ( $T_w - \bar{T}$ ) temperature difference. The average Nusselt number based on mean temperature  $\overline{Nu}_m$  closely follows the average Nusselt number based on initial temperature  $\overline{Nu}$  during the conduction dominated regime. Over the quasi-steady regime,

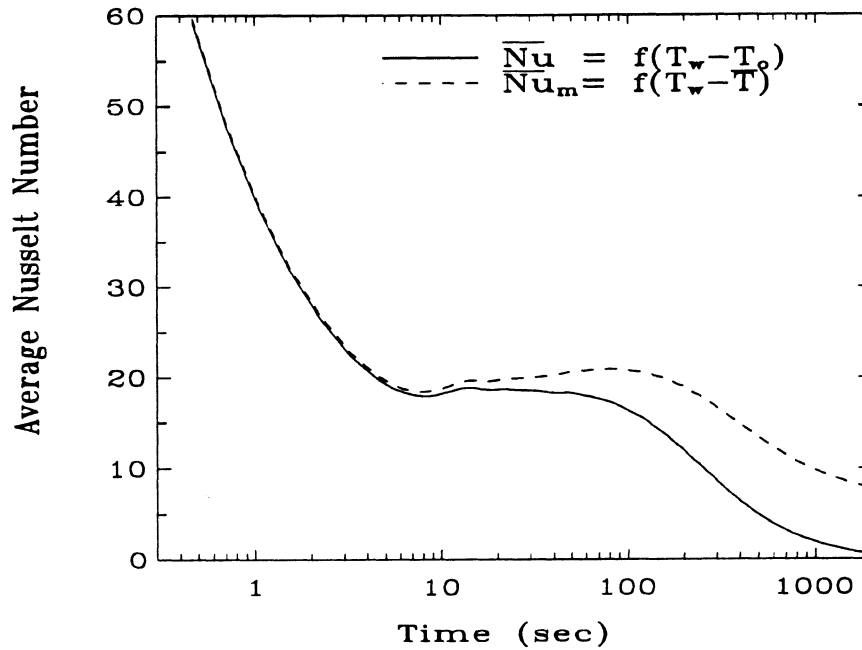


Figure 2.6: Transient  $\overline{Nu}$  and  $\overline{Nu}_m$  for  $Ra = 10^6$  and a relative plate size of  $\phi = 0.5$  and relative plate position  $\eta = 1/2$ .

$\overline{Nu}_m$  rises slightly because the mean temperature in the cavity is increasing while the heat input into the cavity remains relatively constant. The decay periods are quite different. The average Nusselt number  $\overline{Nu}_m$  does not go to zero because the heat flux and  $(T_w - \overline{T})$  temperature difference are both simultaneously approaching zero and their ratio  $\overline{Nu}_m \propto \overline{Nu} / (T_w - \overline{T})$  approaches a constant value.

Figure 2.7 shows a typical response of the average temperature in the cavity as a function of time. In comparing Figures 2.6 and 2.7, it is clear that the cavity bulk temperature only begins to rise significantly at the end of the quasi-steady period and continues to increase during the decay period.

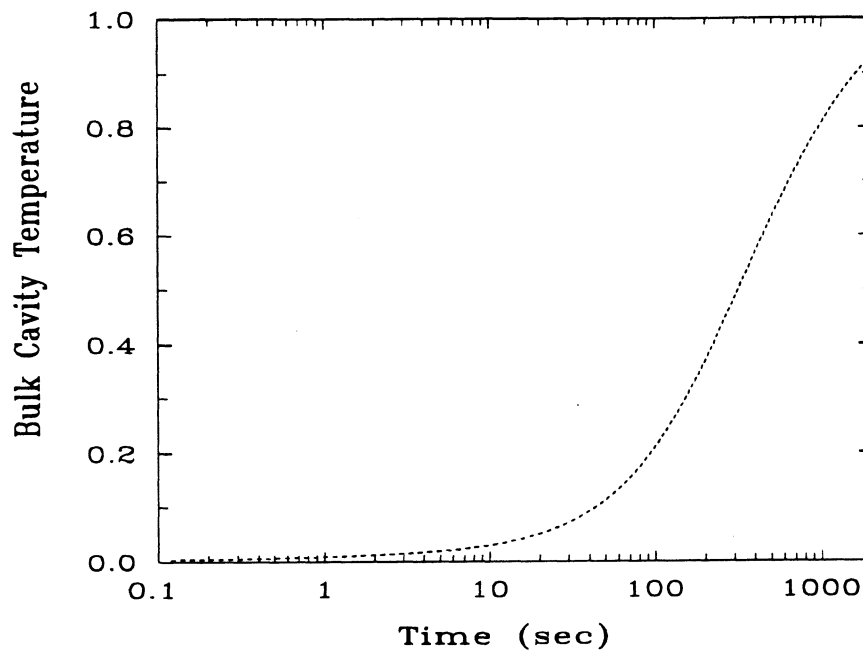


Figure 2.7: Mean cavity temperature for  $Ra = 10^6$  and a relative plate size of  $\phi = 0.5$  and relative plate position  $\eta = 1/2$ .

The limiting case of  $\phi = 1$  is nearly identical to the configuration studied by Nicolette and Yang (1985) and Hall, et al. (1988). Comparing Figure 2.5 with Figures 1.3 and 1.4, the qualitative behavior of  $\overline{Nu}$  in the current case shows trends similar to that of Nicolette

and Yang. The agreement with Hall, et al. is poor. Two factors cast the accuracy of the Hall, et al. solution into doubt. First, a relatively coarse (41x41) and uniform grid was used in the cavity. Second, no indication is given to judge the time accuracy of the solution.

The results in Figure 2.5 showed the effect of various relative plate sizes on the transient heat transfer from the plate with  $Ra = 10^6$ . Figure 2.8 illustrates the transient behavior of  $\overline{Nu}$  for four different values of  $Ra$  for a fixed relative plate size  $\phi = 1/2$  and plate position  $\eta = 1/2$  while letting the Rayleigh number vary from  $10^3$  to  $10^6$ .

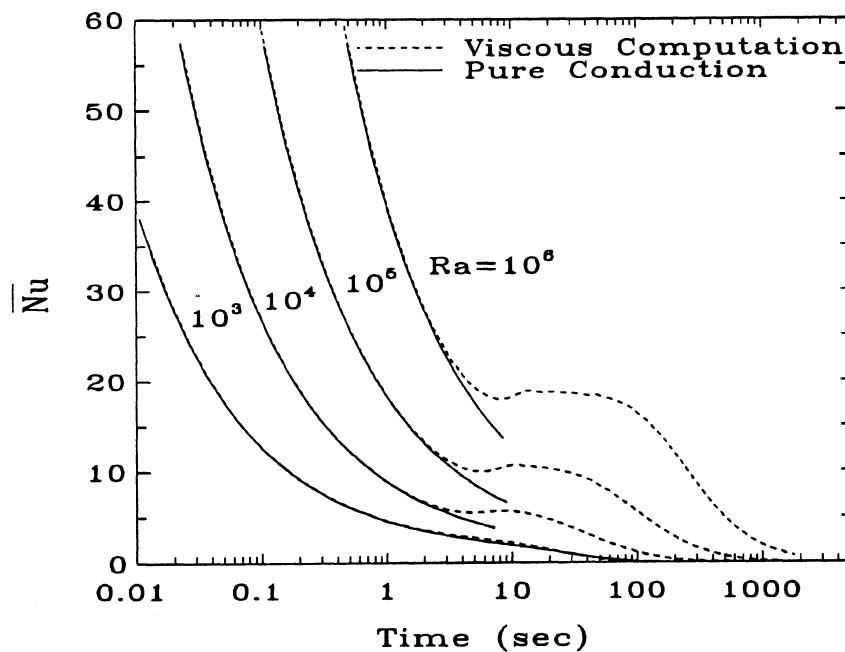


Figure 2.8: Transient  $\overline{Nu}$  (including pure conduction solutions) over a range of Rayleigh numbers for a relative plate size of  $\phi = 0.5$  and relative plate position  $\eta = 1/2$ .

The respective transient pure conduction solutions are also shown by the solid lines. Agreement with the viscous flow solution confirms the earlier conjecture that the initial heat transfer is by pure conduction. At low Rayleigh numbers ( $Ra \leq 10^3$ ), the heat transfer process closely follows the pure conduction case which indicates that the low Rayleigh number cases are very weakly convective throughout the entire process. The respective solutions at higher Rayleigh numbers show the three regimes previously discussed.

Figure 2.9 includes the same computed solutions as in Figure 2.8 as well as the steady state infinite medium solutions. Reasonable agreement of the quasi-steady regimes in each case is obtained with the limit for an infinite medium.

The temporal behavior of the heat transfer during the conduction and quasi-steady regimes is well characterized by the solid lines shown in Figures 2.6-2.7. Scale analysis can be used to predict the time duration of the conduction, quasi-steady, and complete transient periods. Scale analysis is a technique which considers the governing equations only in an order-of-magnitude sense. Patterson and Imberger (1980) used scale analysis extensively in their study of the differentially heated cavity. Interestingly, the scale estimates for the geometry considered here are similar to those which arise for the differentially heated cavity. Bejan (1984) maintains that scale analysis yields more information per intellectual effort than any other type of analysis. Bejan also offers a concise summary of rules applicable for scale analysis.

Scale analysis uses the governing equations of fluid flow and heat transfer to produce order-of-magnitude estimates of the quantities of interest. The technique typically requires the use of several of the governing equations in a series of intermediate results to arrive at the final quantity of interest. The following sequence of estimates attempts to predict the duration of the conduction dominated regime.

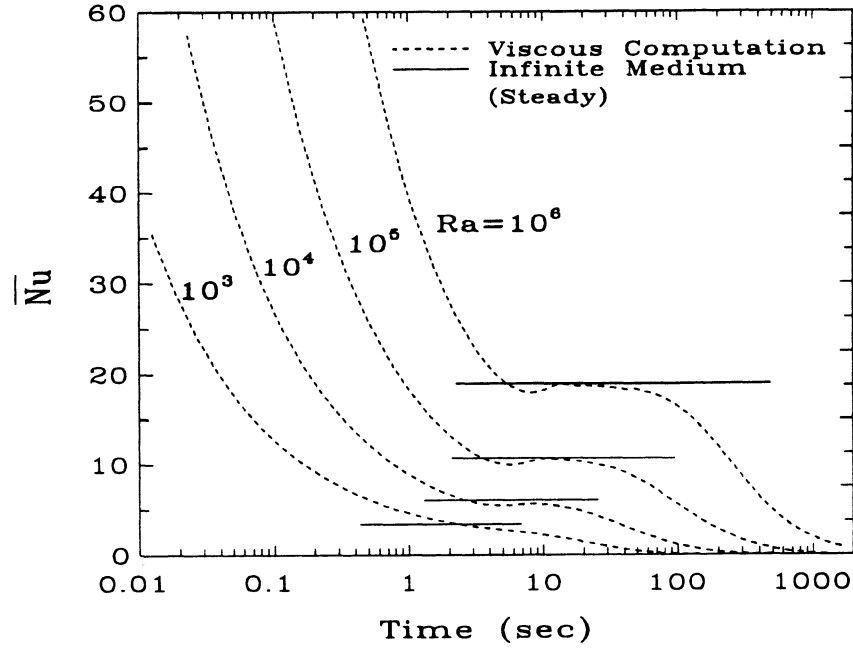


Figure 2.9: Transient  $\overline{Nu}$  (including infinite medium solutions) over the range of Rayleigh numbers for a relative plate size of  $\phi = 0.5$  and relative plate position  $\eta = 1/2$ .

Initially, the velocities in the neighborhood of the heated plate are zero and the only possible mode of heat transfer into the cavity is by conduction. As heat is conducted into the cavity, a thermal boundary layer of thickness  $\delta_T$  forms adjacent to the plate. Considering the individual terms in Equation 2.4 in an order of magnitude sense gives

$$\frac{\Delta T}{\Delta t}, \quad u \frac{\Delta T}{\delta_T}, \quad v \frac{\Delta T}{L} \sim \alpha \frac{\Delta T}{\delta_T^2}, \quad \alpha \frac{\Delta T}{L^2} \quad (2.32)$$

where  $\sim$  implies that the terms on the left side of the equation are of the same order of magnitude as the terms on the right side. The  $u$  and  $v$  velocities are small and the thermal boundary layer thickness is much smaller than the plate length ( $\delta_T \ll L$ ). The remaining terms balance to give an estimate of the thermal boundary layer thickness which is identical to Patterson and Imberger (1984).

$$\delta_T \sim (\alpha \Delta t)^{1/2} \quad (2.33)$$

As energy is conducted into the thermal boundary layer, buoyancy forces will accelerate the fluid over the entire thickness  $\delta_T$ . Considering the  $y$ -momentum equation

$$\frac{v}{\Delta t}, \quad u \frac{v}{\delta_T}, \quad v \frac{v}{L} \sim \frac{1}{\rho} \frac{P}{L^2}, \quad v \frac{v}{\delta_T^2}, \quad v \frac{v}{L^2}, \quad g \beta \Delta T \quad (2.34)$$

For  $Pr > 1$ , the viscous force term  $v v / \delta_T^2$  will dominate over the unsteady inertia force term  $v / \Delta t$  and balance the buoyancy term  $g \beta \Delta T$  to arrive at an estimate for the developing  $v$ -velocity.

$$v \sim \frac{g \beta \Delta T}{Pr} \Delta t \quad (2.35)$$

Considering the energy flows within the thermal boundary layer, a balance results which requires that the energy conducted away from the plate equals the energy convected from the boundary layer yielding the following

$$v \frac{\Delta T}{L} \sim \alpha \frac{\Delta T}{\delta_T^2} \quad (2.36)$$

Combining the previous expressions for the  $v$ -velocity and thermal boundary layer thickness  $\delta_T$  results in an estimate for the duration of the conduction dominated period.

$$\Delta t_c \sim \frac{L^2}{\alpha Ra^{1/2}} \quad (2.37)$$

The above estimate is identical to that obtained by Patterson and Imberger (1980) with the exception that  $L$  is the plate length rather than the overall enclosure height. The above estimate is independent of the enclosure size relative to the plate size. The only restrictions on the above estimate are  $Pr > 1$  and  $\delta_T \ll L$ . The conduction limit duration estimates given by Equation 2.37 superimposed on the transient Nusselt number results are shown below in Figure 2.10. The scale analysis estimates of the conduction limits are in good agreement with the observed time duration of conduction dominated behavior.

The estimate of the duration of the quasi-steady period estimate is considerably more difficult to obtain due to the complex transient behavior of the fluid flow and energy transfers throughout the cavity during the transition to and duration of the quasi-steady period. At the end of the conduction regime,  $\Delta \tau_c \sim L^2/\alpha Ra^{1/2}$  and the  $v$ -velocity becomes

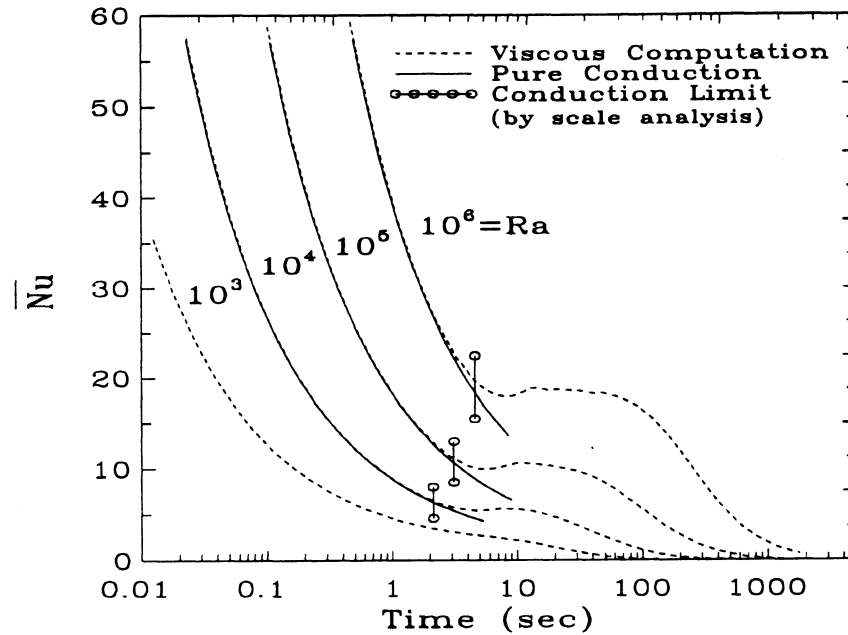


Figure 2.10: Scale analysis estimates for the conduction dominated regime with  $\phi = 0.5$  and  $\eta = 0.5$ .

$$v \sim \frac{g\beta\Delta T}{Pr} \Delta t \sim \frac{g\beta\Delta T}{Pr} \frac{L^2}{\alpha Ra^{1/2}} = \frac{Ra^{1/2}\alpha}{L} \quad (2.38)$$

and the thermal boundary layer thickness is

$$\delta_T \sim \frac{L}{Ra^{1/4}} \quad (2.39)$$

Assuming the volume flow rate is constant through the thermal boundary layer during the quasi-steady period, the volume flow rate  $\dot{Q}$  is given by

$$\dot{Q} \sim v\delta_T \sim \alpha Ra^{1/4} \quad (2.40)$$

The end of the quasi-steady regime is characterized by significant heating of the fluid in the enclosure causing the driving force for heat transfer (temperature difference across the plate) to diminish. Since the enclosure fluid is predominantly stratified throughout the transient, the driving force will diminish when the volume of fluid above the plate is heated. If the volume of fluid above the plate is circulated through the thermal boundary layer, the enclosure will experience a significant temperature rise and the driving force for heat transfer will diminish indicating the ending of the quasi-steady regime. The estimated time for fluid to move from the bottom of the vertical plate to the top is given by

$$t \sim \frac{L}{v} \sim \frac{L\delta_T}{\alpha Ra^{1/4}} \quad (2.41)$$

The quantity  $L\delta_T$  can be viewed as the volume of fluid heated through one pass by the plate. A volume of fluid equivalent to that above the plate will pass through the thermal boundary layer prior to the end of the quasi-steady period. Thus, the estimate for the quasi-steady period duration is given by

$$\Delta t_{qs} \sim \frac{L^2}{\alpha\phi Ra^{1/4}} [1 - (\eta + \phi/2)] \quad (2.42)$$

where  $L$  is the plate length,  $\eta$  is the relative plate position, and  $\phi$  is the relative plate size. (The quasi-steady estimate Equation 2.42 breaks down for the special case when  $\phi = 0.5$  and  $\eta = 0.75$  since the plate would be positioned at the cavity top.) The quasi-steady period duration estimates given by Equation 2.42 superimposed on the transient Nusselt number results are shown below in Figure 2.11. The estimates agree well with the observed end

of the quasi-steady period.

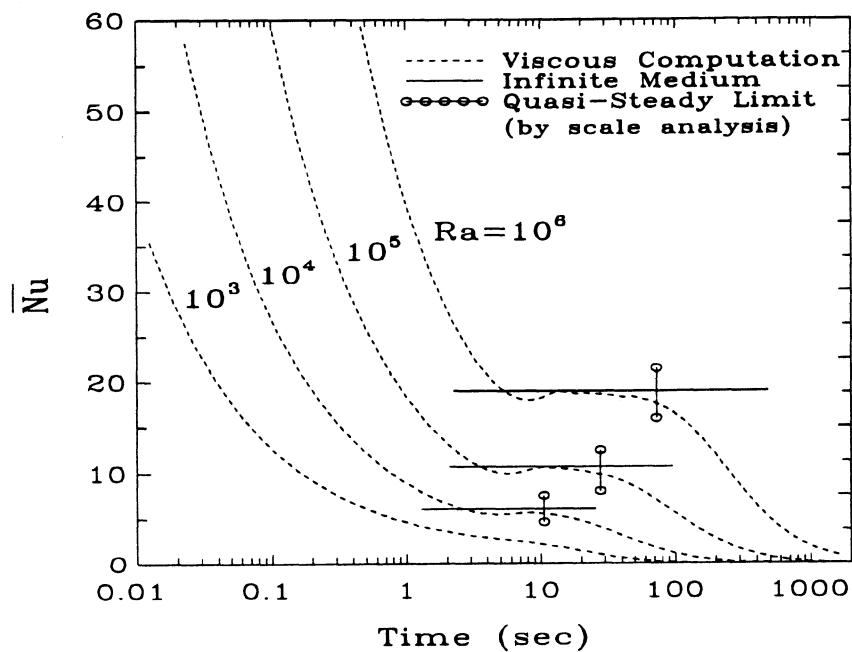


Figure 2.11: Scale analysis estimates for the quasi-steady regime with  $\phi = 0.5$  and  $\eta = 0.5$ .

The characteristics of the transient heat transfer process for the conduction and quasi-steady regimes have been determined along with time estimates predicting the duration of the regimes. Now the dominant characteristics of the decay period will be identified. The analysis of the decay period begins by considering the heat transfer from the plate as given by Equation 2.43.

$$q = k \frac{\partial T}{\partial x} \sim k \frac{(T_w - \bar{T})}{\delta_T} \sim \frac{\overline{Nu} k}{L} (T_w - T_o) \quad (2.43)$$

where  $\bar{T}$  is the bulk cavity temperature found from Equation 2.10.

Because the thermal and viscous boundary layers will grow as the bulk temperature in the cavity rises,  $\delta_T$  will not be constant during the decay period. The expression for the thermal boundary layer thickness  $\delta_T \sim L/Ra^{1/4}$  can be modified to account for this increase in thickness. Thus, defining a modified thermal boundary layer thickness expression as follows

$$\bar{\delta}_T \sim \frac{L}{\overline{Ra}^{1/4}} = \frac{L}{[g \beta L^3 (T_w - \bar{T}) / \nu \alpha]^{1/4}} \quad (2.44)$$

where  $\overline{Ra}$  is the Rayleigh number based on the difference  $(T_w - \bar{T})$  similar to that used by Hall, et al. (1988). The Rayleigh number  $\overline{Ra}$  based on the difference between the plate and bulk cavity temperatures will become smaller as the bulk temperature increases; consequently, the thermal boundary layer thickness increases. Therefore, the energy balance becomes

$$\frac{k(T_w - \bar{T}) \overline{Ra}^{1/4}}{L} \sim \frac{\overline{Nu} k}{L} (T_w - T_o) \quad (2.45)$$

and the resulting expression for the average Nusselt number

$$\overline{Nu} \sim \frac{(T_w - \bar{T})}{(T_w - T_o)} \overline{Ra}^{1/4} = (1 - \bar{T}^*) \overline{Ra}^{1/4} = (1 - \bar{T}^*)^{5/4} Ra^{1/4} \quad (2.46)$$

where  $\bar{T}^* = (\bar{T} - T_o)/(T_w - T_o)$  which is proportional to the fraction ( $f$ ) of the cavity heated to temperature  $T_w$ . The above expression for the average Nusselt number is not useful in its current form because the bulk cavity temperature is not known a priori. The overall energy balance on the enclosure is

$$kA \frac{(T_w - \bar{T})}{\bar{\delta}_T} \sim mc \frac{d\bar{T}}{dt} = mc(T_w - T_o) \frac{df}{dt} \quad (2.47)$$

Substituting in the above expression for thermal boundary layer thickness and rearranging yields,

$$\frac{kARa^{1/4}}{mcL} (1-f)^{5/4} \sim \frac{df}{dt} \quad (2.48)$$

where  $(1-f) = (T_w - \bar{T})/\bar{\delta}_T$ .

Solving the ordinary differential equation with the initial condition  $f \sim 0$  @  $t = 0$  results in an expression for  $f$ .

$$f = (1 - \bar{T}^*) \sim \left[ 1 + \frac{\alpha Ra^{1/4} t}{2HW} \right]^{-4} \quad (2.49)$$

When combined with the above expression for the average Nusselt number gives

$$\overline{Nu} \sim \left[ 1 + \frac{\alpha Ra^{1/4} t}{2HW} \right]^{-5} Ra^{1/4} \quad (2.50)$$

Equation 2.50 is the resulting scale estimate of the heat transfer during the decay period. The estimate given by Equation 2.50 differs from that obtained by Hall, et al. (1988) for the differentially heated cavity.

The heat transfer during the decay period is assumed to be proportional to Equation 2.50.

$$\overline{Nu} = C_1 \left[ 1 + \frac{\alpha Ra^{1/4} t}{2HW} \right]^{-5} Ra^{1/4} \quad (2.51)$$

The constant  $C_1$  in Equation 2.51 is determined by least squares from the decay period results for each Rayleigh number. The results are shown in Table 2.2.

$Ra$	$C_1$	$r^2$ (%)
$10^3$	0.7634	96.5
$10^4$	0.8207	98.8
$10^5$	0.7975	99.0
$10^6$	0.8035	99.1
Composite	0.7936	99.5

Table 2.2: Constant for Equation 2.51 for  $\phi = 0.5$  and  $\eta = 0.5$ .

where  $r^2$  represents the percent of variation in the response ( $\overline{Nu}$ ) explained by the dimensionless predictor group. Table 2.2 shows that the worst case is at  $Ra=10^3$ . As mentioned previously, this case is largely conduction dominated throughout the entire transient. Excellent agreement is obtained at the higher Rayleigh numbers. A composite slope is obtained by fitting the results for all Rayleigh numbers. Figure 2.12 shows the resulting fit of the decay regime based on Equation 2.51 (and composite constant value of  $C_1$ ) as well as the conduction and quasi-steady estimates compared to the actual transient computations. The agreement between the actual and predicted heat transfer over the decay period is excellent. Overall, the actual transient heat transfer process is characterized very well by the piecewise approximation over each regime.

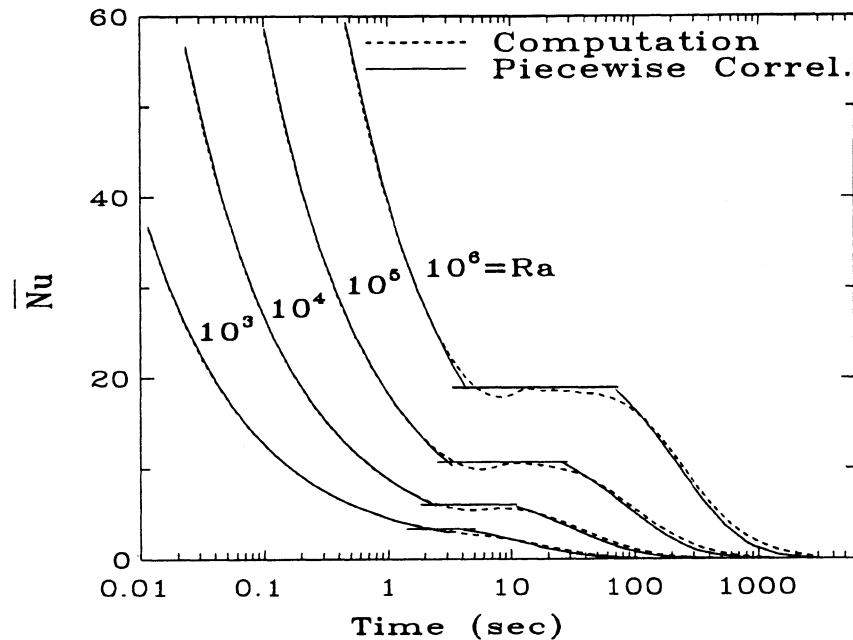


Figure 2.12: Piecewise approximation and the actual transient heat transfer for  $10^3 \leq Ra \leq 10^6$  for  $\phi = 0.5$  and  $\eta = 0.5$ ;  $C_1 = 0.7936$ .

To complete the analysis of this geometric configuration, flow field and temperature field results are presented. A common feature in the velocity flow field is a clockwise rotating vortex. The location of the vortex hub depends on the magnitude of the Rayleigh number and the instant in time during the transient. The temperature field is characterized by a heated plume which rises above the plate eventually penetrating across the top and down to the bottom of the enclosure. A relatively high degree of thermal stratification is

maintained throughout the transient. Field results for each order of Rayleigh number will be given in terms of stream function<sup>2</sup> and temperature contours at two times during the transient. The first sequence of plots considers a period in the transient ( $t^*=5.5$ ) where peak velocities are occurring. Figure 2.13 shows the stream function results for four different Rayleigh numbers.

In each case, there is a single clockwise rotating vortex. At low Rayleigh numbers, the hub of the vortex is in the center of the cavity. As the Rayleigh number increases, the strength or circulation of the vortex increases and its center moves closer to the boundary layer exiting from the heated plate. In general, a boundary layer of upward moving fluid is established near the heated plate (supply side). The fluid continues to accelerate above the plate and peak velocities are typically reached at a point approximately midway between the plate and enclosure top. As the fluid moves across the top, a horizontal boundary layer is established. The fluid quickly loses its momentum and thermal energy to the relatively cooler surrounding fluid; subsequently, the fluid falls (return side) and eventually becomes entrained in the supply side boundary layer adjacent to the heated plate.

Figure 2.14 shows the corresponding temperature results at  $t^*=5.5$ . The isotherms for low Rayleigh numbers ( $Ra \leq 10^3$ ) show minimal distortion validating the previous assertion that the heat transfer is conduction dominated throughout the entire transient. As the Rayleigh number increases, the thermal plume rising above the plate becomes more distinct and distorted due to the stronger circulation of the vortex.

---

2 The stream function  $\psi$  is defined by  $u = \partial\psi/\partial y$ ,  $v = -\partial\psi/\partial x$ . This definition generates a contour which is everywhere tangent to the local velocity vector. The change in stream function is an exact differential given by  $\Delta\psi = \int (V \cdot n) d\Gamma$  where  $V$  is the velocity vector and  $\Gamma$  is a general path of integration.

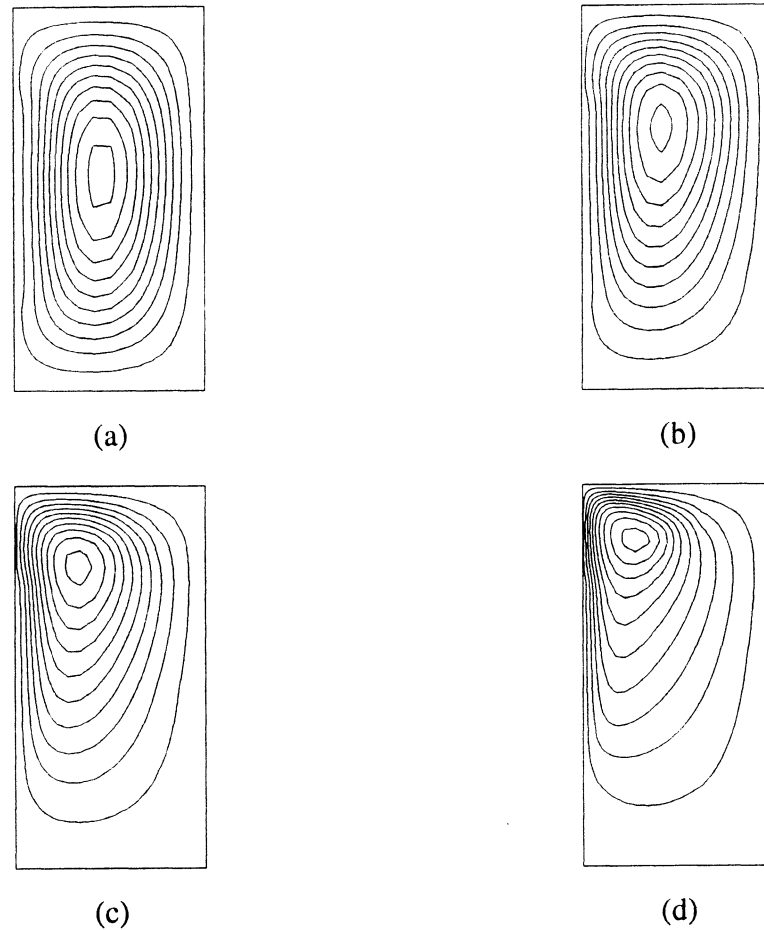


Figure 2.13: Stream function contours at ( $t^*=5.5$ ): (a)  $Ra=10^3$ ,  $t=4.22$  sec;  $\Psi_{\min} = -0.0342$ ,  $\Delta\Psi = 0.0036$ ,  $\Psi_{\max} = -0.0018$  i.e.  $-0.0342(0.0036)-0.0018$ ; (b)  $Ra=10^4$ ,  $t=6.20$  sec,  $-0.0665(0.007)-0.0035$ ; (c)  $Ra=10^5$ ,  $t=9.09$  sec,  $-0.0684(0.0072)-0.0036$ ; (d)  $Ra=10^6$   $t=13.33$  sec,  $-0.0532(0.0056)-0.0028$ .

The sequence of plots in Figures 2.15 and 2.16 show stream function and isotherms at a point in time which corresponds to the end of the quasi-steady period (as predicted by Equation 2.51). (Note, results for  $Ra=10^3$  are omitted since they do not differ significantly from those shown in Figures 2.13 and 2.14.) Figure 2.15 shows the stream function results at the end of the respective quasi-steady regimes.

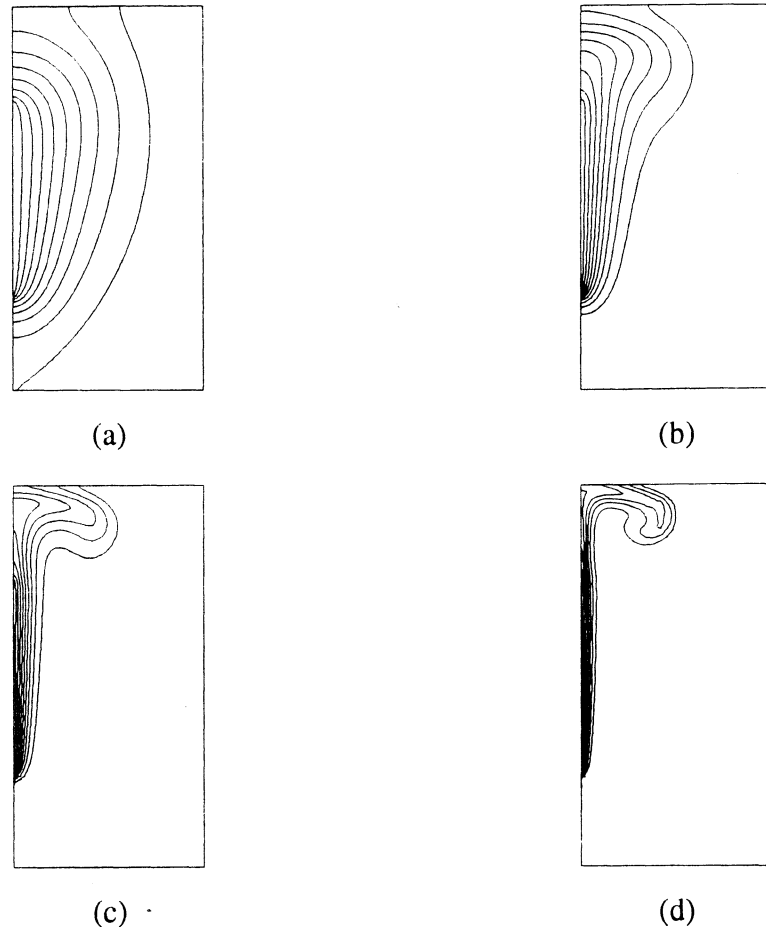


Figure 2.14: Temperature contours at ( $t^*=5.5$ ): (a)  $Ra=10^3$ ,  $t=4.22$  sec;  $T_{\min} = 0.1$ ,  $\Delta T=0.1$ ,  $T_{\max} = 1.0$  i.e. 0.1(0.1)1.0; (b)  $Ra=10^4$ ,  $t=6.20$  sec, 0.1(0.1)1.0; (c)  $Ra=10^5$ ,  $t=9.09$  sec, 0.1(0.1)1.0; (d)  $Ra=10^6$   $t=13.33$  sec, 0.1(0.1)1.0.

By the end of the quasi-steady period, the magnitude of the velocities in the cavity are beginning to diminish. At low Rayleigh numbers ( $Ra \leq 10^4$ ), a single re-circulation zone is maintained in the central portion of the enclosure. At higher Rayleigh numbers ( $Ra > 10^4$ ), the center of the re-circulating vortex has become elongated and streamlines opposite the plate have buckled. The fluid moving across the enclosure top in the horizontal boundary layer maintains more of its momentum and thermal character since the surrounding fluid

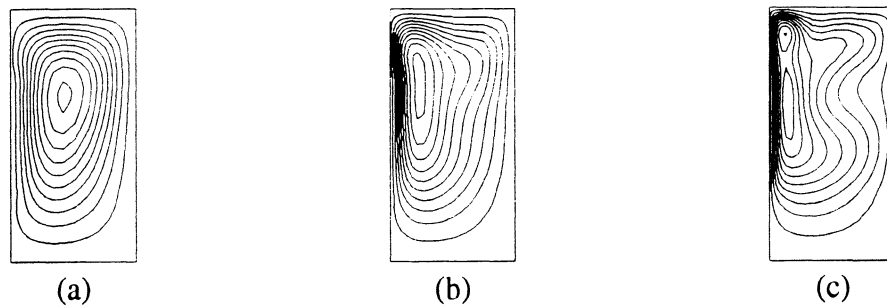


Figure 2.15: Stream function contours at the end of quasi-steady regime: (a)  $Ra=10^4$ ,  $t=10.64$  sec;  $\psi_{\min} = -0.057$ ,  $\Delta\psi = 0.006$ ,  $\psi_{\max} = -0.003$  i.e.  $-0.057(0.006)-0.003$ ; (b)  $Ra=10^5$ ,  $t=27.77$  sec,  $-0.0314(0.0033)-0.0017$ ; (c)  $Ra=10^6$   $t=72.47$  sec,  $-0.020(0.0021)-0.00105$ .

is much warmer at this time. When the fluid reaches the right vertical wall, it is reflected back toward the cavity center. The depth of this return penetrating layer of fluid is determined by the strength of the re-circulation zone adjacent to the heated plate relative to the strength of the penetrating layer. For the  $Ra=10^5$  case, the return side fluid in the re-circulating zone adjacent to the plate entrains a significant amount of the weaker penetrating layer. In the  $Ra=10^6$  case, the return side fluid in the re-circulating zone adjacent to the plate is not able to completely entrain the fluid flowing from the penetrating layer. Thus, a portion of this penetrating layer is reflected back before it loses its momentum and thermal energy to the relatively cooler fluid in the lower portion of the enclosure. It is subsequently entrained into the supply side boundary layer at the base of the plate.

Figure 2.16 shows the corresponding temperature results at the end of the quasi-steady regime. The isotherms at the end of the quasi-steady period indicate that the bulk temperature in the cavity is beginning to increase significantly. The local temperature difference across the plate is beginning to decrease from the top down. The reduction in

driving force coincides with the start of heat transfer to decay from the steady infinite medium solution. A relatively high degree of thermal stratification in the enclosure is maintained.

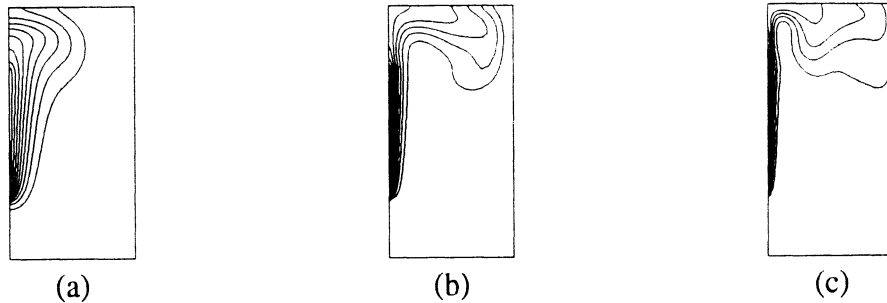


Figure 2.16: Temperature contours at the end of quasi-steady regime: (a)  $Ra=10^4$ ,  $t=10.64$  sec;  $T_{\min}=0.1$ ,  $\Delta T=0.1$ ,  $T_{\max}=1.0$  i.e. 0.1(0.1)1.0; (b)  $Ra=10^5$ ,  $t=27.77$  sec, 0.1(0.1)1.0; (c)  $Ra=10^6$   $t=72.47$  sec, 0.1(0.1)1.0.

The results presented for the two periods considered were intended to show behavior during times when the velocity field is a maximum and when the temperature field is changing significantly. Although the geometry and magnitude of the Rayleigh number is different in this study, the results presented here show qualitative agreement with those of Khalilollahi and Sammakia.

The results thus far have focused on a relative plate position of  $\eta = 0.5$ . It is also of interest to observe the effect of altering the vertical plate position. The vertical plate position was moved to a lower and higher relative position ( $\eta = 0.25, 0.75$ ). The behavior of the heat transfer/fluid flow process during the initial transient is identical to the centered plate case. The pure conduction limit scale estimate given by Equation 2.37 is valid regardless of the vertical plate position. The effects of the vertical plate position are not apparent until the quasi-steady regime is well underway. When the plate is positioned

high in the cavity ( $\eta = 0.75$ ), the duration of the quasi-steady regime decreases and when the plate is low in the cavity ( $\eta = 0.25$ ) the duration of the quasi-steady regime increases as illustrated in Figure 2.17.

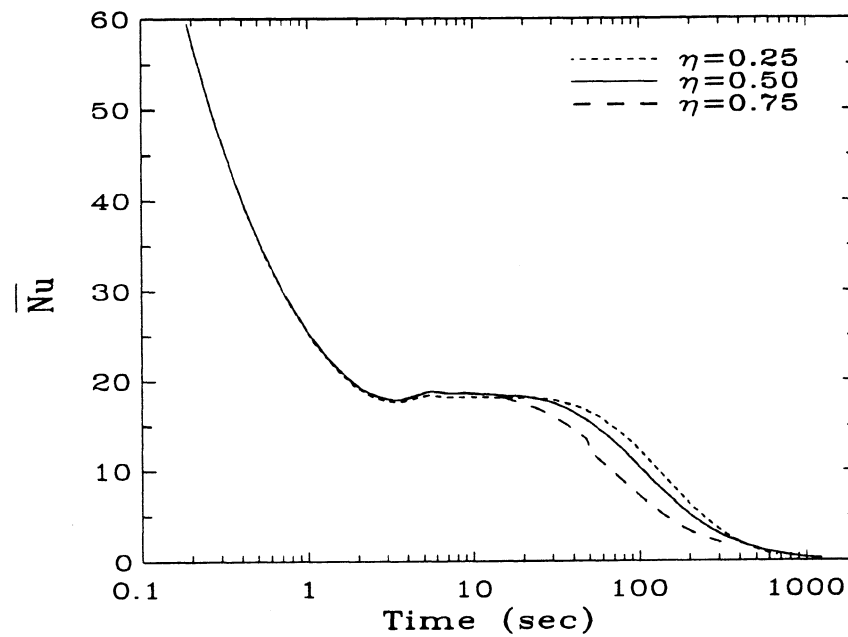


Figure 2.17: Effect of the vertical plate position on the Average Nusselt number for  $Ra=10^6$  and  $\phi = 0.5$ .

Similar to the centered plate case, the heat transfer characteristics of the decay period are correlated to be of the form given in Equation 2.51. The constant for Equation 2.51 determined by least squares over the range of Rayleigh numbers  $10^4 \leq Ra \leq 10^6$  is given in Table 2.3 for each vertical plate position.

$\eta$	$C_1$	$r^2$ (%)
0.25	0.9690	98.8
0.50	0.7936	99.5
0.75	0.6396	98.3

Table 2.3: Average constants for Equation 2.51 for  $\phi = 0.5$  and  $10^4 \leq Ra \leq 10^6$ .

It is clear from Figure 2.17 and the constants given in Table 2.3 that the heat transfer during the decay period depends on the vertical plate position (of course the starting time of the decay period also depends on the plate position). There is a strong correlation between the constants obtained for each relative plate position and the plate position but the gross nature of scale analysis does not allow this effect to be predicted a priori.

By observing the magnitude of the constants in Table 2.3, it is clear that the heat transfer for the upper plate position is smaller than that of the mid and lower plate positions due to the flow impedance caused by the cavity top on the exiting boundary layer from the plate. The influence of the cavity top becomes less important as the plate position moves lower in the cavity; consequently, the magnitude of the heat transfer increases. This is shown by considering the peak velocities in the direction parallel to the plate. Table 2.4 gives the temporal maximum values of the  $v$ -velocity and the time in which they occur for  $Ra=10^6$ .

$\eta$	$t^*$	$v_{\max}^*$
0.25	5.91	0.694
0.50	5.03	0.537
0.75	4.51	0.308

Table 2.4: Maximum  $v$ -velocities for  $Ra=10^6$  and the three vertical plate positions.

When the plate is situated at the base of the cavity ( $\eta = 0.25$ ), higher velocities can be achieved and maintained due to the longer vertical distance for the flow to accelerate, consequently; the heat transfer is higher than that for the upper plate positions. Also when the plate is at the base of the cavity, there is little interruption or "choking" of the flow due to the presence of the cavity base because the majority of fluid entrained by the plate boundary layer originates from the "side" of the plate and not below the plate. The inflow of fluid to the boundary layer from the side is illustrated by Figure 2.18.

The fluid near the plate accelerates upward due to the energy input from the heated plate. After the fluid exits from the heated plate, thermal energy is no longer added to the fluid stream; however, the velocity reaches a peak above the plate due to a minimal loss

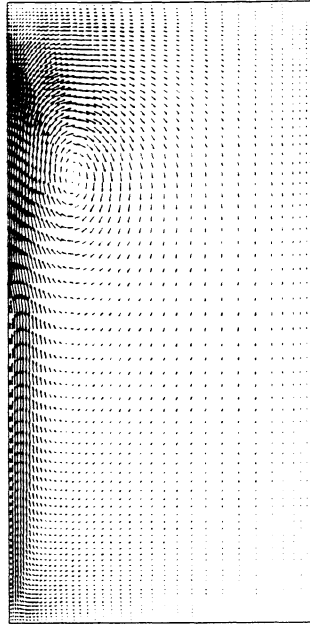


Figure 2.18: Velocity vectors at  $t^*=5.0$  for  $\phi = 0.50$ ,  $\eta = 0.25$ , and  $Ra=10^6$ .

of thermal energy and the lack of significant viscous shear caused by the absence of the solid plate surface. The fluid begins to decelerate and begin to move right due to the presence of the enclosure top. As the fluid moves along the enclosure top, it quickly loses momentum and thermal energy to the cooler stagnant fluid in the far right side of the cavity. As the fluid stream cools, it begins to descend and a portion of the descending fluid stream becomes entrained by the vertical boundary layer established by the heated plate. The side entrainment results in the formation of a clockwise vortex identical to that shown in Figures 2.13 and 2.15.

Figure 2.19 shows the resulting velocity vector field at  $t^*=5.0$ . The flow structure is similar to that shown in Figure 2.18. In this case, the fluid is not free to accelerate along the complete length of the plate. A clockwise rotating vortex is maintained adjacent to the upper portion of the plate.

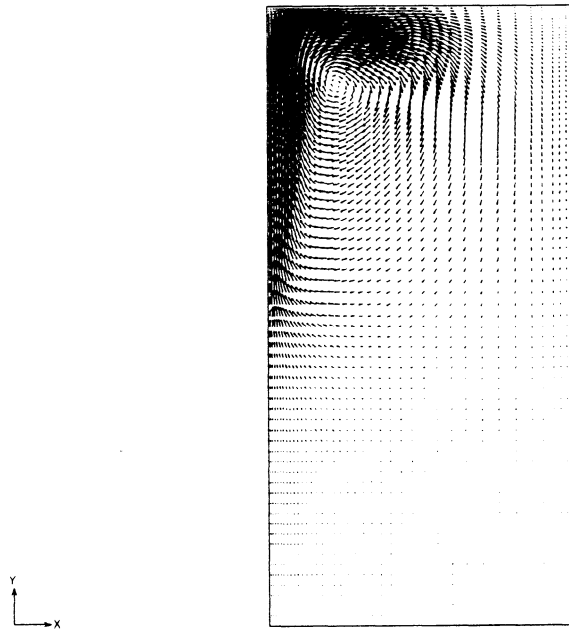


Figure 2.19: Velocity vectors at  $t^*=5.0$  for  $\phi = 0.50$ ,  $\eta = 0.75$ , and  $Ra=10^6$ .

Sources positioned low in the cavity result in higher velocities in the neighborhood of the plate and higher heat transfer rates. When the base of the plate is in contact with the cavity bottom, there is no significant degradation of the boundary layer flow because the majority of the fluid entering the boundary layer is entrained from the side of the plate and not the bottom.

## 2.4 Conclusions

The transient natural convection heat transfer/fluid flow characteristics from an isothermal vertical flat plate in an adiabatic square enclosure have been considered. The strongly coupled system of governing partial differential equations have been solved by a finite element method. The transient heat transfer response can be characterized by three distinct regimes: pure conduction, quasi-steady, and decay. The complete transient can be characterized by three piecewise curves representing a pure conduction solution, infinite medium solution, and a correlation for the decaying period. Scale analysis is used to develop order-of-magnitude estimates for the time duration of each regime. In addition, scale analysis is used to identify the relevant parameters to correlate the decay period. For low Rayleigh numbers ( $Ra \leq 10^3$ ) the heat transfer process is conduction dominated throughout the complete transient.

The relative size of the enclosure was varied to observe the effects of the bounding walls on the heat transfer from the vertical flat plate source. It is clear that the bounding walls will eventually influence the heat transfer process. Large enclosures are able to maintain the quasi-steady period for longer periods of time but eventually the heat transfer process decays as the fluid in the enclosure is significantly heated. The enclosure must be at least 1.5 times the size of the plate in order for the heat transfer to approach the infinite medium case (enclosures of this size order have very short quasi-steady periods).

The relative vertical position of the plate in the cavity has a definite effect on the transient heat transfer characteristics from the plate. When the plate is high in the cavity, the rate of heat transfer from the plate is reduced due to lower flow rates through the

boundary layer caused by the cavity top impeding the outlet of the plate boundary layer. Also, the cavity is stratified, therefore; a higher positioned plate will "see" a reduction in the driving force for heat transfer.

## References

- 
- Becker, E. B., Carey, G. F., Oden, J. T., Finite Elements: An Introduction, Prentice-Hall, Inc., (1981).
- Bejan, A., Convection Heat Transfer, John Wiley & Sons, (1984).
- Boussinesq, J., *Theorie de la Chaleur*, **2**, Gauthier-Villars, Paris, (1903).
- Burnett, D. S., Finite Element Analysis, Addison-Wesley Publishing, (1988).
- Carey, G. F., Oden, J. T., Finite Elements: Fluid Mechanics, Prentice-Hall, Inc., (1986).
- Churchill, S. W., Chu, H. H. S., "Correlating Equations for Laminar and Turbulent Free Convection from a Vertical Plate", *International Journal of Heat and Mass Transfer*, **18** pp. 1323, (1975).
- FIDAP, A fluid dynamics analysis package by Fluid Dynamics International, Inc. 500 Davis St. Suite 600, Evanston, IL, 60201.
- Gray, D. D., Giorgini, A., "The Validity of The Boussinesq Approximation for Liquids and Gases", *International Journal of Heat and Mass Transfer*, **19**, pp. 545-551, (1976).
- Hall, J. D., Bejan, A., Chaddock, J. B., "Transient Natural Convection In a Rectangular Enclosure With One Heated Side Wall", *International Journal of Heat and Fluid Flow*, **9**(4), pp. 396-404, (1988).
- Khalilollahi, A., Sammakia, B., "Unsteady Natural Convection Generated by a Heated Surface Within an Enclosure", *Numerical Heat Transfer*, **9**, pp. 715-730, (1986).
- Nicolette, V. F., Yang, K. T., "Transient Cooling by Natural Convection in a Two Dimensional Square Enclosure", *International Journal of Heat and Mass Transfer*, **28**(9), pp. 1721-1732, (1985).
- Oberbeck, A., "Über die Wärmeleitung der Flüssigkeiten bei Berücksichtigung der Strömungen infolge von Temperatur Differenzen", *Annals of Physical Chemistry*, **7**, pp. 271-292, (1879).

Patterson, J., Imberger, J., "Unsteady Natural Convection In a Rectangular Cavity", *Journal of Fluid Mechanics*, **100**, pp. 65-86, (1980).

Reindl, D. T., Beckman, W. A., Mitchell, J. W., Rutland, C. J., "Benchmarking Transient Natural Convection In An Enclosure", *1991 ASME National Heat Transfer Conference Minneapolis*, (July 1991).

Zienkiewicz, O. C., The Finite Element Method, McGraw-Hill, London, (1977).

### 3 Coiled Tube In a Cylindrical Enclosure

A crucial element in an active thermal solar energy system is storage. Since the loads on a system do not coincide with the resource availability, a means to store the energy for later use is essential. Many techniques and configurations have been devised to store thermal energy but detailed analysis of the techniques are limited. Two common sensible storage techniques are direct and indirect contact storage tanks. In a direct contact system, the storage tank is charged and discharged by hot and cold fluid streams flowing directly in and out of the storage volume. An advantage of the direct contact scheme is that no heat exchanger is required to charge or discharge energy from the storage tank. In contrast to direct contact storage schemes, indirect storage requires the use of heat exchangers. Often times indirect storage designs utilize heat exchangers immersed in the storage volume to charge and discharge energy from the tank.

The vast majority of research activity on thermal storage in the literature have focused on analyzing direct contact thermal storage tanks (Lavan and Thompson 1977, Sliwinski 1978, Cabelli 1977, Young and Baughn 1981, Chan, et al. 1983, Guo 1985, and Lightstone, et al. 1989) while the studies for indirect storage tanks are sparse (Feiereisen 1983, and Farrington 1986). (For a summary of thermal storage research see Radosevich and Wyman 1983.) The primary reason for this imbalance in research efforts lies in the fact that direct contact storage strategies are usually more efficient; however, some system configurations dictate the need for indirect contact storage. For example, if the collector loop fluid is not compatible with the store fluid, a heat exchanger is required to physically separate the two mediums.

Feiereisen, et al. (1983) experimentally studied four immersed heat exchanger coil configurations. The storage tank performance was observed while varying heat exchanger location, orientation, and flow rates. Correlations of heat exchanger performance, in the form of Nusselt number as a function of Rayleigh number, were presented. The Nusselt and Rayleigh numbers were defined based on a log-mean temperature difference between the heat exchanger and tank temperatures. Since this definition is not possible in the current investigation, the current results can not be compared with Feiereisen, et al.

Farrington, et al. (1986) built on the work of Feiereisen by performing experiments to determine overall loss coefficients and heat transfer performance from immersed coils in two commercial thermal storage tanks. Again general conclusions are drawn regarding observed performance of the tanks and the immersed coil heat exchangers. Farrington also found that reduced heat exchanger flow rates enhanced charging performance.

These studies do not permit detailed investigation of the transient fluid flow and heat transfer processes within the enclosures. The conclusions drawn in these two studies rely on observing "bulk" quantities (i.e., measuring heat exchanger inlet/outlet temperatures and flow rates). This approach limits the depth of understanding that can be achieved in studying the heat transfer and fluid flow from an immersed coil heat exchanger. The focus of the current work is to gain a fundamental understanding into the physics of the heat transfer and fluid flow of a single immersed coil heat exchanger in an enclosure. By understanding the transient heat transfer and fluid flow from the immersed coil, more accurate simplified models to predict storage behavior in solar system simulations can be sought. In addition, techniques to minimize charge time and promote stratification may be identified.

The objective of this chapter is to gain insight into the fundamental physics of fluid flow and heat transfer from an immersed coil heat exchanger in an enclosure and identify relevant parameters to correlate the transient heat transfer results. The geometric configuration is shown in Figure 1.7. Although, the heat exchanger/tank configuration considered here is less complex than the configurations considered by Feiereisen and Farrington, the same methodology of analysis used here can be applied to more complex tank configurations. To accomplish the objectives, the governing time dependent Navier-Stokes and energy equations are solved by the same method considered in Chapter 2. Solutions are obtained over a range of Rayleigh numbers ( $10^3 \leq Ra_D \leq 10^6$ ) for a fixed enclosure size and heat exchanger location. The range of Rayleigh numbers is selected to include behavior from conduction dominated ( $Ra_D \leq 10^3$ ) to the higher end of the laminar regime ( $Ra_D \leq 10^6$ ). The author is not aware of any numerical computations or experiments performed on the geometry considered here.

### **3.1 Governing Equations for Cylindrical Enclosure**

Similar to the rectangular cavity, the computational domain for the cylindrical cavity is shown in Figure 3.1. The water filled enclosure is initially quiescent at a uniform temperature  $T_o$ . At time zero, a step change in the wall temperature of the immersed heat exchanger to  $T_w$  begins to influence the fluid in the enclosure. The final state is a quiescent flow field at a temperature equal to the heat exchanger coil temperature. These boundary conditions permit axi-symmetric assumptions which greatly reduces the computations necessary to solve the problem. (In a real thermal storage tank, the flow is inherently three dimensional because there is an azimuthal variation in temperature as the fluid moves through the interior of the heat exchanger.)

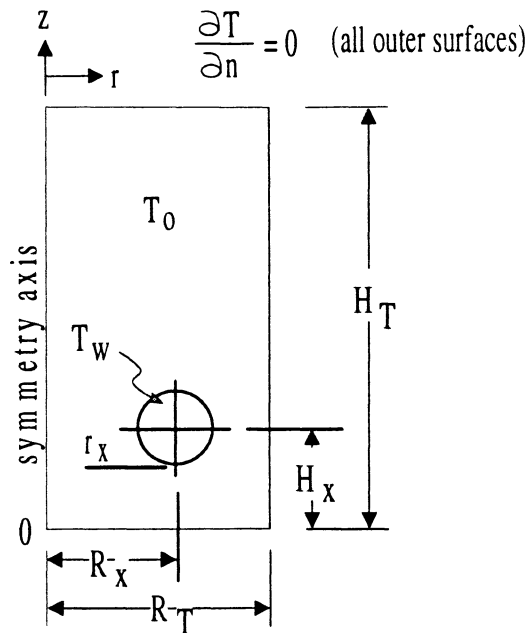


Figure 3.1: Computational domain for the cylindrical enclosure.

The tank radius,  $R_T$  is half the tank height  $H_T$  (a unit aspect ratio enclosure). The tank height is six times larger than the exchanger tube diameter  $D$  and twice the coil diameter  $R_x$ . The heat exchanger is elevated to a position  $H_x$  equal to  $0.3H_T$  and has a radius  $R_x$  equal to  $0.25H_T$ . Thus, the complete geometric problem is scaled based on the magnitude of the Rayleigh number. The primary quantities of interest are average heat flux from the exchanger and bulk tank temperature. The Boussinesq working fluid (water) has a Prandtl number of 5.42.

Similar to the rectangular coordinate case, the governing equations can be non-dimensionalized using the variables shown in Table 3.1.

$r^* = r/D$	$z^* = z/D$
$v_r^* = v_r/U$	$v_z^* = v_z/U$
$T^* = (T - T_o)/(T_w - T_o)$	$P^* = P/\rho U^2$
$t^* = tU/D$	$U = \sqrt{g \beta (T_w - T_o) D}$

Table 3.1: Cylindrical coordinate variable Non-dimensionalization.

After dropping the \* superscripts, the governing dimensionless differential equations for this configuration are

Conservation of Mass:

$$\frac{1}{r} \frac{\partial}{\partial r} (r v_r) + \frac{\partial}{\partial z} (v_z) = 0 \quad (3.1)$$

Radial Momentum:

$$\frac{\partial v_r}{\partial t} + v_r \frac{\partial v_r}{\partial r} + v_z \frac{\partial v_r}{\partial z} = -\frac{\partial P}{\partial r} + \sqrt{\frac{Pr}{Ra_D}} \left[ \frac{1}{r} \frac{\partial}{\partial r} \left( r \frac{\partial v_r}{\partial r} \right) + \frac{\partial^2 v_r}{\partial z^2} - \frac{v_r}{r^2} \right] \quad (3.2)$$

Axial Momentum:

$$\frac{\partial v_z}{\partial t} + v_r \frac{\partial v_z}{\partial r} + v_z \frac{\partial v_z}{\partial z} = -\frac{\partial P}{\partial z} + \sqrt{\frac{Pr}{Ra_D}} \left[ \frac{1}{r} \frac{\partial}{\partial r} \left( r \frac{\partial v_z}{\partial r} \right) + \frac{\partial^2 v_z}{\partial z^2} \right] + T \quad (3.3)$$

Energy:

$$\frac{\partial T}{\partial t} + v_r \frac{\partial T}{\partial r} + v_z \frac{\partial T}{\partial z} = \frac{1}{\sqrt{Ra_D Pr}} \left[ \frac{1}{r} \frac{\partial}{\partial r} \left( r \frac{\partial T}{\partial r} \right) + \frac{\partial^2 T}{\partial z^2} \right] \quad (3.4)$$

Boundary Conditions:

@ $r = 0$	$0 \leq z \leq H_T/D$	$v_r = 0, \partial v_z / \partial r = 0$	$\partial T / \partial n = 0$
@ $r = R_T/D$	$0 \leq z \leq H_T/D$	$v_r = v_z = 0$	$\partial T / \partial n = 0$

@ $z = 0$	$0 \leq r \leq R_T/D$	$v_r = v_z = 0$	$\partial T/\partial n = 0$
@ $z = H_T/D$	$0 \leq r \leq R_T/D$	$v_r = v_z = 0$	$\partial T/\partial n = 0$
@ <i>the surface of heat exchanger</i>		$v_r = v_z = 0$	$T = 1$

**Initial Conditions:**

all $r$	all $z$	$v_r = v_z = 0$	$T = 0$
---------	---------	-----------------	---------

The average Nusselt number is the integral of the local flux over the circumference of the heat exchanger boundary as given by

$$\overline{Nu} = \int_0^{2\pi} \frac{\partial T}{\partial n} \Big|_w d\theta \quad (3.5)$$

where  $\theta$  is the angular coordinate around the tube. The definition of the average Nusselt number is based on the initial temperature difference ( $T_w - T_o$ ) and not the temperature difference ( $T_w - \bar{T}$ ) where  $\bar{T}$  is the bulk temperature in the enclosure.

FIDAP is used to solve the governing differential equations in a primitive variable formulation using a Galerkin finite element approximation. The elements are nine node quadrilaterals with the quadratic bases for both the velocity and temperature components. The resulting system of ordinary differential equations solved by an adaptive second order implicit trapezoid rule.

### 3.2 Results

The following section presents the results for the cylindrical enclosure computations. A significant effort has been expended to assure that the final solutions are independent of the spatial and temporal computational meshes. The mesh refinement techniques used here are identical to those given by Reindl, et al. (1991). The spatial mesh employed in the present computations is shown in Figure 3.2.

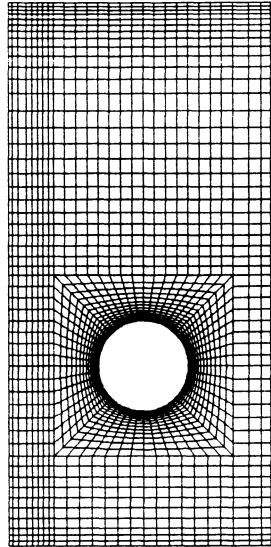


Figure 3.2: Axis symmetric mesh for cylindrical enclosure.

All computations are carried out on a Cray Y-MP8/864 computer. For the above mesh, the CPU time required to obtain transient results depends on the magnitude of the Rayleigh number. Typical run times ranged from three hours ( $Ra_D=10^3$ ) to more than twenty hours ( $Ra_D=10^6$ ). Computations at higher Rayleigh numbers were not attempted due to resource limitations.

A typical response for the transient heat transfer from the immersed coil is shown in Figure 3.3. Qualitatively, the transient heat transfer looks identical to that from the flat plate in a rectangular enclosure. Again there are three distinct heat transfer regimes: conduction, quasi-steady, and decay.

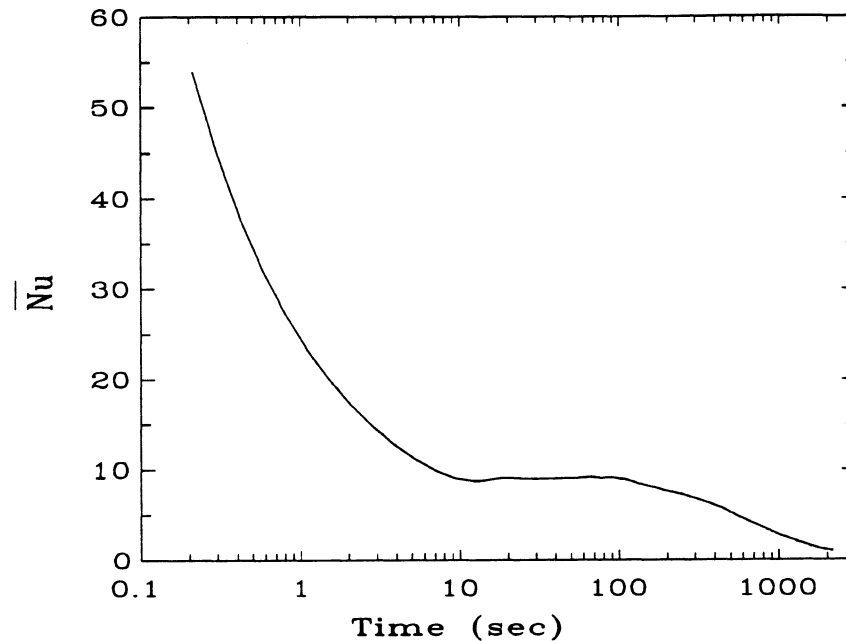


Figure 3.3: Transient heat transfer response for  $Ra_D=10^5$ .

### 3.2.1 Limiting Cases

There are two limiting cases to validate the pure conduction and quasi-steady regimes. Figure 3.4 shows the transient heat transfer response and pure conduction solutions for a range of Rayleigh numbers. It is clear that the early transient is conduction dominated (which is independent of the interior heat exchanger location).

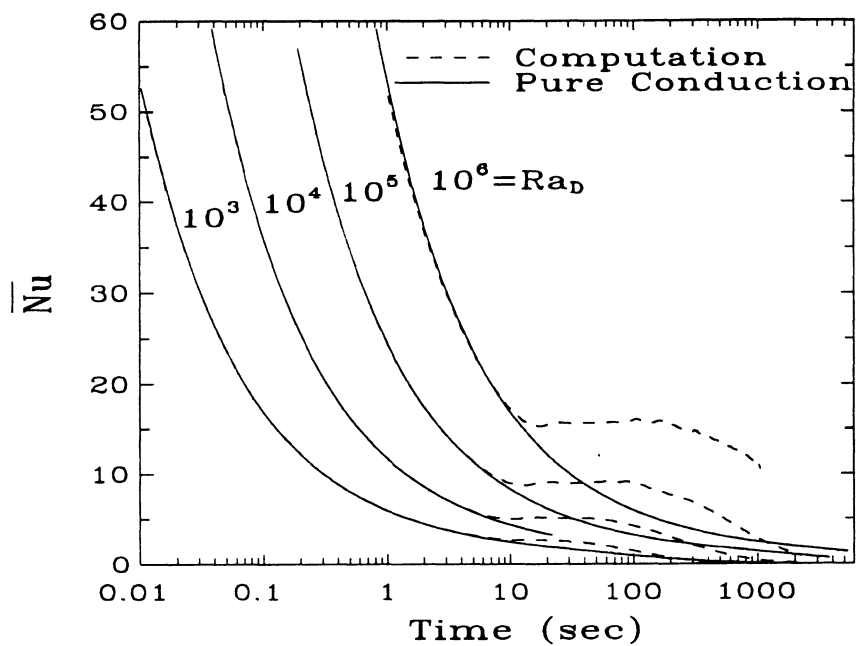


Figure 3.4: Transient heat transfer including pure conduction solutions for  $10^3 \leq Ra_D \leq 10^6$ .

The nearest analogy to compare the heat transfer during the quasi-steady regime is the long horizontal cylinder in an infinite medium. The Morgan (1975) review included experiments and analysis by several investigators. Unfortunately, Morgan reports a wide disparity in the reported values of the average Nusselt as a function of Rayleigh number for the horizontal cylinder in an infinite medium. Considering the cases compiled by Morgan with working fluids and Rayleigh number ranges similar to those considered here, a wide range of average Nusselt number results are reported. Table 3.2 shows the range of average Nusselt numbers along with a recommended average Nusselt number given by Morgan for each order of Rayleigh number.

$Ra_D$	$\overline{Nu}_{\min}$	$\overline{Nu}_{\max}$	$\overline{Nu}_{Morgan}$
$10^3$	2.64	3.50	3.11
$10^4$	4.70	5.87	4.80
$10^5$	8.12	10.22	8.54
$10^6$	14.45	18.17	15.20

Table 3.2: Range of average Nusselt numbers ( $\overline{Nu}_{\min}$ ,  $\overline{Nu}_{\max}$ ) from investigators compiled by Morgan and the recommended value by Morgan ( $\overline{Nu}_{Morgan}$ ).

Morgan attributed deviations in the reported results to differences in experimental designs and measurements. More recently, Churchill and Chu (1975) have studied heat transfer from the horizontal cylinder. Table 3.3 shows the computed average Nusselt numbers along with those of Morgan and Churchill and Chu.

$Ra_D$	$\overline{Nu}$	$\overline{Nu}_{Morgan}$	$\overline{Nu}_{C\&C}$
$10^3$	2.96	3.11	3.02
$10^4$	5.14	4.80	5.15
$10^5$	9.08	8.54	9.31
$10^6$	15.67	15.20	17.62

Table 3.3: Average Nusselt number results of current computations ( $\overline{Nu}$ ) compared with correlations from Morgan ( $\overline{Nu}_{Morgan}$ ) and Churchill and Chu ( $\overline{Nu}_{C\&C}$ ).

The present computations compare well with Churchill and Chu at Rayleigh numbers up to  $10^5$  and with Morgan at  $10^6$ . Considering the variation in the previously published results reported by Morgan, the current quasi-steady results compare well with either Churchill and Chu or with Morgan. Figure 3.5 illustrates the transient computations along with the infinite medium correlation of Morgan.

The limiting cases of pure conduction and infinite medium convection provide an independent basis for comparing the behavior and accuracy of the current results during the first two regimes. The behavior of the heat transfer and fluid flow during the decay period is rather complex as the bulk temperature in the enclosure begins to rise and fluid velocities diminish. There are no simple limiting cases to represent the heat transfer during the decay period.

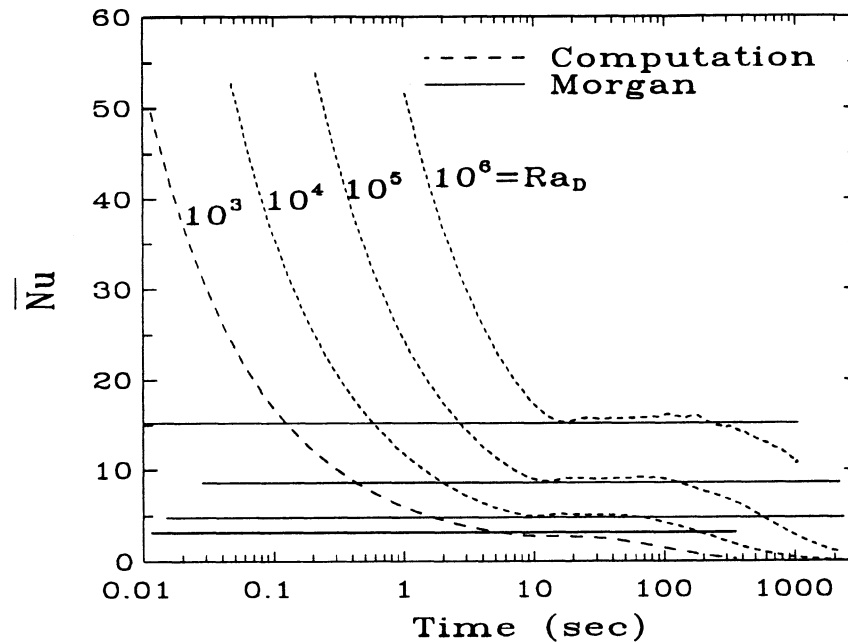


Figure 3.5: Transient heat transfer including the Morgan correlation for a long horizontal cylinder in an infinite medium for  $10^3 \leq Ra_D \leq 10^6$ .

### 3.2.2 Scale Analysis

The temporal behavior of the pure conduction and quasi-steady regimes are well characterized by the limiting cases shown in Figures 3.4-3.5. It would be useful to have the ability to predict the time duration of the conduction and quasi-steady regimes as well as determine the appropriate parameters to correlate the decay period. These objectives can be achieved by using scale analysis techniques. The scale analysis estimates derived here are analogous to the estimates found for the flat plate in the rectangular enclosure.

The following sequence of estimates are used to predict the time duration of the conduction dominated regime. Considering the dimensional form of the energy equation (Equation 3.4) in an order of magnitude sense

$$\frac{\Delta T}{\Delta t}, v_r \frac{\Delta T}{\delta_T}, v_z \frac{\Delta T}{D} \sim \frac{\alpha \Delta T}{r \delta_T}, \alpha \frac{\Delta T}{\delta_T^2}, \alpha \frac{\Delta T}{D^2} \quad (3.6)$$

where  $\Delta T = (T_w - T_o)$ ,  $\Delta t$  is the time duration,  $\delta_T$  is a characteristic thermal boundary layer thickness, and  $D$  is the heat exchanger tube diameter. Assuming that the velocity components are small during the early transient and the boundary layer thickness is much smaller than the tube diameter ( $\delta_T \ll D$ ), the remaining terms balance providing an estimate for the thermal boundary layer thickness identical to that of Patterson and Imberger (1980).

$$\delta_T \sim (\alpha \Delta t)^{1/2} \quad (3.7)$$

Considering the dimensional form of axial momentum (Equation 3.3), the buoyancy force  $g \beta \Delta T$  accelerates fluid within the boundary layer  $\delta_T$  and for a Prandtl number greater than unity, the viscous force term  $\nu v_z / \delta_T^2$  dominates the inertia force  $v_z / \Delta t$  term. The resulting balance between the buoyancy and viscous force terms yields an estimate of the vertical velocity component.

$$v_z \sim \frac{g \beta \Delta T}{Pr} \Delta t \quad (3.8)$$

An energy balance on the thermal boundary layer imposes a balance between the conducted energy from the heat exchanger and that convected away.

$$v_z \frac{\Delta T}{D} \sim \alpha \frac{\Delta T}{\delta_T^2} \quad (3.9)$$

The above expression can be simplified by Equations 3.7-3.8 which results in an estimate for the time duration of the conduction dominated regime.

$$\Delta t_c \sim \frac{D^2}{\alpha Ra_D^{1/2}} \quad (3.10)$$

Conduction limit time estimates from Equation 3.10 are shown in Figure 3.6. The scale estimates accurately predict the duration of the conduction dominated regime.

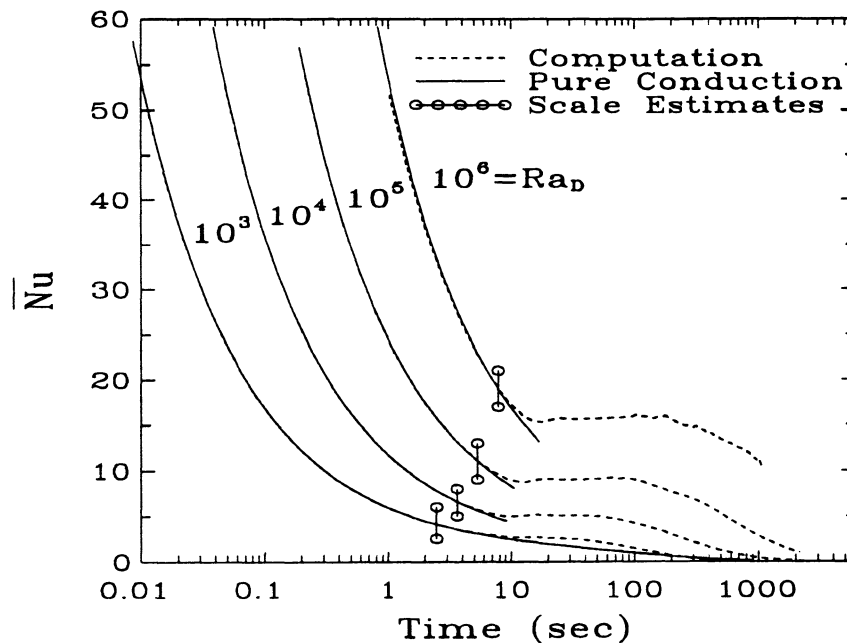


Figure 3.6: Scale estimates for the duration of the conduction dominated regime.

At the end of the conduction dominated regime, the vertical component of velocity  $v_z$  becomes

$$v_z \sim \frac{Ra_D^{1/2} \alpha}{D} \quad (3.11)$$

and the boundary layer thickness is  $\delta_T \sim D/Ra_D^{1/4}$ . Assuming that the volume flow of fluid through the boundary layer is constant during the quasi-steady period, the flow rate  $\dot{Q}$  is given by

$$\dot{Q} \sim v_z \delta_T \sim \alpha Ra_D^{1/4} \quad (3.12)$$

The time required for a fluid element to traverse the cylinder circumference from bottom to top is

$$t \sim \frac{L}{V} \sim \frac{\frac{\pi}{2} D}{v_z} \sim \frac{\pi D \delta_T}{2 \alpha Ra_D^{1/4}} \quad (3.13)$$

The end of the quasi-steady regime occurs when the temperature in the tank begins to rise significantly. A significant bulk temperature rise is observed when the volume of fluid equivalent to that above the heat exchanger is circulated through the coil thermal boundary layer. The time required to circulate the volume of fluid above the heat exchanger through the thermal boundary layer around the heated coil yields the quasi-steady period duration estimate.

$$\Delta t_{qs} \sim \frac{r_x^2 \gamma [1 - (\eta + \phi)]}{2 \alpha \phi^2 Ra_D^{1/4}} \quad (3.14)$$

where  $r_x = D/2$ ,  $\gamma = R_T/H_T$ ,  $\eta = H_x/H_T$ , and  $\phi = r_x/H_T$ . The quasi-steady time duration scale estimates are shown in Figure 3.7. The quasi-steady time duration estimates agree well with the apparent end of the quasi-steady period identified by position where the computed heat transfer diverges from the infinite medium solution.

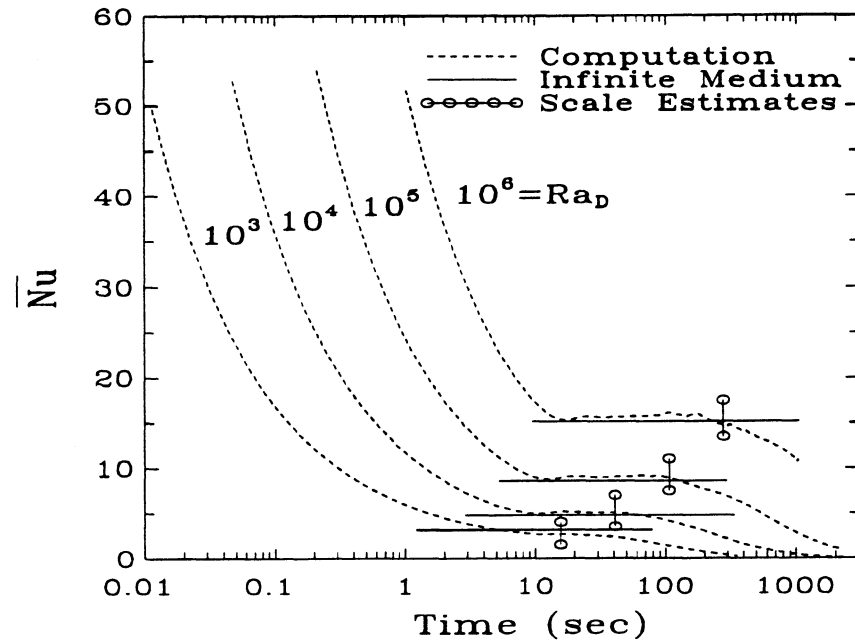


Figure 3.7: Scale estimates for the duration of the conduction dominated regime.

Finally, we use scale analysis techniques to identify parameters to correlate the decay period. An energy balance on the heat exchanger relates the conducted energy to the convected energy.

$$k \frac{(T_w - \overline{T})}{(\delta_T)} \sim \frac{\overline{Nu} k}{D} (T_w - T_o) \quad (3.15)$$

Since  $\delta_T$  is not constant as the decay period progresses, the expression for the characteristic thermal boundary thickness must be modified.

$$\delta_T \sim \frac{D}{Ra_D^{1/4}} \rightarrow \overline{\delta_T} \sim \frac{D}{\overline{Ra_D}^{1/4}} \quad (3.16)$$

where  $\overline{Ra_D}^{1/4}$  is based on the temperature difference ( $T_w - \overline{T}$ ) similar to that used by Hall, et al. (1988). Substituting the above expression in Equation 3.15 results in an estimate for the average Nusselt number from the coil.

$$\overline{Nu} \sim (1 - \overline{T}^*)^{5/4} Ra_D^{1/4} \quad (3.17)$$

with  $(1 - \overline{T}^*) \equiv (T_w - \overline{T})/(T_w - T_o)$  and  $\overline{T}^*$  is proportional to the fraction  $f$  of the cavity heated to temperature  $T_w$ . In general, Equation 3.17 is not a useful expression for correlating the Nusselt number since the bulk cavity temperature or heated fraction  $f$  are required. An expression for the heated fraction can found by considering an overall energy balance on the enclosure for the differentially heated fraction as

$$df \sim \frac{q dt}{mc(T_w - T_o)} \quad (3.18)$$

Integrating the above equation and applying the condition at  $t=0$  the heated fraction  $f=0$  results in an expression for the heated fraction which can be substituted into Equation 3.17 to yield

$$\overline{Nu} \sim 0.5686 \left[ 1 + \frac{\alpha \kappa \phi^2 Ra_D^{1/4} t}{\gamma^2 D^2} \right]^{-5} Ra_D^{1/4} \quad (3.19)$$

where  $\alpha$  is the thermal diffusivity,  $\kappa = R_x/H_T$ ,  $\phi = r_x/H_T$ ,  $\gamma = R_T/H_T$ , and  $Ra_D$  is defined based on the initial temperature difference. The coefficient 0.5686 is determined from a least squares fit of the computed decay period results for all orders of Rayleigh number. The correlation given by Equation 3.19 explains 99.86% of the variation in the average Nusselt

number over the decay period. The agreement between the correlated decay periods and the actual computed decay periods is demonstrated in Figure 3.8 for  $Ra_D=10^5$ . Plots for other orders of Rayleigh numbers are similar.

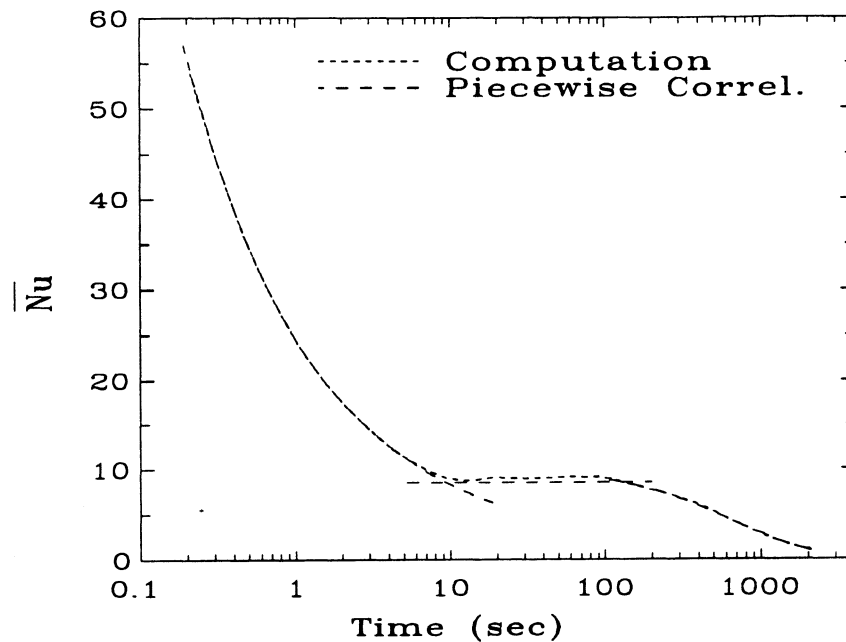


Figure 3.8: Computed heat transfer response and piecewise heat transfer response composed of pure conduction, infinite medium, and the correlated decay period for  $Ra_D=10^5$ .

For thermal storage, an important consideration is the time required to charge the tank (which is found from the transient bulk temperature response). Figure 3.9 shows the

typical response of the bulk temperature in the enclosure. It is clear that the majority of overall energy transfer into the tank occurs during the decay period as evidenced by the greatest bulk temperature rise.

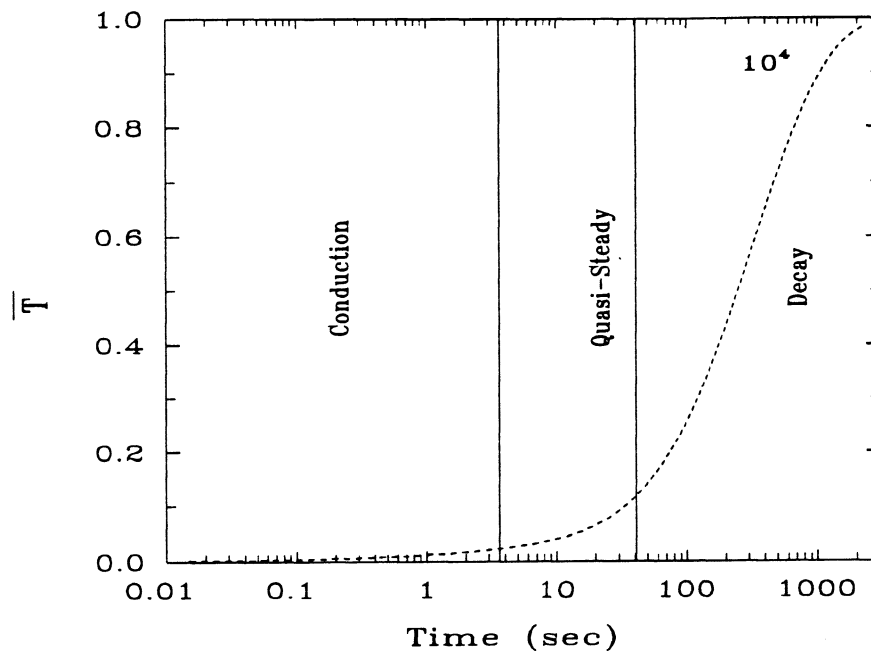


Figure 3.9: Transient bulk temperature response that occurs during the respective regimes for  $Ra_D=10^4$ .

### 3.2.3 Flow Field Results

The transient evolution of the temperature and fluid flow fields in the present geometry are very complex. Farrington and Bingham (1986) used dye injection techniques and noted the complex behavior of the flow fields from the various heat exchanger

configurations. In the case of a smooth coil heat exchanger, the authors noted unstable and swirling convection currents. Similar behavior is observed in the computations performed during this study. It is difficult to present comprehensive flow field results from a transient processes as complex as the one considered here. The temperature and velocity flow fields are presented for the case of  $Ra_D=10^5$  in order to illustrate and identify key features of the flow.

Figures 3.10a and 3.10b show temperature and stream function contours respectively at the time corresponding to the early quasi-steady period.

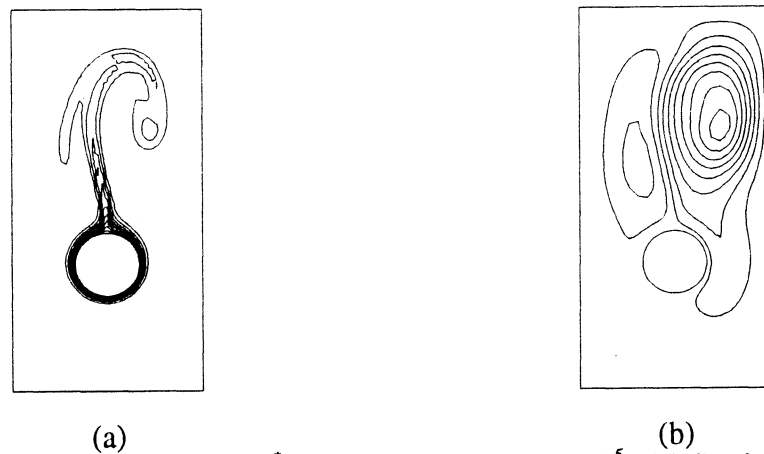


Figure 3.10: Contour maps at  $t^*=61$  ( $t=140$  sec),  $Ra_D=10^5$ : (a) Isotherms,  $T_{min}=0.1$ ,  $\Delta T=0.1$ ,  $T_{max}=1.0$  i.e.,  $0.1(0.1)1.0$ ; (b) Stream function,  $\psi_{min} = -3.391$ ,  $\Delta\psi = 0.452$ ,  $\psi_{max} = 0.673$  i.e.,  $-3.391(0.452)0.673$ .

By this time in the quasi-steady regime, the velocity flow field near the cylinder is fully developed and the thermal plume above the cylinder is reaching the top of the enclosure. Two vortices circulate in opposite directions on either side of the cylinder with a large component of flow proceeding down the center of the enclosure. Figure 3.11 shows the results at a later time in the quasi-steady period. At this time, clockwise rotating eddies

have formed above the cylinder and the core flow near the cylinder source in the center of the enclosure has reversed. The core of the enclosure above the cylinder is relatively warmer than fluid near the enclosure walls and significant stratification does not occur.

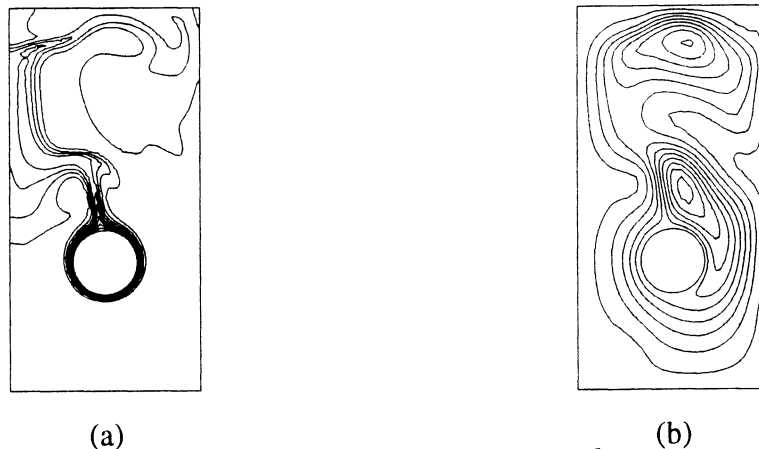


Figure 3.11: Contour maps at  $t^*=101$  ( $t=232$  sec),  $Ra_D=10^5$ : (a) Isotherms, 0.1(0.1)1.0; (b) Stream function, -1.88(0.20)-0.07735.

Figure 3.12 show the flow and temperature fields at a time corresponding to the end of the quasi-steady regime. The end of the quasi-steady period is caused by the weakly stratified temperature field moving warmer fluid down in a neighborhood near the cylinder source; reducing the temperature difference across the source. Core flow near the cylinder source has resumed its upward flow direction and several clockwise and counter-clockwise eddies have formed.

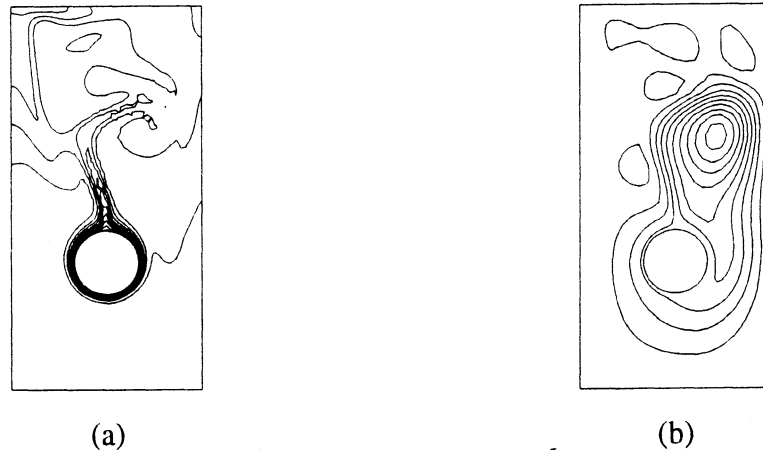


Figure 3.12: Contour maps at  $t^*=141$  ( $t=323$ ),  $Ra_D=10^5$ : (a) Isotherms, 0.1(0.1)1.0; (b) Stream function, -2.554(0.304)0.0955.

### 3.3 Conclusions

The temporal behavior of the flow field in the cylindrical enclosure is quite different than in the square cavity. The square cavity flow field was characterized by the existence of a single clockwise rotating vortex. The location of this vortex hub was a function of the Rayleigh number and time into the transient. In the cylindrical enclosure, the flow field is significantly more complex. The structure cannot be characterized by a single vortex rotating exclusively in one direction. During the transient, several vortices form and dissipate. There is a predominant bulk "core" flow that moves from top to bottom in the center of the enclosure for much of the transient; however, this core flow does reverse direction during the transient.

The isotherms in the square cavity configuration show that a strong degree of stratification is maintained throughout the entire transient. In the cylindrical enclosure, the stratification behavior is quite different. The stratification is quite weak due to mixing caused by eddies forming and dissipating combined with a reversing core flow.

Although the qualitative behavior of the temperature and flow fields in these two geometric configurations are quite different, the character of the transient heat transfer is similar. In each case, the heat transfer is characterized by three distinct regimes: conduction, quasi-steady, and decay. The conduction and quasi-steady regimes compare well with limiting cases. Scale analysis successfully predicts duration of the regimes as well as identifying appropriate parameters to correlate the decay period. The scale analysis techniques used in this geometric configuration are entirely analogous to those used in the square cavity with a heated vertical flat plate.

## References

- 
- Cabelli, A., "Storage Tanks - A Numerical Experiment", *Solar Energy*, **19**, pp. 45-54, (1977).
- Chan, A. M. C., Smereka, P. S., Giusti, D., "A Numerical Study of Transient Mixed Convection Flows in a Thermal Storage Tank", *Journal of Solar Energy Engineering*, **105**, pp. 246-253, (1983).
- Churchill, S. W., Chu, H. H. S., "Correlating Equations for Laminar and Turbulent Free Convection from a Horizontal Cylinder", *International Journal of Heat and Mass Transfer*, **18**, p. 1049, (1975).
- Farrington, R. B., "Test Results of Immersed Coil Heat Exchangers and Liquid Storage Tanks Used in the Packaged Systems Program", *SERI Rept. #TR-254-2841*, June (1986).
- Farrington, R. B., Bingham, C. E., "Testing and Analysis of Immersed Heat Exchangers", *SERI Rept. #TR-253-2866*, August (1986).
- Feiereisen, T. J., Klein, S. A., Duffie, J. A., Beckman, W. A., "Heat Transfer from Immersed Coils", presented at *ASME WAM Phoenix - 1982*, Paper No. 82-WA/SOL-18, Nov. (1983).
- FIDAP, A fluid dynamics analysis package by Fluid Dynamics International, Inc. 500 Davis St. Suite 600, Evanston, IL, 60201.
- Guo, K. L., "Numerical Study of Flow and Temperature Stratifications in a Liquid Thermal Storage Tank", *Journal of Solar Engineering*, **107**, pp. 15-20, (1985).
- Hall, J. D., Bejan, A., Chaddock, J. B., "Transient Natural Convection In a Rectangular Enclosure With One Heated Side Wall", *International Journal of Heat and Fluid Flow*, **9**(4), pp. 396-404, (1988).
- Lavan, Z., Thompson, J., "Experimental Study of Thermally Stratified Hot Water Storage Tanks", *Solar Energy*, **19**, pp. 519-524, (1977).
- Lightstone, M. F., Raithby, G. D., Hollands, K. G. T., "Numerical Simulation of the Charging of Liquid Storage Tanks: Comparison With Experiment", *Journal of Solar Energy Engineering*, pp. 225-231, (1989).

Morgan, V. T., "The Overall Convective Heat Transfer from Smooth Circular Cylinders", *Advances In Heat Transfer*, **11**, pp. 199-263 (1975).

Patterson, J., Imberger, J., "Unsteady Natural Convection In a Rectangular Cavity", *Journal of Fluid Mechanics*, **100**, pp. 65-86, (1980).

Radosevich, L. G., Wyman, C. E., "Thermal Energy Storage Development for Solar Electrical Power and Process Heat Applications", *ASME Journal of Solar Energy Engineering*, **105**, pp. 111-118, (1983).

Reindl, D. T., Beckman, W. A., Mitchell, J. W., Rutland, C. J., "Benchmarking Transient Natural Convection In An Enclosure", *1991 ASME National Heat Transfer Conference Minneapolis*, (July 1991).

Sliwinski, B. J., "Stratification In Thermal Storage During Charging", *International Conference on Heat Transfer, Toronto, Canada*, **4**, pp. 149-154, (1978).

Young, M. F., Baughn, J. W., "An Investigation of Thermal Stratification in Horizontal Storage Tanks", *Journal of Solar Energy Engineering*, **103**, pp. 286-290, (1981).

## 4 Experimental Analysis

Experimental techniques have been used for centuries as a means to understand the behavior of physical processes. Experiments provided the basis for relations such as Fourier's law of conduction and Newton's law of cooling. In addition, many of the correlations in convection heat transfer are based on empirical results. The advent of computers and numerical techniques have changed the role of experiments in research. With the proliferation of fast processors and parallel computing architectures, numerical analyses are increasingly replacing physical experiments as a research and development tool.

There are advantages and disadvantages in using numerical techniques in lieu of physical experiments. Among the benefits are cost, flexibility (in geometry and parameters), complete capture of flow field information ( $\bar{V}$  and  $T$ ) without intrusion, and derivation of integral quantities (e.g.,  $\overline{Nu}$  and  $\bar{T}$ ). The disadvantages include accuracy and applicability of assumptions applied in the numerical technique. Far too often, numerical computations of real processes are reported without any evidence of "accuracy". Little or no attempt is made to assure that the codes/methods being used are an accurate representation of the real process being simulated. Within the context of numerical computations, the validity of the results in Chapters 2 and 3 relied on convergence properties of the numerical method and comparing the results with independent limiting cases. Since the applicability of all assumptions can not be addressed in a numerical environment, experiments are needed.

The cylindrical enclosure with a single coil heat exchanger shown in Figure 4.1 will be focus of the experimental investigation. The range of parameters to be explored

experimentally will be restricted due to limited resources; however, the experimental apparatus is designed to operate in parameter ranges where the numerical solutions are "strained". Agreement between the experimental data and numerical results under these conditions suggests confidence in the numerical solutions for other parameter ranges. The goal of the experiments is to validate the numerical computations by "measuring" two key variables: average Nusselt number from the heat exchanger and the enclosure bulk fluid temperature.

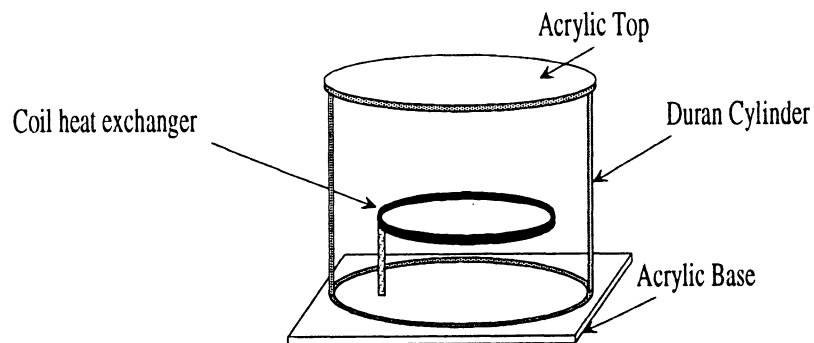


Figure 4.1: Experimental enclosure layout.

#### **4.1 Determining Average Nusselt Number and Bulk Temperature**

Two variables have been selected to compare the "accuracy" of the numerical computations with the actual performance of a physical experiment. Since the quantities are not directly measurable, they must be derived by observing other variables. This section discusses the methodologies involved with determining the average Nusselt number and bulk temperature in the experimental configuration.

The average Nusselt number can be determined by three different methods. The first two methods involves measuring the electrical power supplied to a resistance heating element housed in the heat exchanger. Consider the following energy balance on the tank and heat exchanger.

$$\text{Tank} \quad q_{pwr} - q_L = \frac{dU}{dt} \quad (4.1)$$

$$\text{Exchanger} \quad q_{pwr} - q_{convect} = 0 \quad (4.2)$$

where  $q_{pwr}$  is the electrical power supplied to the heat exchanger,  $q_L$  is the heat loss to the surroundings,  $U$  is the internal energy of fluid in the tank,  $q_{convect}$  is the energy convected from the heat exchanger. (Note, the heat exchanger energy balance neglects the initial transient required to "step" the heat exchanger to its specified temperature.) The numerical computations imposed an adiabatic boundary condition on all walls of the enclosure. The above energy balances can be used to "correct" the experimental results with heat losses so that direct comparisons with the adiabatic enclosure assumed in the computations are possible. The corrected energy balance yields a relationship for the average heat transfer coefficient as given by

$$\bar{h}_x A (T_w - T_o) = I(t)^2 R + \bar{h}_L A_o (\bar{T} - T_o) \quad (4.3)$$

where  $\bar{h}_x$  is the average heat transfer coefficient from the heat exchanger,  $A$  is the external area of the heat exchanger,  $\bar{h}_L$  is the average heat loss coefficient from the insulated enclosure, and  $A_o$  is the external area of the insulated enclosure. Rearranging Equation 4.3 results in the expression for the average Nusselt number for the heat exchanger as a function of other measured variables.

$$\overline{Nu}(t) = \frac{I(t)^2 R}{2\pi^2 k_w R_x (T_w - T_o)} + \frac{\bar{h}_L A_o (\bar{T}(t) - T_o)}{2\pi^2 k_w R_x (T_w - T_o)} \quad (4.4)$$

The variables which are continuous functions of time are the current supplied to the heating element and the fluid bulk temperature. The resistance  $R$  of the heating element is assumed constant due to its stability over the temperature range considered. The measured current represents an root mean squared (RMS) value of the chopped alternating current (AC) power supplied to the heating element from the phase angle fired relay.

A second method for computing the average Nusselt number is based on calculating the power to the heat exchanger by the product of current through and voltage across the heating element.

$$\overline{Nu}(t) = \frac{I(t)V(t)}{2\pi^2 k_w R_x (T_w - T_o)} + \frac{\bar{h}_L A_o (\bar{T}(t) - T_o)}{2\pi^2 k_w R_x (T_w - T_o)} \quad (4.5)$$

The disadvantage with this method is the requirement to monitor an additional time dependent quantity, voltage  $V(t)$ .

The last method for computing the average Nusselt number relies on measuring the bulk temperature rather than the power supplied to the heat exchanger. The expression for the average Nusselt as a function of the bulk temperature is given by

$$\overline{Nu}(t) = \frac{(mc)_{tank}}{2\pi^2 k_w R_x (T_w - T_o)} \frac{d\bar{T}}{dt} + \frac{\bar{h}_L A_o (\bar{T}(t) - T_o)}{2\pi^2 k_w R_x (T_w - T_o)} \quad (4.6)$$

Equations 4.4-4.6 represent the data reduction equations for the average Nusselt number. The accuracy of each data reduction equation will be explored by detailed uncertainty analysis in Section 4.3.

A unique method to "measure" the bulk temperature of fluid in the enclosure has been established. By definition, the bulk temperature is the average temperature of fluid in the enclosure.

$$\bar{T} \equiv \frac{\int T(r, \theta, z) dV}{\int dV} \quad (4.7)$$

Past experimental methods employed to determine bulk temperature have relied on placing temperature transducers (typically thermocouples) at various spatial points throughout the enclosure and averaging the resulting readings. It is clear that bulk temperature results based on this methodology would be difficult to reproduce and prone to a high degree of inaccuracy in stratified enclosures. In the present investigation, an isobaric condition is imposed by allowing the working fluid to expand upon heating. By allowing the fluid to expand into a vertical column, the change in specific volume can be determined by measuring the differential change in total fluid volume. The temperature corresponding to this changed volume represents the bulk temperature of fluid in the enclosure.

The viability of the bulk temperature measurement method requires some limitations/assumptions to be investigated. First, the method requires the working fluid to retain a linear relationship between the temperature and specific volume. Without this linearity, the bulk temperature for strongly stratified and semi-stratified enclosures cannot be accurately derived from the volume expansion of the heated working fluid. Figure 4.2 illustrates the temperature-specific volume behavior for water (data from Keenan, et al. 1978). In the range of temperatures being considered in the experiments (~20-40C), the temperature-specific volume relationship is reasonably linear. A least squares linear fit to the property data explains 98.8% of the actual variation.

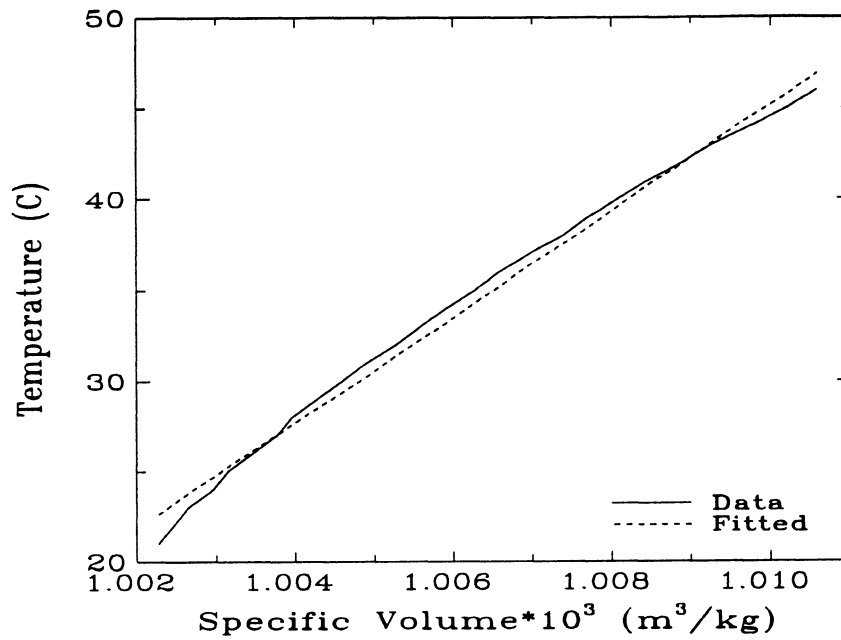


Figure 4.2: Temperature-specific volume behavior for water.

Another assumption in the method for experimentally determining the fluid bulk temperature concerns the heat and mass transfer of the working fluid in the expansion column. Heat loss in the column could potentially result in contraction of fluid and result in an erroneous bulk temperature measurement. Since the maximum volume of the fluid in the expansion column is only 1.5% of the total volume of fluid in the enclosure, the effect of heat loss and fluid contraction outside the enclosure is negligible. Mass transfer

of fluid from the expansion column to the ambient environment must also be minimized. Since the area of the free surface of fluid expanding in the column is very small ( $\sim 1.8 \text{ cm}^2$ ), mass transfer to the ambient is assumed negligible.

A potentially significant factor which may influence the observed bulk temperature is thermal expansion of the enclosure. Because of the relatively large volume of the enclosure compared to the expansion column, any changes in enclosure volume by thermal expansion will cause the true bulk temperature to be underpredicted. Further details related to assessing the accuracy of the bulk temperature measurements are given in Sections 4.2.3 and 4.3.

## 4.2 Experiment Configuration

The computations presented in Chapter 3 considered the cylindrical enclosure with the following geometric configuration:  $\phi = 0.167$ ,  $\gamma = 0.5$ ,  $\kappa = 0.5$ , and  $\eta = 0.333$ . The relative tube size  $\phi = 0.167$  was chosen for the numerical computations due to limitations on computational resources. Performing computations over the entire range of Rayleigh numbers with a smaller relative tube size would have required a significant computational resource increase. Unfortunately, constructing an experimental apparatus that matches the above parameters is not realistic; therefore, the following parameters will be used in the experiments:  $\phi = 0.03068$ ,  $\gamma = 0.5$ ,  $\kappa = 0.3834$ , and  $\eta = \textit{free}$ . The experimental results will be compared with a numerical computation performed using these parameters.

### 4.2.1 Design

In any experimental analysis, there are trade-offs associated with the physical design of the apparatus. The goal is to design and construct an apparatus that resembles, as close

as possible, the geometric configuration and boundary conditions used in the computations. A significant attempt was made to make the apparatus as simple as **practical**. The experimental tank is shown in Figure 4.3.

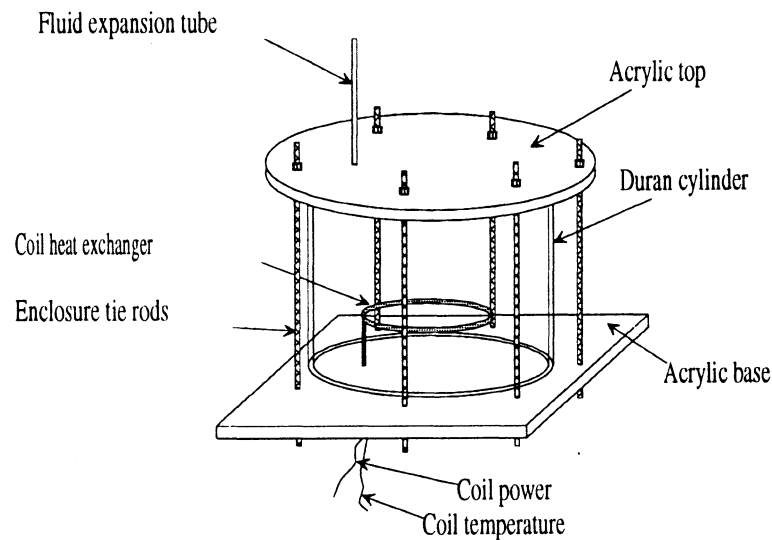


Figure 4.3a: Experimental enclosure (isometric view).

The requirements of the enclosure include: low thermal conductivity, capable of being insulated easily, compatibility with working fluid (water), low thermal expansion, and transparent. An enclosure with low thermal conductivity will reduce heat loss and minimize any de-stratification of the interior fluid by conduction down the side walls of the enclosure. The enclosure must be well insulated so that the experimental boundaries approach the adiabatic conditions imposed in the numerical computations. The accuracy of the bulk temperature measurement technique relies on determining the volume expansion of the fluid only; therefore, the enclosure must have a very low thermal expansion coefficient to avoid confounding the fluid volume expansion with the enclosure volume expansion. A transparent enclosure will allow the use of flow visualization techniques.

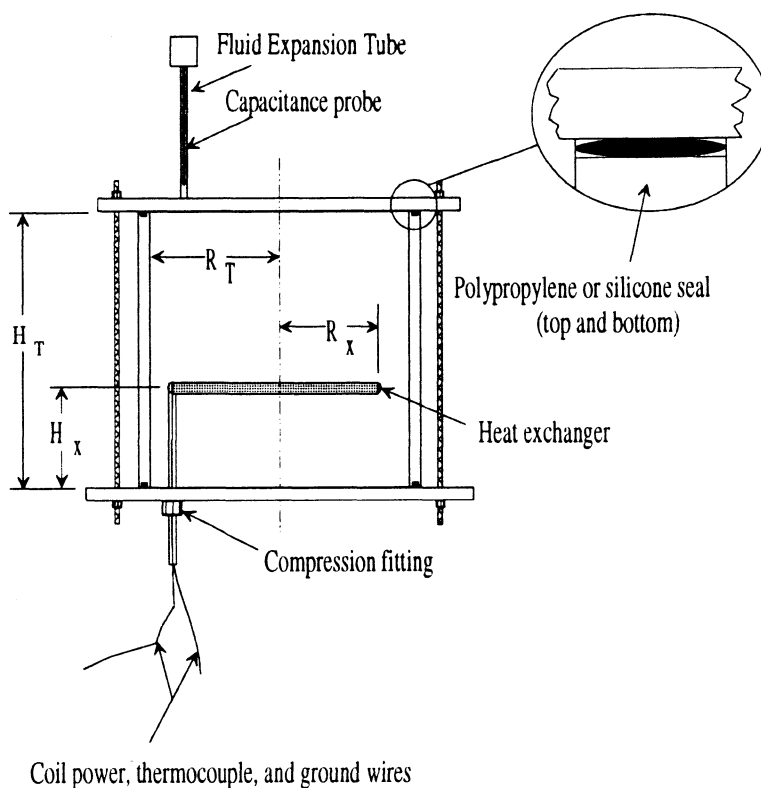


Figure 4.3b: Experimental enclosure (cross-section).

Two different materials, Acrylic and Duran<sup>®</sup>, were used in the main enclosure body (cylindrical portion of enclosure) to achieve these requirements. The acrylic is a polymer and the Duran<sup>®</sup> is a borosilicate based glass. Table 4.1 lists the relevant properties of the materials used in the enclosure construction.

Material	Property	Value	Units
Acrylic	Thermal conductivity	1.25	W/m-C
	Specific heat	1.19	kJ/kg-C
	Density	2,676	kg/m <sup>3</sup>
	Max. cont. temp.	82	C
	Linear expansion coeff.	7.56E-6	1/K
Duran <sup>®</sup>	Thermal conductivity	1.14	W/m-C
	Specific heat	0.711	KJ/kg-C
	Density	2,230	kg/m <sup>3</sup>
	Max. cont. temp.	500	C
	Linear expansion coeff.	3.25E-6	1/K

Table 4.1: Enclosure properties (at 33 C).

The enclosure consists of either an acrylic or Duran<sup>®</sup> cylinder sandwiched between an acrylic sheet base and top. A water-tight seal is made by a silicone seal placed at the top and bottom of the cylinder. The coil heat exchanger is supported in the enclosure by a polycarbonate tube which penetrates the enclosure base through a compression fitting. The tube serves as a physical support for the heat exchanger as well as being a conduit for routing the coil power, ground, and thermocouple cables out of the enclosure. A "vent" tube positioned on the top of the enclosure serves as a standpipe which allows the heated fluid in the enclosure to expand.

The performance requirements of the circular coil heat exchanger are among the most demanding of any component/subsystem in this experiment. The heat exchanger must have high thermal conductivity, low thermal capacitance, a smooth surface finish, compatible with the working fluid (water), and house thermocouple and heating elements. High thermal conductivity along with a low capacitance will yield a heat exchanger that

approaches the step change in wall temperature and isothermal surface conditions assumed in the numerical computations. A smooth surface finish will eliminate any wall induced disturbances in the buoyant flow field. The construction of the heat exchanger is illustrated in Figure 4.4.

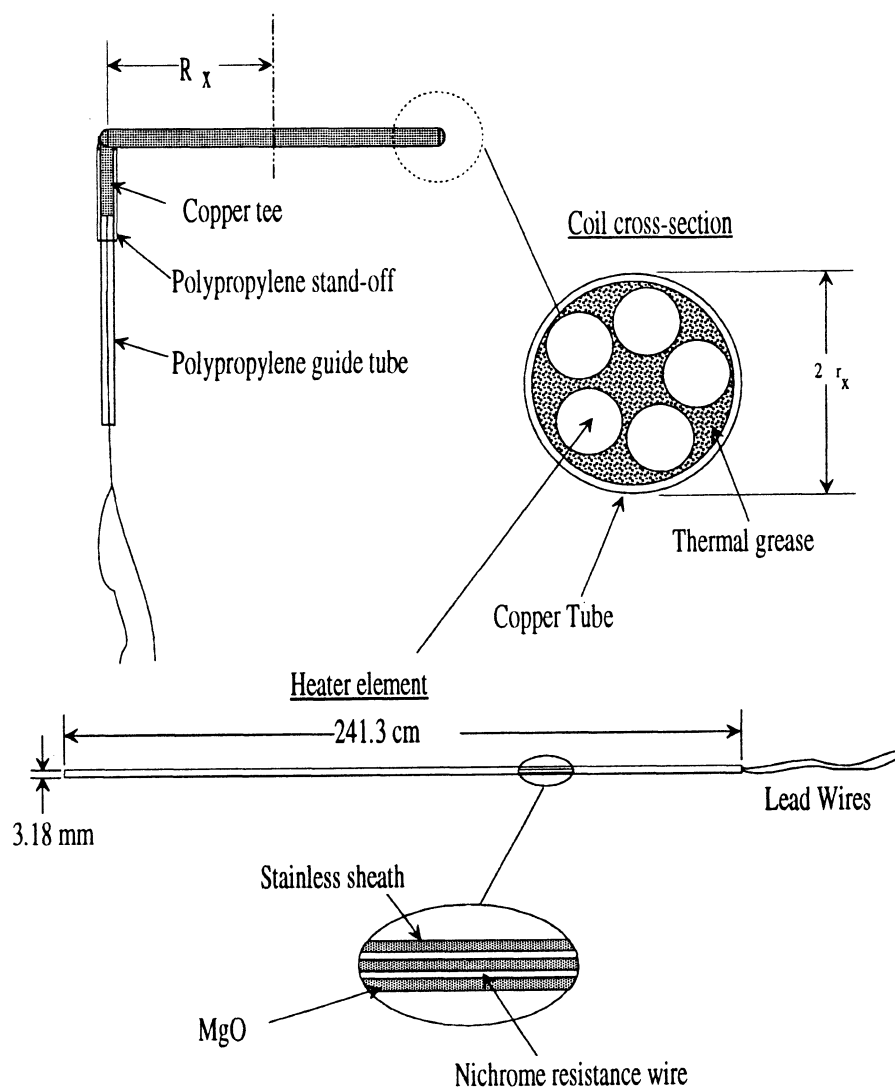


Figure 4.4: Circular heat exchanger design.

The main body of the heat exchanger consists of a 12.7 mm o.d. (0.5 in) copper tube formed in a circular shape. A single resistive heating element<sup>3</sup> is routed around the interior of the copper tube approximately six times as well as two T-type thermocouple probes and a ground wire. To enhance the heat transfer characteristics from the internal resistance element to the copper tube wall, thermal grease<sup>4</sup> is "pumped" into the coil. The grease enhances the thermal communication between the heating element and the coil by purging the air void fraction in the coil interior. The exterior surface of the copper tube is polished and coated with a very thin layer of clear protective acrylic sealant to minimize surface oxidation. The copper coil is "sealed" by sweating a custom formed tee section to the open ends of the tube. The thermocouple and power wires are routed down through this perpendicular tee. Parasitic conduction losses through the coil support are minimized by using a polycarbonate stand-off couple with an polycarbonate guide tube.

#### **4.2.2 Data Acquisition and Control Systems**

The data sought in the experiments include temporal values of ambient temperature, coil temperature, coil power, and fluid bulk temperature. All data is logged to a personal computer (IBM AT) via an analog-digital (A/D) converter board<sup>5</sup>. The A/D board used has sixteen channel capability with sixteen bit conversion resolution. A schematic of the data acquisition layout is shown in Figure 4.5

---

3 Model 125CH93A1X with stainless steel overbraid from Watlow; St. Louis, MO.

4 Omegatherm model 201 Thermal grease from Omega Engineering, Inc.; Stamford, CT.

5 Model WB-AAI High Resolution interface card from Omega Engineering, Inc.; Stamford, CT.

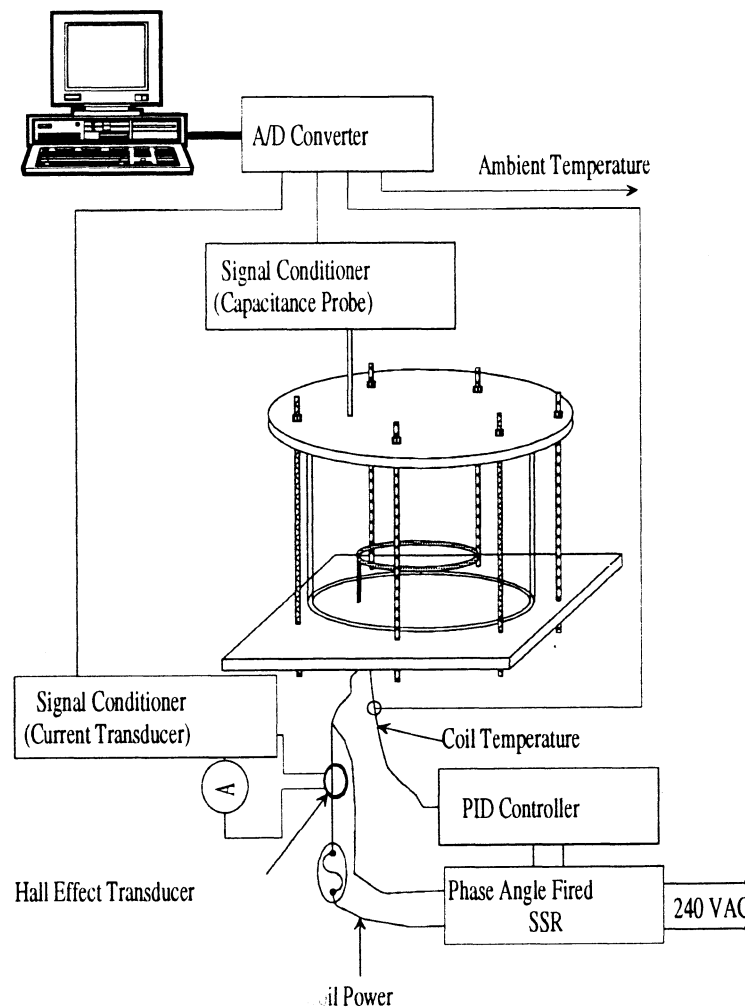


Figure 4.5: Data acquisition system.

Thermocouples are used to monitor the ambient and coil temperatures. The thermocouples are 36 AWG (0.005in, 0.127mm conductor diameter) copper/constantan (type T) construction with Teflon insulation<sup>6</sup>. The type T thermocouple was selected because it provides acceptable error characteristics (0.5 C, 0.9 F) for temperature

<sup>6</sup> Model TT-T-36 T-type thermocouple from Omega Engineering, Inc.; Stamford, CT.

measurement in the range under consideration. The small gage wire results in a very fast response to changes in the local temperature. All thermocouples are baseline calibrated in an ice bath. The thermocouple calibration is verified at higher temperatures by comparing measurements with a independently calibrated mercury bulb thermometer.

The power control system will modulate the electrical energy supplied to the heat exchanger such that a constant coil temperature is maintained. The coil power is determined by measuring the current supplied to the coil. Since the load (the heating element) is purely resistive, the power can be determined directly by applying ohms law. The resistance of the Nichrome heating element is insensitive to temperature (over the relevant range of temperatures considered); therefore, the power supplied to the coil is

$$P(t) = I(t)^2 R \quad (4.8)$$

where  $P$  is the power,  $I$  is root mean square current, and  $R$  is the coil resistance. The coil current is measured by using a hall effect transducer<sup>7</sup> along with a signal conditioner<sup>8</sup>. The signal conditioner reportedly provides a 0-10Vdc output proportional to the RMS value of the coil current. The advantages of this configuration include elimination of insertion losses (by the hall effect transducer), fast response ( $< 50 \mu\text{s}$ ), and ability to handle the chopped waveforms from the phase angle fired relay. The disadvantage with the hall effect transducer is the null drift.

Determining the enclosure bulk temperature relies on determining the fluid specific volume by measuring the change in height of fluid expanding in a column from the enclosure. A difficulty in applying this method arises when we consider techniques to

---

7 Model CTL-50 from Dalec Distributors; Chicago, IL.

8 Model CTA213 from Dalec Distributors; Chicago, IL.

monitor the continuous fluid height in the expansion column as a function of time. To be consistent with using the personal computer as a central data acquisition device, it is necessary to employ a transducer which monitors the continuous fluid level height and has an output compatible with the analog/digital converter. Several techniques were investigated on the basis of accuracy, cost, and complexity. The method selected utilizes radio frequency technology. The unit consists of a "capacitance" probe<sup>9</sup> (level transmitter) inserted into the expansion column coupled with an appropriate signal amplifier<sup>10</sup>. The probe represents one plate of a capacitor with the fluid as the other plate. The capacitance sensed by the probe varies as a linear function of fluid level. As fluid expands into the column, the capacitance increases providing a measurement system with an analog output signal directly proportional to the height of fluid in the expansion column.

The capacitance probe unit is calibrated by adding a fixed incremental volumes of fluid in the column and monitoring the response. (The addition of a fixed incremental volume of fluid to the column is controlled by using a 10 ml syringe.) The initial attempts at calibrating the transducer yielded a response from the probe as shown in Figure 4.6. Since the transducer output is quoted to be linear by the manufacturer, the behavior exhibited in Figure 4.6 is disturbing. The nonlinear output shown in Figure 4.6 is caused by a faulty transducer ground. The radio frequency technique requires a good ground in the same plane as the probe. A ground plane parallel to the capacitance probe is added to the expansion column and the resulting probe response over five separate runs is shown

---

9 Model 700-1-22 sensor from Drexelbrook Engineering; Horsham, PA.

10 Model 408-2200 two-wire transmitter from Drexelbrook Engineering; Horsham, PA.

in Figure 4.7. The results shown in Figure 4.7 indicate that the capacitance probe response is extremely linear and repeatable. The solid line is a least squares fit of all data and explains 99.996% of the variation in the probe response.

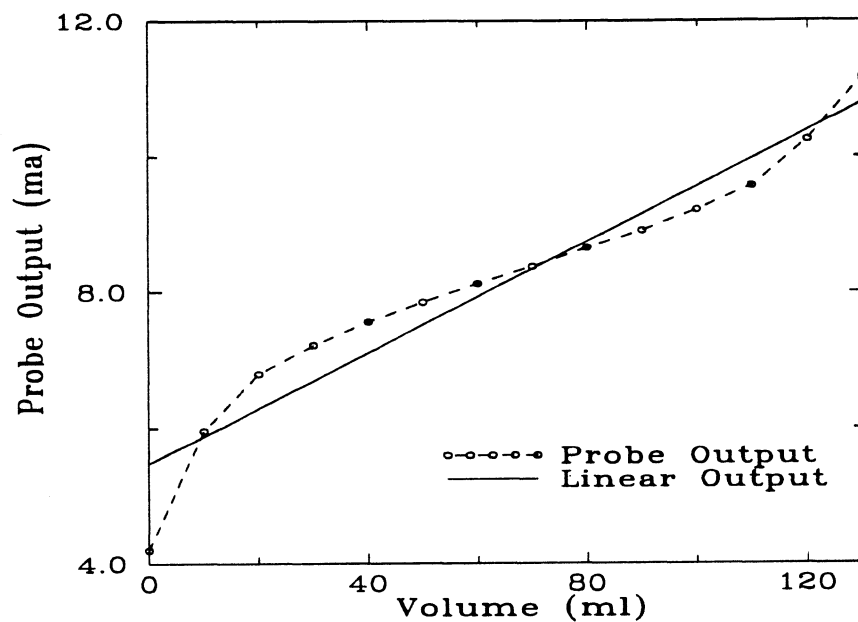


Figure 4.6: Capacitance probe with improper response.

To maintain the heat exchanger coil at a constant temperature, it is necessary to vary the amount of energy supplied to the coil. Initially, a simple feedback control system was engaged to accomplish this task. The feedback control system initially consisted of a PID

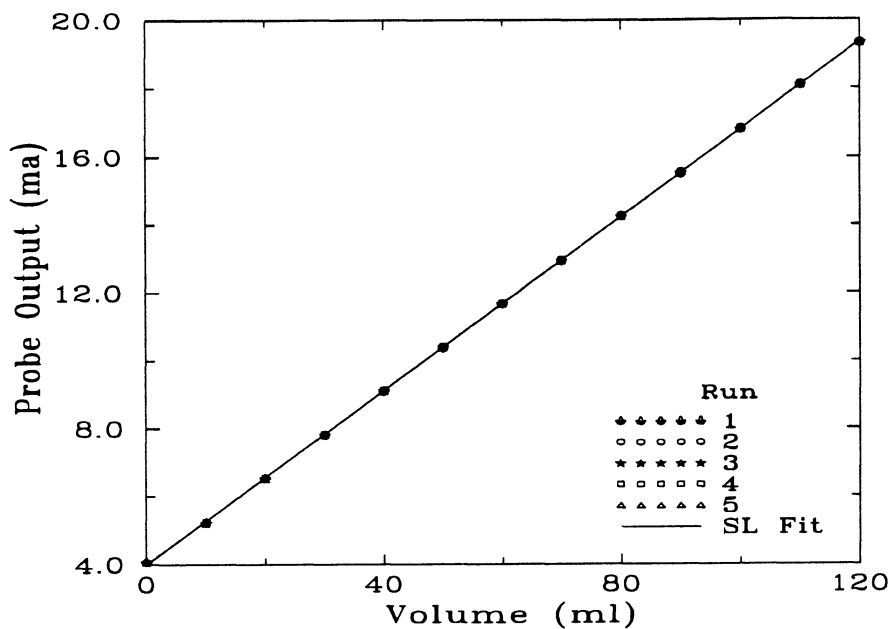


Figure 4.7: Acceptable capacitance probe response.

(proportional-integral-differential) controller<sup>11</sup>, coil temperature thermocouple, zero-cross fired SSR<sup>12</sup> (solid state relay), and a 240 VAC supply. The power supply in conjunction with the control system provides a time-proportioning output of power supplied to the heating element. A typical response of current as a function of time under this control scheme is shown in Figure 4.8.

<sup>11</sup> Model CN4401TR-D Micro-controller from Omega Engineering, Inc.; Stamford, CT.

<sup>12</sup> Model SSR240AC25: Solid state relay Omega Engineering, Inc.; Stamford, CT.

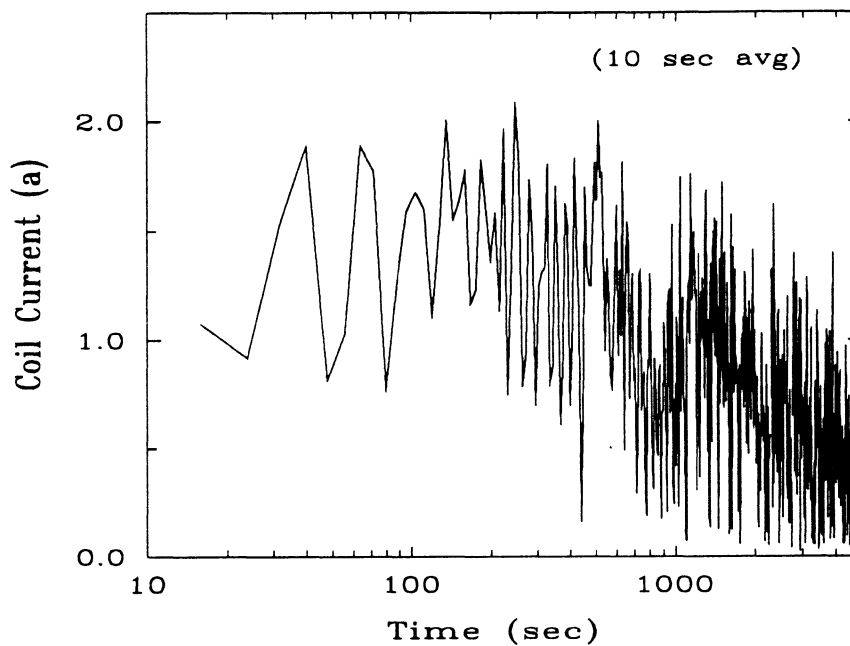


Figure 4.8: Response from time-proportional control strategy.

The simple time-proportioning control strategy proved to be too crude to allow accurate determination of the time dependent average Nusselt number (which is a function of the measured current). Various techniques were employed in an attempt to "clean-up" the signal from the current transducer including: Fourier transform filtering, time averaging, and control parameter modulation. None of these techniques were able to satisfactorily resolve the power signal; therefore, a more sophisticated control scheme was sought.

The second control strategy implemented uses a PID controller<sup>13</sup> with an analog proportioning output which is coupled with a phase angle fired solid state relay<sup>14</sup> (SSR). The SSR then modulates the power supplied to the coil depending on the magnitude of the temperature controller's output signal resulting in a much cleaner coil current signal as shown in Figure 4.9. The control signal begins to deteriorate at small magnitudes of current (when the enclosure bulk temperature has significantly increased) as indicated by the fluctuating current signal. The fluctuating signal can be smoothed by time-averaging the signal during the late transient.

---

13 Model 965A-1FA0-0000 Temperature Controller from Watlow Controls; Winona, Minnesota.

14 Model VO1-240-10-AT Solid state relay power controller from Watlow Controls; Winona, Minnesota.

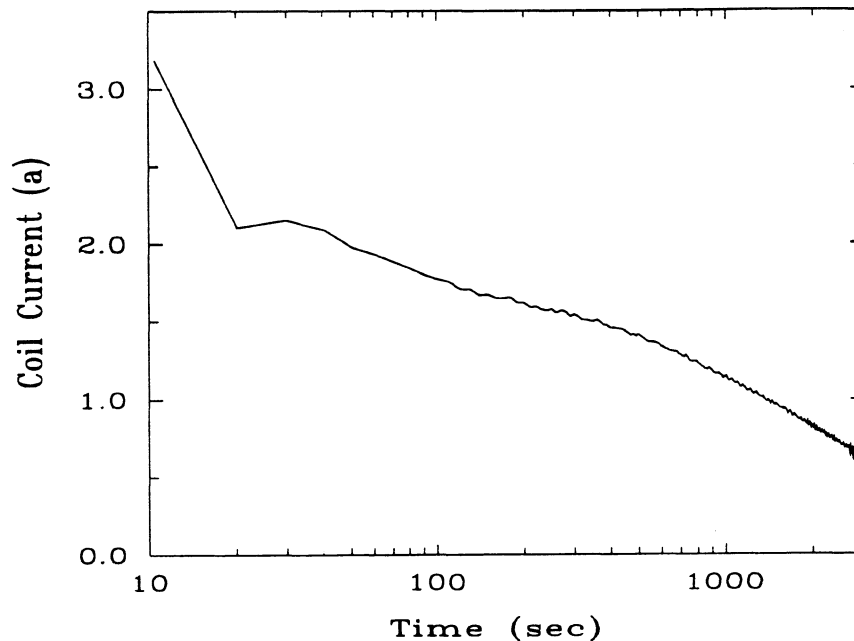


Figure 4.9: Typical response from analog-proportional control strategy.

### 4.2.3 Assumptions

There were several assumptions made in the course of the numerical computations and some of these assumptions need to be re-evaluated in the context of a physical experiment. One key assumption that needs to be examined is the Boussinesq approximation. The temperature change ( $T_w - T_o$ ) required to achieve the desired order of Rayleigh numbers is  $\sim 20$  C (36 F). A temperature difference this large well out of the range of the strict Boussinesq approximation ( $\sim 2$  C, 3.6 F) implying that the property variation as a function of temperature may be significant. The two properties that show

the largest temperature dependence are viscosity (both dynamic  $\nu$  and kinematic  $\mu$  viscosities) and the volume expansion coefficient  $\beta$ . As the temperature increases, viscosity decreases while the volume expansion coefficient increases. The net effect of these two properties changing with temperature is compounded when we consider the definition of the Rayleigh number ( $Ra_D = g \beta D^3 \Delta T / \nu \alpha$ ). Figure 4.10 shows the change in the property group ( $g \beta / \nu \alpha$ ) with temperature. The property variations with temperature effectively causes the driving force (Rayleigh number) to vary with temperature. Figure 4.11 shows the variation of Rayleigh number due to temperature effects on the fluid properties.

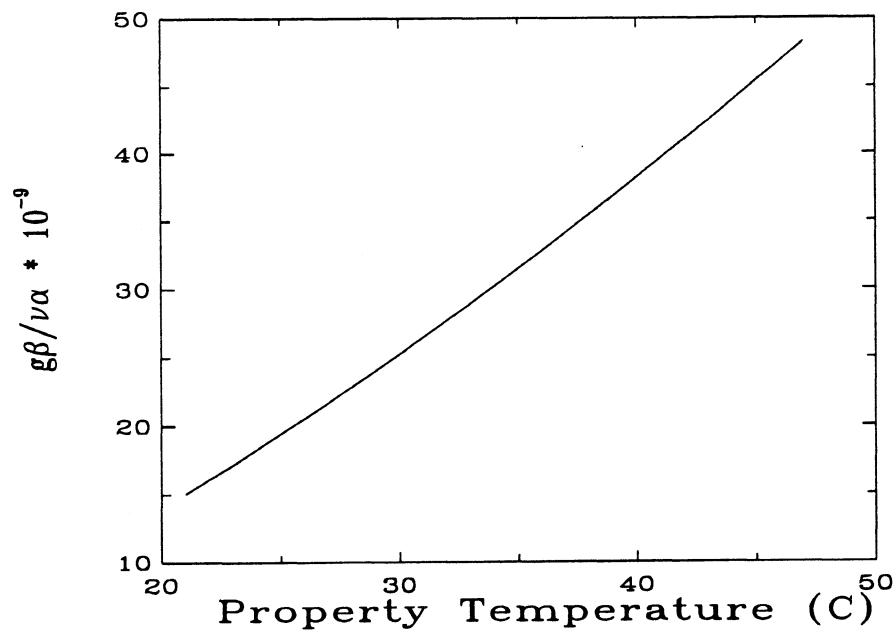


Figure 4.10: Temperature effect on combined fluid properties.

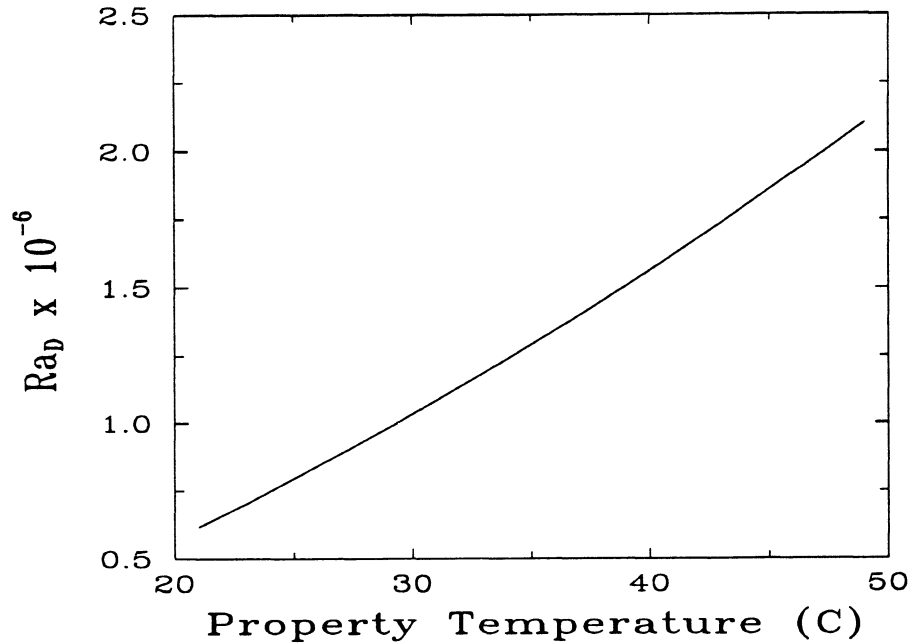


Figure 4.11: Temperature dependent fluid properties effects on  $Ra_D$  ( $D=12.7\text{mm}$ ,  $0.5\text{in}$ ;  $\Delta T = 20\text{C}$ ,  $36\text{F}$ ).

It may be possible to compensate for the property variations by selecting a suitable temperature for evaluating fluid properties. To study the influence of property variation, computations are performed using the square cavity geometry as discussed in Chapter 2 (since it is less intensive from a computational standpoint). The use of this geometry should not be considered a loss of generality in studying property variation effects since property variations are independent of geometry. A set of five computations are performed for a fixed geometry ( $H=W=2L$ ,  $y_p=H/2$ ). The computations are performed in dimensional

form with the properties evaluated and maintained constant based on three different temperatures. The constant property cases are compared with two variable property computations. The first allowed only the dynamic viscosity to vary as a polynomial function of temperature. The second allowed both the dynamic viscosity and thermal expansion coefficient to vary as a polynomial function of temperature. The sequence of computations are summarized below and the average Nusselt number results for the cases are shown in Figure 4.12.

Case 1:	Constant properties evaluated at $T_o=20$ C (68 F).
Case 2:	Constant properties evaluated at $T_{mean}=(T_o+T_w)/2=30$ C (86 F).
Case 3:	Constant properties evaluated at $T_w=T=40$ C (104 F).
Case 4:	Variable dynamic viscosity ( $\nu = f(T)$ ) and all other properties constant and evaluated at $T_{mean}=(T_o+T_w)/2=30$ C (86 F).
Case 5:	Variable dynamic viscosity ( $\nu = f(T)$ ), variable volume expansion coefficient ( $\beta = f(T)$ ) and all other properties constant and evaluated at $T_{mean}=(T_o+T_w)/2=30$ C (86 F).

It is clear that if properties are evaluated at the mean temperature the average Nusselt number results approach the variable property results. Table 4.2 shows time, magnitude, and location of peak velocity components for each of the five cases. The peak velocity results support the assumption that property variations can be accounted for by using fixed properties evaluated at a suitable temperature. Thus, the experimental results ("non-Boussinesq") with properties evaluated at the mean temperature ( $T_{mean}=\{T_o+T_w\}/2$ ) should compare well with the computational results ("Boussinesq").

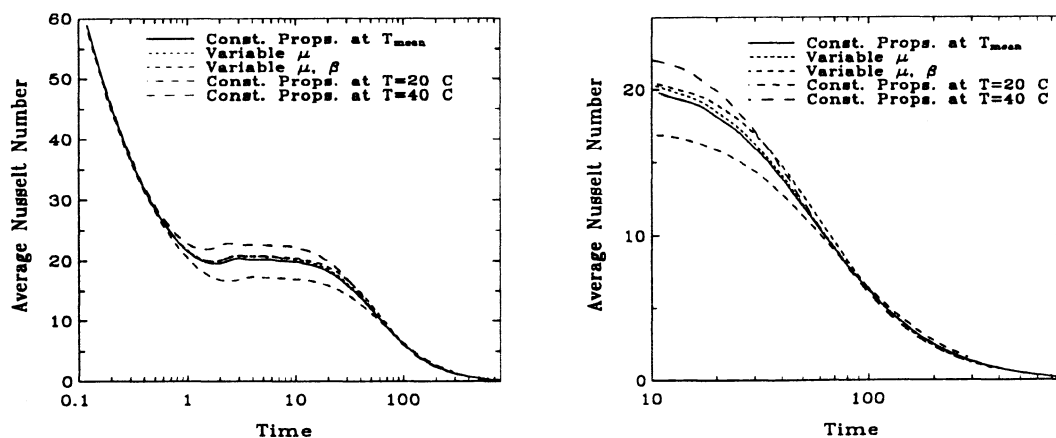


Figure 4.12: Effect of property variations on the average Nusselt number.

Case	$u_{max}$	$t$	$x$	$y$	$v_{max}$	$t$	$x$	$y$
1	6.130	3.74	2.479	24.11	9.381	3.43	0.0	21.60
2	9.132	2.88	2.187	24.25	13.063	2.59	0.0	21.92
3	12.01	2.40	2.187	24.40	16.169	2.12	0.0	22.20
4	8.721	2.87	2.187	24.25	12.987	2.58	0.0	21.92
5	8.514	2.82	2.187	24.25	13.089	2.54	0.0	21.92

Table 4.2: Peak velocity results; velocities in mm/sec and x-y in mm.

The numerical computations neglect all radiative heat transfer from the heat source to the fluid medium or enclosure. It is necessary to examine the effects of radiative transfer in the actual experimental apparatus. In this case, the working fluid represents a participating medium and the intensity of radiation leaving the source will diminish due

to both absorption and scattering. Considering a medium of thickness  $S$ , the monochromatic directional intensity varies according to Bouguer's law (as discussed by Siegel and Howell, 1981).

$$i_{\lambda}(S) = i_{\lambda}(0) \exp \left[ - \int_0^S K_{\lambda}(S) dS \right] \quad (4.9)$$

where  $i_{\lambda}$  is a directional monochromatic intensity,  $K_{\lambda}$  is a monochromatic extinction coefficient and  $S$  is the path length through the medium. The extinction coefficient consists of two components

$$K_{\lambda} = a_{\lambda} + \sigma_{s\lambda} \quad (4.10)$$

where  $a_{\lambda}$  is an absorption coefficient and  $\sigma_{s\lambda}$  is a scattering coefficient. Assuming that the scattering component is negligible ( $\sigma_{s\lambda} \approx 0$ ) and the absorption coefficient is not a function of position, Bouguer's law can be integrated to give

$$i_{\lambda}(S) = i_{\lambda}(0) \exp(-a_{\lambda}S) \quad (4.11)$$

Thus, the initial intensity  $i_{\lambda}(0)$  decreases exponentially with increasing path length and absorption coefficient.

To estimate the radiative transfer using Equation 4.11, we assume the heat source is ideal and seek estimates of the spectral absorption coefficient. The spectral intensity distribution of the assumed black heat exchanger source at an upper temperature limit is shown in Figure 4.13. Hale and Querry (1973) report spectral properties of water over a large wavelength range. The spectral absorption coefficients for water are shown in Figure 4.14. By Wien's displacement law, the peak intensity occurs at a wavelength of  $9.26\mu\text{m}$ . The spectral absorption is very strong about the wavelengths of maximum intensity.

Because of the large magnitude in the spectral absorption coefficient in this range, the entire initial intensity will be diminished in a very short distance ( $\ll 1\text{mm}$ ). With such a short radiative pathlength, the temperature differences are very small; therefore, the net radiation heat transfer from the heat exchanger is negligible.

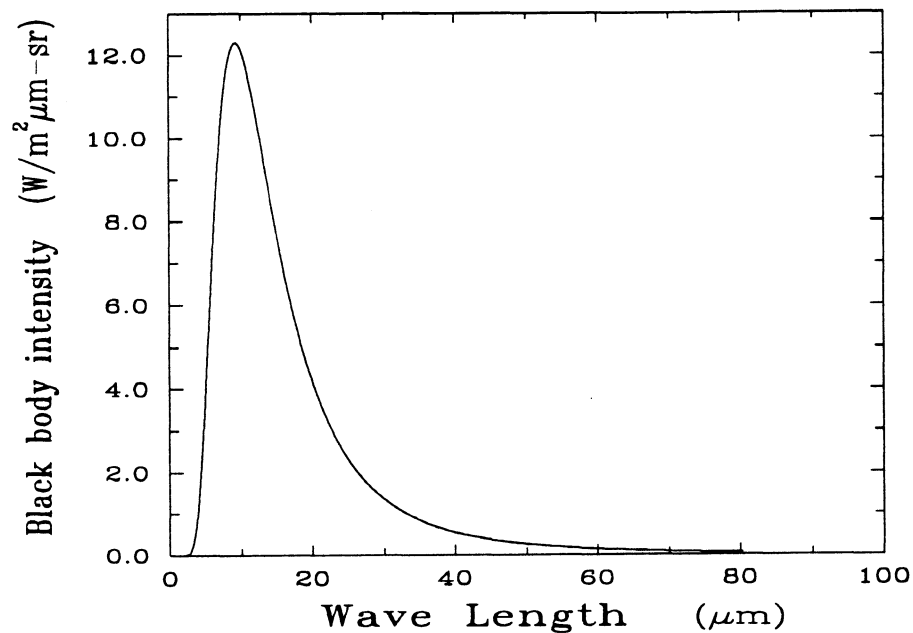


Figure 4.13: Ideal (black) body spectral intensity at  $T=313\text{K}$ .

The numerical computations assume the enclosure is adiabatic. Of course from an experimental standpoint, a perfectly insulated enclosure is not possible. Two steps can be taken to account for the imperfect enclosure boundary condition. First, the enclosure can be carefully insulated to minimize heat loss. Second, the computed heat flux/Nusselt

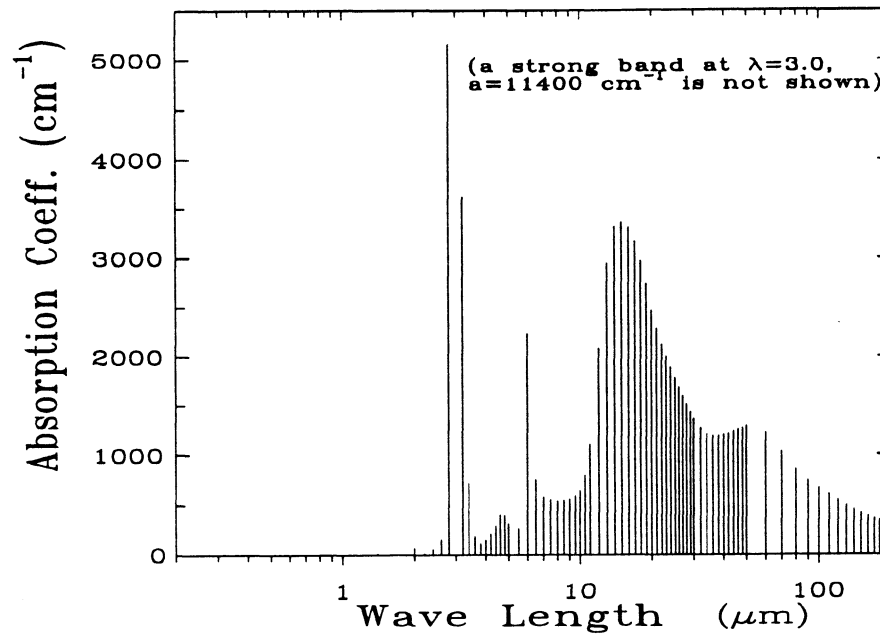


Figure 4.14: Spectral absorption coefficients for water.

number results can be corrected if the heat loss can be characterized. It should be noted that the actual flow field in the experimental configuration will differ slightly compared to the numerical computations due to the heat loss. The enclosure is insulated with a dual foil faced bubble type plastic insulation<sup>15</sup>. The insulation has a low thermal conductivity

<sup>15</sup> Model "Astro-Foil" from Rotech Industries, Inc.; Crown Point, Indiana.

(~0.0228 W/m-C) and a high reflectivity (~0.9). The insulation is applied to the enclosure in two layers: first, a loose fitting inner layer to break up the air gap that exists between the enclosure and the outer layer of insulation and second, the outer layer of insulation.

The heat loss from the enclosure is characterized by performing "cool down" experiments. The first step in a cool down experiment is to heat the working fluid in the enclosure to some target temperature. After removing the power supplied to the heat exchanger, bulk and ambient temperatures are monitored over time as the enclosure loses its internal energy to the relatively cooler surroundings. A simple energy balance on the enclosure during cool down gives

$$\bar{h}_L A_o (\bar{T}(t) - T_\infty) = (mc)_{\text{tank}} \frac{d\bar{T}}{dt} \quad (4.12)$$

where:  $\bar{h}_L$  is the average overall heat loss coefficient,  $A_o$  is the external area of the insulated enclosure,  $\bar{T}$  is the enclosure bulk temperature,  $T_\infty$  is the ambient temperature,  $(mc)_{\text{tank}}$  is a mass capacitance of the composite enclosure and working fluid, and  $t$  is time. The goal is to determine the average heat loss coefficient,  $\bar{h}_L$ .

Two approaches are used to characterize the heat loss; the first assumes the average heat loss coefficient is constant during the cool down and the second method assumes that the loss coefficient (in terms of an average Nusselt number) is a function of the Rayleigh number as given by Equation 4.13.

$$\overline{Nu}_L = C_o \overline{Ra}_H^n \quad (4.13)$$

where  $C_o$  is a correlating constant, and  $n$  a correlating exponent. The Rayleigh number  $\overline{Ra}_H$  is based on a characteristic dimension,  $H$ , which represents the total insulated enclosure height and a characteristic temperature difference,  $(\overline{T} - T_\infty)$ . Assuming the average heat loss during cool down is constant, Equation 4.12 can be integrated resulting in the following

$$\overline{T}(t) = T_\infty + (\overline{T}_o - T_\infty) \exp\left[-\frac{\overline{h}_L A_o t}{(mc)_{tank}}\right] \quad (4.14)$$

A heat loss coefficient of 0.59 W/m<sup>2</sup>-C (0.104 Btu/hr-ft<sup>2</sup>-F) provided a best fit to the experimental cool down data resulting in a standard error of 0.033 with Equation 4.14 explaining 99.85% of the variation in the actual cool down data.

When the heat loss is assumed to be a function of the Rayleigh number according to Equation 4.13, the bulk temperature is given by

$$\overline{T}(t) = T_\infty + \left[ \frac{n C_o k_{air} A_o}{H (mc)_{tank}} \left( \frac{g \beta H^3}{\nu \alpha} \right)_{air} t + (\overline{T}_o - T_\infty)^{-n} \right]^{-1/n} \quad (4.15)$$

The subscript *air* denotes an air property. All properties are evaluated at the mean film temperature  $((\overline{T}_o + T_\infty)/2)$ . The results from three cool-down runs are averaged and coefficients of  $n=1/4$  and  $C_o=0.0928$  result in a standard error of 0.0027 and explain 99.99% of the variation in the experimental cool down results. The cool down data including the best fit loss coefficient are shown in Figure 4.15. For the remainder of the experimental analysis, the heat loss will be estimated using the loss coefficient based on the Rayleigh number as given in Equation 4.16.

$$q_L = \frac{0.0928 \overline{Ra}_H^{1/4} A_o k_{air}}{H} (\overline{T} - T_\infty) \quad (4.16)$$

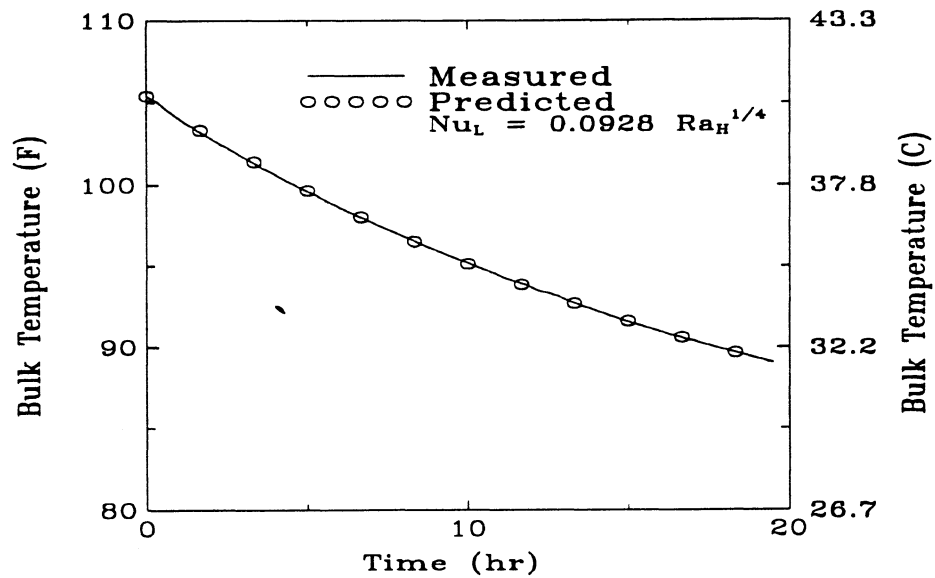


Figure 4.15: Experimental data characterizing heat loss during cool down from the insulated experimental enclosure.

Section 4.1 discussed the necessity of a linear temperature-specific volume relationship of the working fluid for allowing bulk temperature to be determined by measuring the volume expansion. Figure 4.1 showed the temperature - specific volume relationship while Figure 4.6 showed the probe output as a function of the volume added to the expansion column. The desired relationship gives bulk temperature as a function of the change in the capacitance probe output. The relationship is determined by combining the probe response in Figure 4.6 along with the property data in Figure 4.1. The resulting

relationship between bulk temperature and the change in capacitance probe output is shown in Figure 4.16. The bulk temperature data are straight line fitted with a standard error of 0.79 C (1.42 F) and explains 99.2% of the deviation in the actual data.

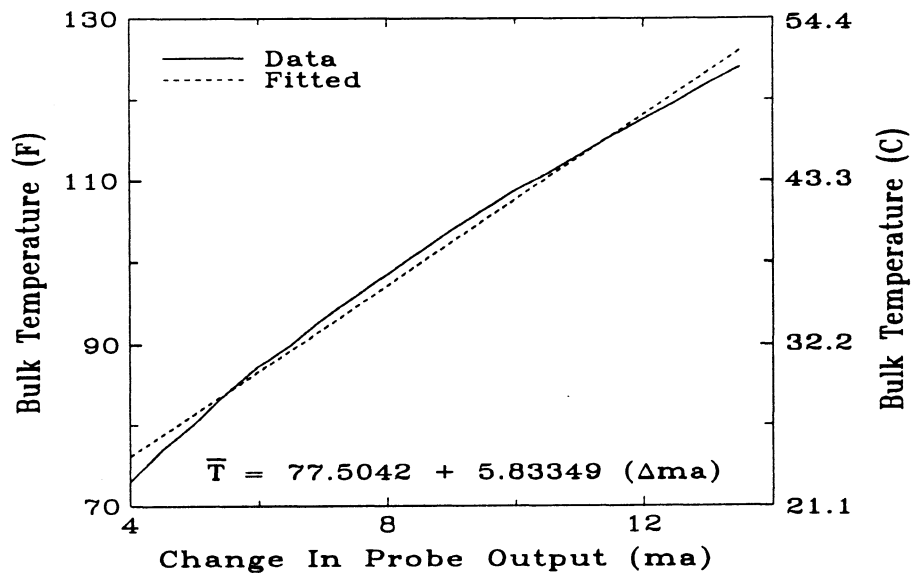


Figure 4.16: Bulk temperature as a function of change in capacitance probe output,  $\Delta ma = (ma_{final} - ma_{initial})$  ( $T_{ref} = 23.9$  C, 75 F).

### 4.3 Uncertainty Analysis

An integral constituent of experimentation is uncertainty analysis. Uncertainty analysis is a formal method for assessing the accuracy of derived quantities while taking into account all of the elemental accuracies of the measured variables involved in

determining the desired quantity of interest. The methods of uncertainty analysis used in this research are based on those given by ANSI/ASME Standard on *Measurement Uncertainty* which is also documented by Coleman and Steele, (1989).

A measurement error can be decomposed into two components: bias and precision errors. A bias error can be thought of as a fixed deviation of the mean measured value from the true value. Precision errors are more stochastic in nature. In general, precision errors are treated statistically. In this research, all precision errors are assumed to be normally distributed and a 95% level of confidence is used in all associated confidence intervals.

The formulation of error analysis equations is essentially the same when considering both bias and precision error elements; however, details in quantifying the specific error behavior in each case differ. First, general uncertainty relationships are derived for each quantity of interest. Then specific bias and precision error estimates are sought. The formulation of the uncertainty estimates is based on considering a first order Taylor series expansion in  $n$ -dimensions. The uncertainties are then expressed in a root sum of squares.

#### **Uncertainty in $\overline{Nu}$ : Method 1**

The data reduction equation for the average Nusselt number in terms of the measured current supplied to the heat exchanger and a fixed heating element resistance is given by Equation 4.4. The expression for the root sum of square error associated with this formulation of  $\overline{Nu}$  is given by

$$\begin{aligned}
\delta \overline{Nu}^2 = & \left( \frac{\partial \overline{Nu}}{\partial I} \delta I \right)^2 + \left( \frac{\partial \overline{Nu}}{\partial R} \delta R \right)^2 + \left( \frac{\partial \overline{Nu}}{\partial k_w} \delta k_w \right)^2 + \\
& \left( \frac{\partial \overline{Nu}}{\partial R_x} \delta R_x \right)^2 + \left( \frac{\partial \overline{Nu}}{\partial T_w} \delta T_w \right)^2 + \left( \frac{\partial \overline{Nu}}{\partial T_o} \delta T_o \right)^2 + \\
& \left( \frac{\partial \overline{Nu}}{\partial \bar{h}_L} \delta \bar{h}_L \right)^2 + \left( \frac{\partial \overline{Nu}}{\partial A_o} \delta A_o \right)^2 + \left( \frac{\partial \overline{Nu}}{\partial \bar{T}} \delta \bar{T} \right)^2 + 2\rho_{T_w, T_o} \frac{\partial \overline{Nu}}{\partial T_w} \frac{\partial \overline{Nu}}{\partial T_o} \delta T_w \delta T_o
\end{aligned} \tag{4.17}$$

Where  $\delta$  represents a general error (bias or precision error) in a particular quantity and  $\rho_{T_w, T_o}$  is the correlation coefficient between two variables (wall and initial temperatures in this case). After computing the appropriate derivatives and substituting into the above equation, the general error equation becomes

$$\begin{aligned}
\delta \overline{Nu}^2 = & \frac{1}{C_1^2} \{ (2RI\delta I)^2 + (I^2\delta R)^2 + \left( C_2 \frac{\delta k_w}{k_w} \right)^2 + \left( C_2 \frac{\delta R_x}{R_x} \right)^2 + \\
& \left( C_2 \frac{\delta T_w}{\Delta T} \right)^2 + \left[ (\bar{h}_L A_o (\bar{T} - T_w) + I^2 R) \frac{\delta T_o}{\Delta T} \right]^2 + (A_o \Delta \bar{T} \delta \bar{h}_L)^2 + (\bar{h}_L \Delta \bar{T} \delta A_o)^2 + \\
& (\bar{h}_L A_o \delta \bar{T})^2 - 2\rho_{T_w, T_o} C_2 (I^2 R + \bar{h}_L A_o (\bar{T} - T_w)) \frac{\delta T_w \delta T_o}{\Delta T^2} \}
\end{aligned} \tag{4.18}$$

where  $C_1 = 2\pi^2 k_w R_x \Delta T$ ,  $C_2 = \bar{h}_L A_o \Delta T + I^2 R$ ,  $\Delta T = (T_w - T_o)$ , and  $\Delta \bar{T} = (\bar{T} - T_o)$ .

### Uncertainty in $\overline{Nu}$ : Method 2

The second method for estimating the average Nusselt number relies on computing the power supplied to the heat exchanger by measuring the current and the voltage from the phase fired relay. The voltage and current must both be monitored continuously during

the experiment and the output from each must represent the RMS of the chopped wave signal. The uncertainty expression for method 2 using the respective data reduction equation (Equation 4.5) is similar to that for method 1 and is given by

$$\begin{aligned} \delta \overline{Nu}^2 = & \frac{1}{C_1^2} \{ (V\delta I)^2 + (I\delta V)^2 + \left( C_2 \frac{\delta k_w}{k_w} \right)^2 + \left( C_2 \frac{\delta R_x}{R_x} \right)^2 + \\ & \left( C_2 \frac{\delta T_w}{\Delta T} \right)^2 + \left[ (\bar{h}_L A_o (\bar{T} - T_w) + I^2 R) \frac{\delta T_o}{\Delta T} \right]^2 + (A_o \Delta \bar{T} \delta \bar{h}_L)^2 + (\bar{h}_L \Delta \bar{T} \delta A_o)^2 + \\ & \left. (\bar{h}_L A_o \delta \bar{T})^2 - 2\rho_{T_w, T_o} C_2 (I^2 R + \bar{h}_L A_o (\bar{T} - T_w)) \frac{\delta T_w \delta T_o}{\Delta T^2} \right\} \end{aligned} \quad (4.19)$$

### Uncertainty in $\overline{Nu}$ : Method 3

The last method for approximating the average Nusselt number considers the time rate of change in the enclosure bulk temperature. The data reduction equation for the average Nusselt number in terms of the enclosure bulk temperature is given by Equation 4.6. After simplifying the expression for the root sum of square error associated with  $\overline{Nu}$  the following general error expression results

$$\begin{aligned} \delta \overline{Nu}^2 = & \frac{1}{C_1^2} \left\{ \left( \frac{d\bar{T}}{dt} \delta (mc)_{i,ank} \right)^2 + \left( C_3 \frac{\delta k_w}{k_w} \right)^2 + \left( C_3 \frac{\delta R_x}{R_x} \right)^2 + \left( C_3 \frac{\delta T_w}{\Delta T} \right)^2 + \right. \\ & \left[ \left( (mc)_{i,ank} \frac{d\bar{T}}{dt} + \bar{h}_L A_o (\bar{T} - T_w) \right) \frac{\delta T_o}{\Delta T} \right]^2 + (A_o \Delta \bar{T} \delta \bar{h}_L)^2 + \left( (mc)_{i,ank} \delta \left( \frac{d\bar{T}}{dt} \right) \right)^2 + \\ & \left. (\bar{h}_L A_o \delta \bar{T})^2 + (\bar{h}_L \Delta \bar{T} \delta A_o)^2 + 2\rho_{T_w, T_o} C_3 \left( (mc) \frac{d\bar{T}}{dt} + \bar{h}_L A_o (\bar{T} - T_w) \right) \frac{\delta T_o \delta T_w}{\Delta T^2} \right\} \end{aligned} \quad (4.20)$$

where  $C_3 = \bar{h}_L A_o \Delta T + (mc)_{i,ank} d\bar{T}/dt$ .

### Uncertainty in $\bar{T}$

The data reduction equation for the enclosure bulk temperature as a function of the column fluid height is a simple linear function of the change in capacitance probe output ( $\bar{T} = a + b(\Delta ma)$ ). A general expression for the error associated with the bulk temperature is given by

$$(\delta\bar{T})^2 = (\delta a)^2 + \{(\Delta ma)\delta b\}^2 + \{b\delta(\Delta ma)\}^2 \quad (4.21)$$

where  $a$  and  $b$  are coefficients obtained from the bulk temperature - capacitance probe curve fit,  $\Delta(ma)$  is the corrected change in capacitance probe output ( $ma - ma_o$ ), and  $\delta a$  and  $\delta b$  include the standard error of the coefficients from the curve fit.

### Uncertainty in $\bar{h}_L$

The uncertainty in the heat loss is required by the expressions for the uncertainty in the average Nusselt number. Since the heat loss varies as a function of time, the uncertainty in the heat loss as a function of time will also vary; consequently, we seek a detailed expression for the uncertainty in the heat loss coefficient. The heat loss is characterized by lumping all the loss transport phenomena into a single coefficient and correlating an expression for heat loss based on a bulk temperature and ambient temperature difference. An expression for the combined heat loss is found by rearranging Equation 4.13.

$$\bar{h}_L = \frac{C_o g^n \beta_{air}^n H^{3n-1} (\bar{T} - T_\infty)^n k_{air}}{H v_{air}^n \alpha_{air}^n} \quad (4.22)$$

where the *air* subscript denotes properties of air evaluated at a mean temperature of  $T_{mean} = (T_w + T_o)/2$ ,  $C_o=0.0928$ ,  $n=1/4$ ,  $H$  is the insulated enclosure height, and  $T_\infty$  is the ambient temperature. The general error equation for the heat loss coefficient is

$$(\delta \bar{h}_L)^2 = n^2 \left\{ \left( \frac{\delta g}{g} \right)^2 + \left( \frac{\delta \beta}{\beta} \right)^2 + \left( (3 - 1/n) \frac{\delta H}{H} \right)^2 + \left( \frac{\delta \bar{T}}{\Delta \bar{T}} \right)^2 + \left( \frac{\delta T_\infty}{\Delta \bar{T}} \right)^2 + \left( \frac{\delta \alpha}{\alpha} \right)^2 + \left( \frac{\delta v}{v} \right)^2 \right\} \quad (4.23)$$

### Uncertainty in $d\bar{T}/dt$

The uncertainty in the time rate of change in bulk temperature is determined by considering a discretized approximation to the derivative.

$$\frac{d\bar{T}}{dt} \approx \frac{(\bar{T}^{i+1} - \bar{T}^{i-1})}{2\Delta t} \quad (4.24)$$

where the superscript  $i$  denotes the timestep. Equation 4.24 represents a second order central difference approximation to the continuous quantity,  $d\bar{T}/dt$ . The general error equation for the time rate of change in bulk temperature, using Equation 4.24 as the data reduction equation, is given by

$$\left( \frac{\delta d\bar{T}/dt}{d\bar{T}/dt} \right)^2 = \left( \frac{\delta \bar{T}^{i+1}}{\Delta \bar{T}} \right)^2 + \left( \frac{\delta \bar{T}^{i-1}}{\Delta \bar{T}} \right)^2 + \left( \frac{\delta t}{\Delta t} \right)^2 - 2\rho_{\bar{T}^{i+1}, \bar{T}^{i-1}} \frac{\delta \bar{T}^{i+1} \delta \bar{T}^{i-1}}{\Delta \bar{T}^2} \quad (4.25)$$

The general error equation can be simplified for both the bias and precision error components. For the bias error, the bulk temperature at all times is measured by the same instrument; therefore, the correlation coefficient  $\rho_{\bar{T}^{i+1}, \bar{T}^{i-1}}$  is unity. The general data reduction equation simplifies to give the bias error estimate as

$$B \left( \frac{d\bar{T}}{dt} \right) = \frac{(\bar{T}^{i+1} - \bar{T}^{i-1})}{2\Delta t^2} \delta t \quad (4.26)$$

For the precision error component, we assume the errors (precision) in the time dependent bulk temperature quantities  $\bar{T}^{i+1}, \bar{T}^{i-1}$  are independent and uncorrelated which yields

$$\left( \frac{P d\bar{T}/dt}{d\bar{T}/dt} \right)^2 = \left( \frac{P \bar{T}^{i+1}}{\Delta \bar{T}} \right)^2 + \left( \frac{P \bar{T}^{i-1}}{\Delta \bar{T}} \right)^2 + \left( \frac{P \delta t}{\Delta t} \right)^2 \quad (4.27)$$

In a detailed uncertainty analysis, the errors are separated into bias and precision components. In the analysis that follows, all precision errors are computed at a 95% level of confidence. Table 4.3 provides a summary of the bias and precision error values used in the uncertainty analysis.

Variable	Est. Bias	Nominal Value	% Bias (Est/Nominal)
$I$ , (amps)	$\pm 0.1$	time dep.	time dep.
$R$ , (ohms)	$\pm 1.3$	59.7	$\pm 2.2$
$V$ , (volts)	$\pm 6.8$	240	$\pm 2.8$
$ma$ , (milli-amps)	-	-	$\pm 1$
$r_x$ , (cm)	$\pm 0.0127$	1.27	$\pm 1$
$R_x$ , (cm)	$\pm 0.25$	7.94	$\pm 3$
$R_T$ , (cm)	$\pm 0.21$	10.35	$\pm 2$
$H_T$ , (cm)	$\pm 0.40$	20.7	$\pm 2$
$H$ , (cm)	$\pm 0.61$	40.64	$\pm 1.5$
$g$ , (m/s <sup>2</sup> )	$\pm 0.29$	9.81	$\pm 3$
$k$ (air and water)	-	-	$\pm 5$
$\alpha$ (air and water)	-	-	$\pm 5$
$\nu$ (air and water)	-	-	$\pm 5$
$\beta$ (air and water)	-	-	$\pm 5$
$t$ (sec)	-	-	$\pm 0.5$
$T_o$ (C, F)	$\pm 1.41, \pm 2.54$	23.9, 75	$\pm 6$
$T_w$ (C, F)	$\pm 1.41, \pm 2.54$	-	-
$T_\infty$ (C, F)	$\pm 1.41, \pm 2.54$	23.9, 75	$\pm 6$
$A_o$ (m <sup>2</sup> , ft <sup>2</sup> )	$\pm 0.00691, \pm 0.0744$	0.6911, 7.44	$\pm 10$
$(mc)_{tank}$ (J/C)	$\pm 4700$	47,000	$\pm 10$
$\bar{T}$ (F) { $T_{ref}=71$ }	$\pm \{1.09 + 0.0126(\Delta ma)^2\}^{1/2}$	-	-

Table 4.3a: Compilation of the magnitude of individual bias errors

Variable	Est. std. Error	95% level Est.
$I$ , (amps)	$\pm 0.002$	$\pm 0.004$
$R$ , (ohms)	$\pm 0.01$	$\pm 0.02$
$r_x$ , (cm)	$\pm 0.04$	$\pm 0.08$
$R_x$ , (cm)	$\pm 0.0794$	$\pm 0.159$
$R_T$ , (cm)	$\pm 0.0794$	$\pm 0.159$
$H_T$ , (cm)	$\pm 0.0794$	$\pm 0.159$
$H$ , (cm)	$\pm 0.159$	$\pm 0.318$
$A_o$ , (m <sup>2</sup> )	$\pm 0.00691$	$\pm 0.0138$
$T_o$ (C, F)	$\pm 0.022, \pm 0.04$	$\pm 0.044, \pm 0.08$
$T_w$ (C, F)	$\pm 0.022, \pm 0.04$	$\pm 0.044, \pm 0.08$
$ma$ , (milli-amps)	$\pm 0.00584$	$\pm 0.0117$
$\bar{T}$ (F)	$\pm 0.06$	$\pm 0.12$
$t$ (sec)	$\pm 0.5$	$\pm 1.0$

Table 4.3b: Compilation of the magnitude of individual precision errors

The relevant individual bias and precision errors above are used in the general uncertainty equations to compute the respective bias and precision uncertainty for the quantity of interest. After the bias and precision errors are computed, they can be combined to estimate the overall uncertainty by the following

$$Uf = \sqrt{\{Bf^2 + Pf^2\}} \quad (4.28)$$

where  $Uf$  is the overall uncertainty in the quantity  $f$ ,  $Bf$  is the bias error component of  $f$ , and  $Pf$  is the precision error component of  $f$ . Equation 4.27 is known as the root sum square formulation of uncertainty.

Computing the uncertainty in the average Nusselt number requires characterizing the uncertainty in the heat loss coefficient. The fractional uncertainty in the heat loss coefficient is computed by considering bias and precision error components individually.

The bias error component of the heat loss coefficient is found by substituting the bias error values given Table 4.3a into Equation 4.23. The precision error estimate for the heat loss coefficient is found in the same manner; however, the property values are assumed to be "frozen" values obtained from either thermodynamic correlations or appropriate tables. Thus, there is no precision error associated with obtaining the values. The uncertainty of the heat loss is a function of the bulk temperature and the error is higher at low values of bulk temperature. The behavior of the uncertainty over a bulk temperature range encountered in the experiments is shown in Figure 4.17. The fractional uncertainty in the heat loss coefficient ranges from 20% at low values of bulk temperature to approximately 2% at high values of bulk temperature.

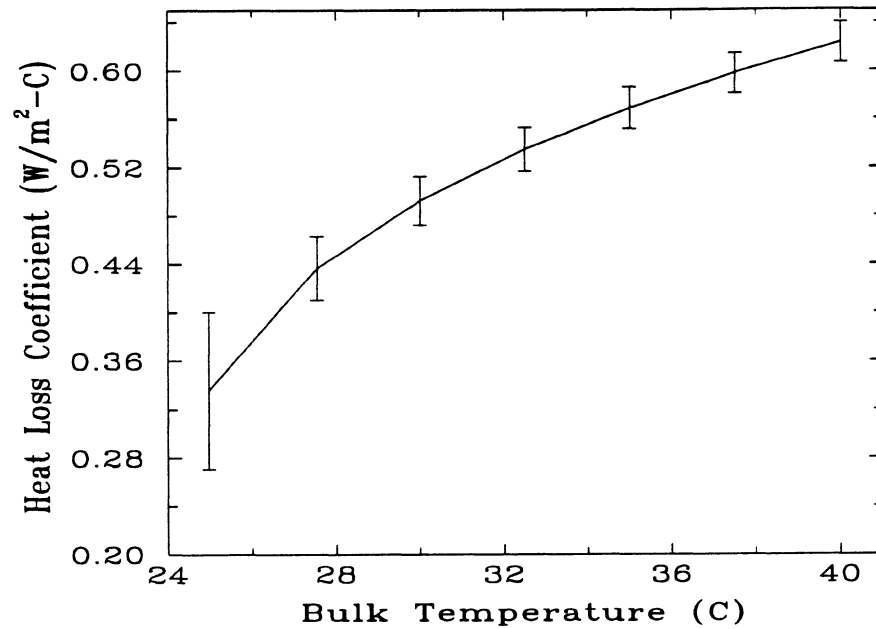


Figure 4.17: Heat loss coefficient dependence on bulk temperature including error bars.

## 4.4 Results

In the course of the experiments, two boundary conditions were imposed on the heat exchanger: constant heat flux and constant temperature. The results of the constant heat flux boundary condition are presented first followed by the constant temperature results.

### 4.4.1 Constant Heat Flux Source

The performance of the experimental apparatus under the transient conditions present with an isothermal heat source is difficult to assess; therefore, a simpler case of a constant

flux heat source is considered. The primary objective is to examine the performance of the bulk temperature measurement system. The heat exchanger is powered with a direct current power supply<sup>16</sup> which reduces the uncertainty in the transient accuracy of the current control and measurement systems.

The efficacy of the bulk temperature measurement system is determined by comparing the measured bulk temperature with the bulk temperature computed by an energy balance. Initially, the entire enclosure was constructed from acrylic. A typical energy balance obtained from the constant flux source using the acrylic enclosure is shown in Figure 4.18. The computed bulk temperature curve by an energy balance (including heat losses) and "measured" bulk temperature from the capacitance probe are significantly different in both magnitude and shape. Also included in Figure 4.18 is the limiting case of a perfectly insulated enclosure (energy balance with no losses).

Additional constant flux runs were made with the acrylic enclosure uninsulated. Figure 4.19 shows the response in measured bulk temperature by the capacitance probe. The resulting temperature profiles are completely unexpected. The uninsulated enclosure case apparently experiences a sharper rise in bulk temperature as indicated by the capacitance probe response. Since this behavior makes no sense, physically, alternative explanations were sought.

---

16 Model LPS 152 DC Tracking Power Supply; Leader Electronics Corporation.

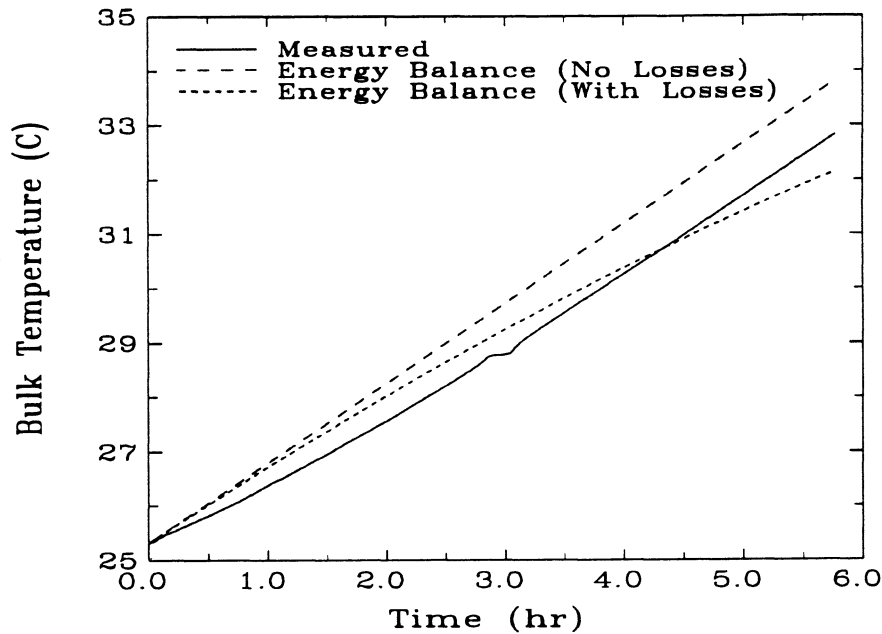


Figure 4.18: Energy balance with a constant heat flux source and acrylic enclosure.

The bulk temperature measurement system relies on monitoring the volume of fluid expanding into a column above the enclosure. Additional apparatus debugging suggested that the acrylic enclosure is experiencing thermal expansion upon heating the working fluid. Because the enclosure is significantly larger than the expansion column, small changes in the enclosure volume by thermal expansion can have a significant influence on the amount of fluid moving up the column during heating. Enclosure thermal expansion explains the behavior observed in Figure 4.19. If the enclosure is uninsulated, the surface temperature of the enclosure is lower. The lower enclosure surface temperature reduces

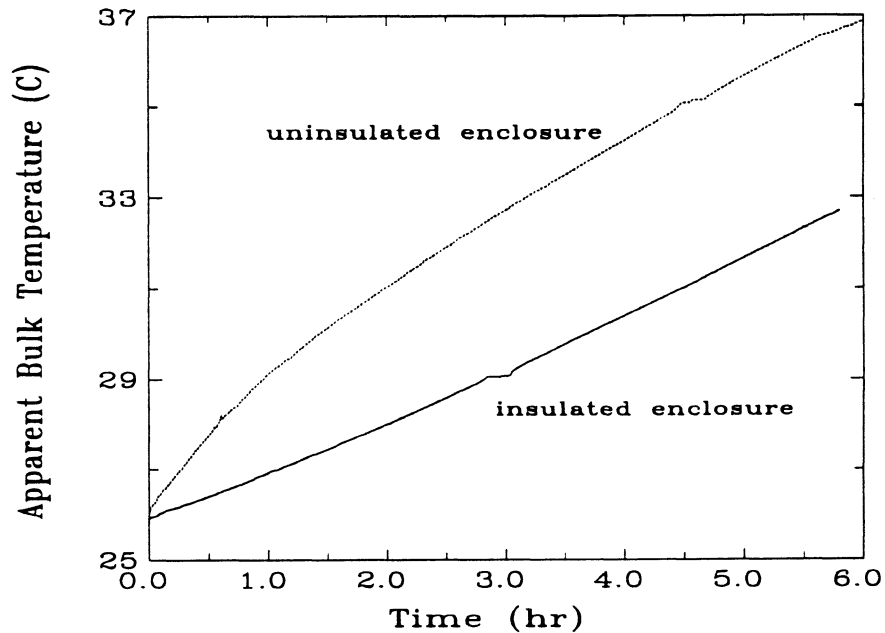


Figure 4.19: Apparent bulk temperature for acrylic enclosure with and without insulation and a constant flux heat source.

the thermal expansion which allows a higher level of working fluid to move up the column. (The net effect of enclosure thermal expansion is an underprediction of the true bulk temperature.)

The impact of enclosure thermal expansion can be illustrated by performing a simple test. The enclosure is insulated and subjected to the constant heat flux source for several hours. The power is then turned off and the enclosure insulation removed allowing relatively cooler ambient air to reach the enclosure surface. From the second law, the bulk

temperature must decrease; however, the fluid in the expansion column continues to rise as shown by the response of the capacitance probe output in Figure 4.20. The explanation for this behavior is that the cooler ambient air is causing the enclosure to contract; thereby, pushing the working fluid higher in the column and making the apparent bulk temperature rise. To minimize the effects of enclosure expansion, a new enclosure body was sought. The new enclosure body is made from a glass (Duran<sup>®</sup>) which has an order of magnitude lower thermal expansion coefficient compared to the acrylic. Figure 4.20 illustrates the action of the reduced enclosure expansion characteristics of Duran<sup>®</sup> compared with the acrylic.

It is clear from Figure 4.20 that the Duran<sup>®</sup> enclosure still experiences thermal expansion. Although the expansion is small, a first order correction is applied to compensate for the error incurred by expansion. The estimate assumes linear expansion in both the circumferential and vertical directions. The temperature difference used in computing the linear expansion is approximated by using the bulk temperature from the actual capacitance probe output (as given in Figure 4.16). The change in capacitance probe output due to enclosure expansion is given by Equation 4.29.

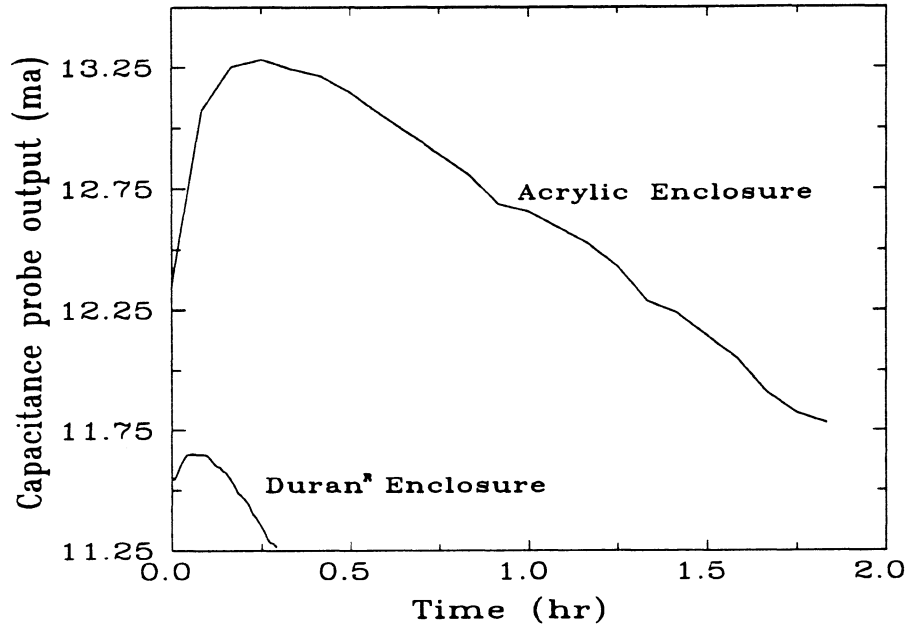


Figure 4.20: Capacitance probe response during initial enclosure cool-down after removing insulation.

$$\Delta(ma)_{corr} = \frac{\pi D_o H_o \alpha_{exp} \Delta \bar{T}}{31.435} [3(1 + \alpha_{exp} \Delta \bar{T}) + \alpha_{exp}^2 \Delta \bar{T}^2] \quad (4.29)$$

where  $\Delta(ma)_{corr}$  is the correction due to enclosure expansion,  $D_o$  and  $H_o$  are the enclosure diameter and height respectively,  $\alpha_{exp}$  is the linear expansion coefficient for Duran<sup>®</sup>, and  $\Delta \bar{T} = (\bar{T}(t) - \bar{T}(0))$ . The correction factor given by Equation 4.29 is added to the observed change in capacitance probe output resulting in a corrected probe output for use in computing corrected bulk temperature estimate with a relationship as given in Figure 4.15.

The resulting energy balance derived based on the constant heat flux condition in the Duran<sup>®</sup> enclosure is shown in Figure 4.21. The "measured" bulk temperature (corrected for enclosure expansion) compares well with the bulk temperature found by integrating the energy supplied to the heat exchanger. Figure 4.21 also shows the limiting case of a perfectly insulated enclosure.

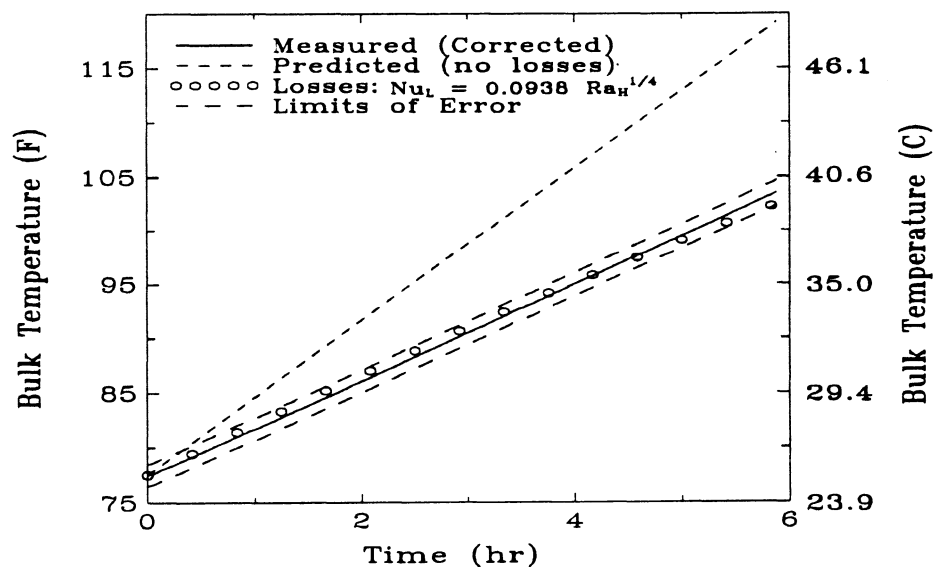


Figure 4.21: Bulk temperature by measurements and energy balance with constant flux heat source (Duran<sup>®</sup> enclosure).

The bulk temperature found by an energy balance is within the bounds of error (based on the uncertainty analysis) for the bulk temperature throughout the entire transient.

Agreement of the measured bulk temperature with the bulk temperature derived by an energy balance based on an independently measured quantity provides an increased level of confidence that the bulk temperature measurement technique is working properly. The error bars in Figure 4.21 are symmetric deviations about the measured bulk temperature. The maximum error in the bulk temperature is estimated to be 0.67 C (1.2 F). The maximum deviation of the bulk temperature based on an energy balance compared with the measured bulk temperature is 0.6 C (1.08 F). In general, the estimated error in bulk temperature is expected to be within 2% over the entire range of bulk temperatures.

#### **4.4.2 Constant Temperature Source**

Imposing a constant heat flux boundary condition is relatively simple both mathematically and physically. The constant temperature boundary condition with a step change in temperature is much more difficult to impose both mathematically and physically. An infinite heat transfer rate is required to achieve the step change initial condition. While this is possible in an mathematical setting, physically it is impossible due to the finite capacitance of the heat exchanger. The actual response of the heat exchanger is determined by the behavior of the control system employed. In this case, a PID (proportional-integral-differential) feedback control system is used to maintain the heat exchanger at the desired set temperature. A typical heat exchanger surface temperature response is shown in Figure 4.22. The heat exchanger surface temperature initially reaches the setpoint quickly but overshoots and eventually falls back to the steady set temperature.

##### **Computations:**

Due to resource constraints, the computational results given in Chapter 3 were based on an enclosure which is smaller than the experimental configuration. Thus, a numerical

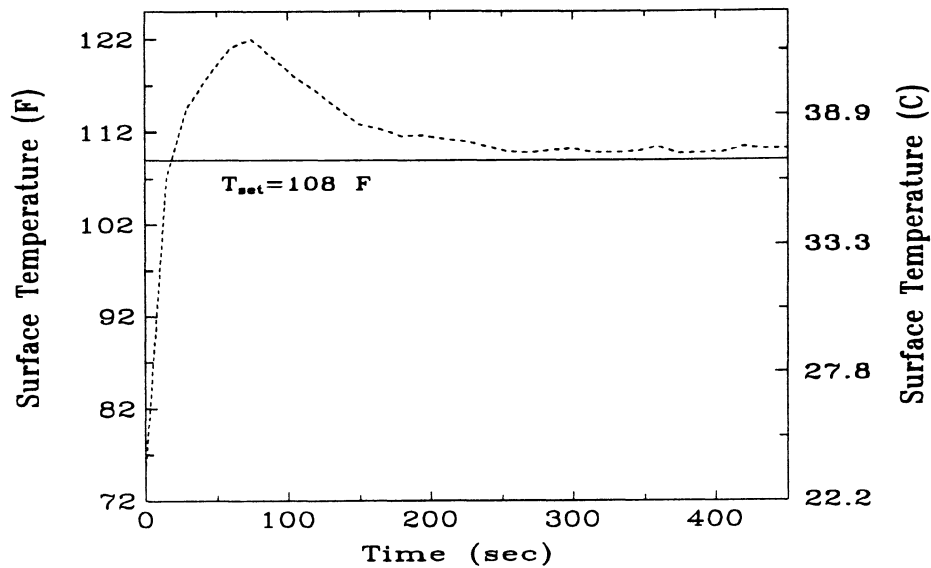


Figure 4.22: Typical, measured heat exchanger surface temperature.

solution of a geometry identical to the experimental configuration must be found. The computations also assumed an ideal step change in surface temperature. Since this condition was not experimentally possible, a typical wall temperature profile was imposed as a time dependent boundary condition for a final computation based on the experimental geometry. The finite element mesh used in the computation is shown in Figure 4.23.

Computations were performed using the mesh in Figure 4.23. Unfortunately, after approximately 21 CPU days (running on a DECStation 5000/240) the computation progressed only as far as the end of the quasi-steady regime. The magnitude of the average

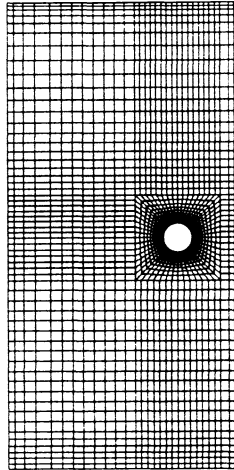


Figure 4.23: Finite element mesh for experimental geometry.

Nusselt number obtained from the computation was in agreement with the correlation for the long horizontal cylinder in an infinite medium given by Morgan (1975) during this time period.

#### **Experimental Results:**

Several sequences of experimental runs were made to assure that the data taken is repeatable. Figure 4.24 shows the bulk temperature response of three runs with the heat exchanger subjected to the isothermal boundary condition. The dashed line represents the three run average. All data are within the error limits determined by the uncertainty analysis presented in Section 4.3.

The time dependent average Nusselt number is determined from two techniques: measured current (Equation 4.4) and measured bulk temperature (Equation 4.6). The expected magnitude of heat transfer during the quasi-steady regime is given by a correlation (Morgan, 1975) for a long horizontal cylinder in an infinite medium. The duration of the quasi-steady regime is predicted by scale analysis (Equation 3.14). The results for the

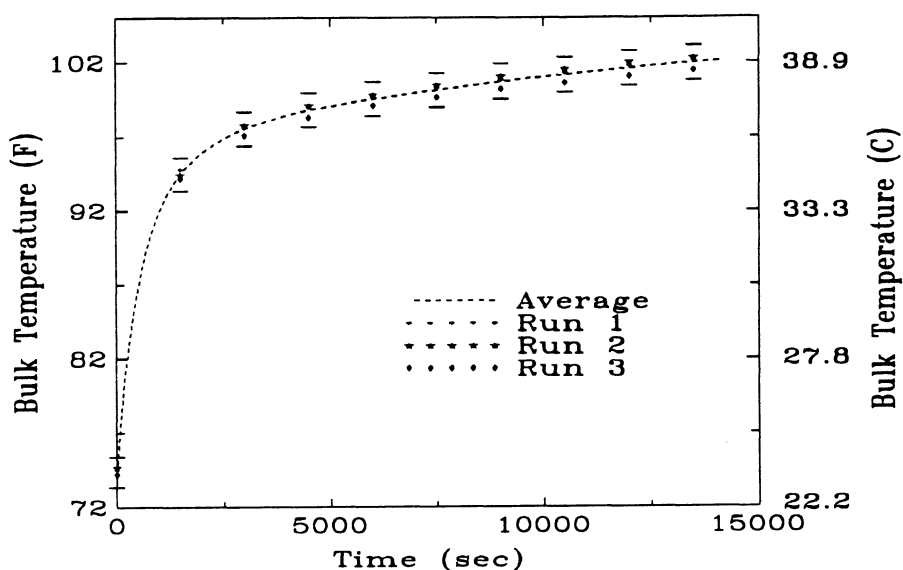


Figure 4.24: Repeatability of the bulk temperature response.

temporal heat transfer response, expressed in terms of an average Nusselt number, are shown in Figure 4.25. Included in Figure 4.25 is the expected magnitude and duration of the "quasi-steady" regime.

Several observations from Figure 4.25 are in order. First, neither the heat transfer results based on measured current nor the results based on bulk temperature compare with the expected quasi-steady regime. The heat transfer never appears to behave as if it were in an infinite medium (as would be indicated by a plateau in the temporal heat transfer response). Second, the difference between the heat transfer predicted by measured current

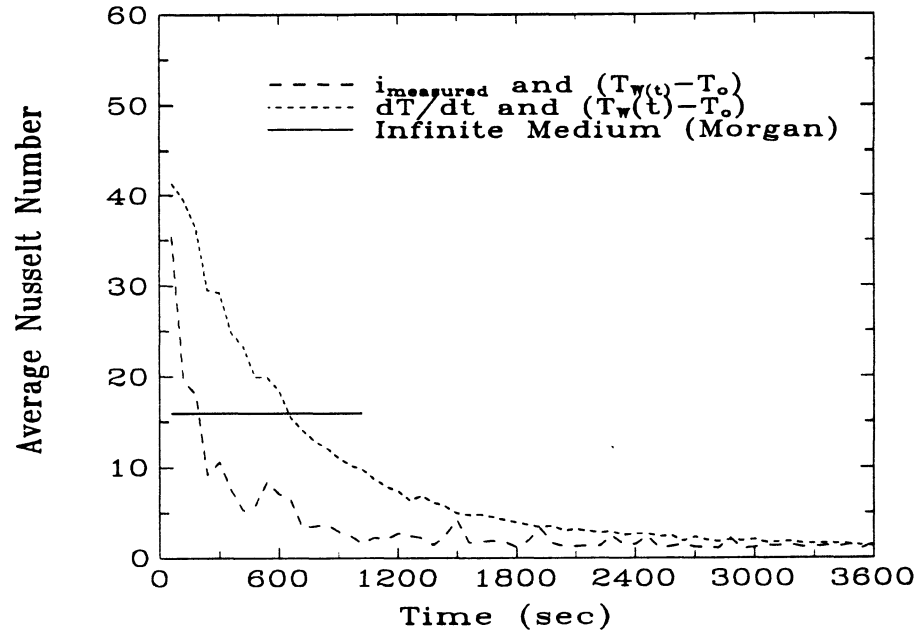


Figure 4.25: Experimental results for average Nusselt number by measured current and time rate change in bulk temperature (one minute time average results over three runs).

and bulk temperature are significant. The author believes that the measured current results are incorrect. The current measurements suffer from the inherent difficulty in evaluating the RMS current of a chopped alternating current waveform whose average value is continuously changing (a result of the phase angle fired solid state relay coupled with the PID controller). The author believes the heat transfer results based on the time rate change in bulk temperature are correct. This conclusion is based on the results given in Section 4.4.1 for the constant current boundary condition. Under the constant current conditions,

the energy supplied to the heat exchanger is easily and accurately measured. Furthermore, Figure 4.21 showed good agreement between the measured bulk temperature and the bulk temperature derived from an energy balance based on the measured current. The agreement lends a high level of confidence in the bulk measurement technique. Thus, the average Nusselt number results based on measured current will be disregarded in the remaining analysis.

The question still remains: why is there a significant difference between the measured and numerical (based on two-dimensional) computations? An unexplored area at this point in the experimental analysis is actual fluid flow field measurements. In an effort to gain a better understanding of the fluid flow field, a simple flow visualization technique is engaged. A shadowgraph technique is used to observe the behavior of bulk flow patterns ascending from the heated coil. Because of the enclosure's cylindrical configuration, the flexibility of the viewing angles are limited to those in the plane of the major coil axis. Figure 4.26 shows the arrangement used to obtain the shadowgraph results. The light source is oriented perpendicular to the enclosure surface and projected such that the shadow of the coil appears on a screen behind the enclosure. Density differences in the flow field cause changes in fluid's index of refraction which result in producing shadows on the screen behind the enclosure. The movement of the shadows is used to qualitatively study the structure of the velocity flow field.

The transient begins by supplying full power to the heat source in an attempt to achieve the sharp change in wall temperature. After the initial supply of power to the source, no fluid movement is noticed for approximately six seconds. The behavior of the observed delay in flow is consistent with the prediction of an initial pure conduction regime. The time period of the delay agrees with the predicted duration of the conduction dominated

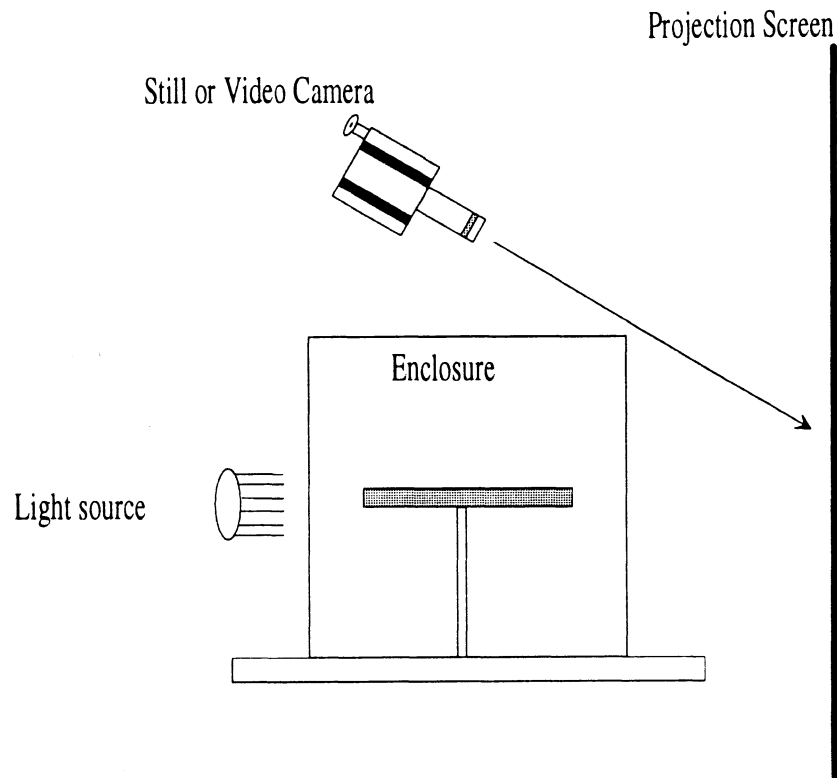


Figure 4.26: Shadowgraph setup.

regime by scale analysis. After the initial delay, a front of warm fluid rises above the coil. Immediately, the warm front of fluid begins to buckle into a mushroom shaped plume formation and fluid cells begin to appear. (The computations showed plumes forming in the plane of the minor axis as well suggesting that the plumes are truly conical or mushroom shaped in three dimensions.) The centers of each plume continue to rise as their shape becomes distorted until finally moving out of the shadowgraph control volume. As the flow continues to develop, distinct cells of fluid exist above the source.

Upon startup, the temperature of the coil eventually overshoots the setpoint and the energy supplied to the source is cut-off by the controller. As the coil temperature decreases, the controller begins proportioning the necessary energy to the coil to maintain its

temperature. Unfortunately, the coil temperature is not constant but fluctuates about the setpoint because of the varying power supplied by the controller-relay setup. The fluctuation of power supplied to the coil has an adverse impact on the flow from the coil. Each time the coil is powered on by the controller, a new front/wave of warm fluid rises above the source. The effect of the controller pulsing the coil power on and off is a greater mixing action of the fluid in the enclosure that would otherwise not occur. On a large scale, the time average (15 second) power supplied to the heat source appears to be smooth; however, on a smaller scale the pulsing source fundamentally changes the coil boundary condition compared to that used in the computations. The net effect is the boundary condition on the coil in the experiment not consistent with the boundary condition imposed in the numerical computations.

Figure 4.27 shows a sequence of photographs taken just when a new front or wave of fluid is building above the coil tube heat source. Figure 4.27a shows that the warm front of fluid above the coil is composed of cell like structures with the mushroom shaped plumes forming at the apex of the wave cells. As the front ascends, some of the plume cells coagulate while others narrow. As the front continues to move up, the mushroom shape of the plumes become distorted and eventually unrecognizable. Eventually, the entire front is ejected from the immediate neighborhood above the coil and moves to the top of the enclosure. This occurs when the temperature of the coil is moving down during its cycle about the setpoint. The entire cycle time between front ejections is approximately 20 seconds (this cycle time is observed relatively early in the transient i.e. within 30 minutes from the start).

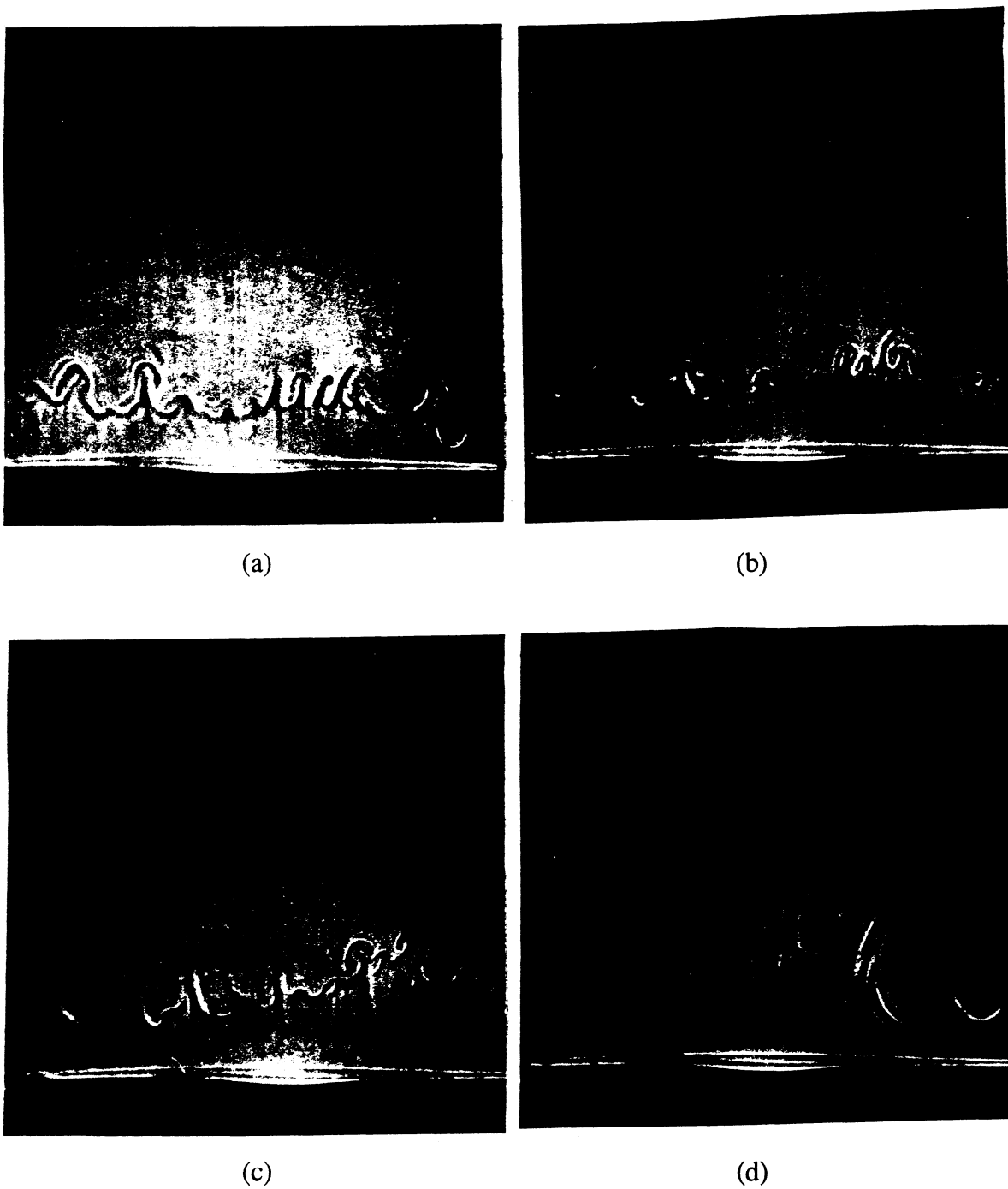


Figure 4.27: Sequence of shadow graphs approximately 2 seconds apart.

The measured heat transfer response appears to be continuously diminishing throughout the entire transient. It is indicative of the behavior experienced during the decay period in the numerical computations. In Chapter 3, scale analysis is used to identify a group of parameters to correlate the decay period (Equation 3.19). The grouping of parameters in Equation 3.19 assumed the mass-capacitance product included only the working fluid (numerically, the enclosure did not have mass); however, the experimental enclosure has significant thermal mass. Generalizing Equation 3.19 to include a mass-capacitance product of the entire enclosure (working fluid + tank) results in the following relationship

$$\overline{Nu} \sim C_1 \left[ 1 + \frac{\pi^2 k R_x Ra_D^{1/4} t}{4 (mc)_{tank}} \right]^{-5} Ra_D^{1/4} \quad (4.30)$$

where  $k$  is the thermal conductivity of water (evaluated at  $\{T_w + T_o\}/2$ ),  $R_x$  is the major radius of the heat exchanger, and  $(mc)_{tank}$  is a mass-capacitance product including working fluid and enclosure structure.

The dimensional grouping identified in Equation 4.30 was compared with the measured transient average Nusselt number. Obtaining the single constant ( $C_1=1.407$ ) by least squares comparison with the measured data yields a single correlation that describes the transient response of the actual heat exchanger. The agreement between Equation 4.31 and the measured average Nusselt number over the entire transient is excellent as shown by Figure 4.28.

$$\overline{Nu} \sim 1.407 \left[ 1 + \frac{\pi^2 k R_x Ra_D^{1/4} t}{4 (mc)_{tank}} \right]^{-5} Ra_D^{1/4} \quad (4.31)$$

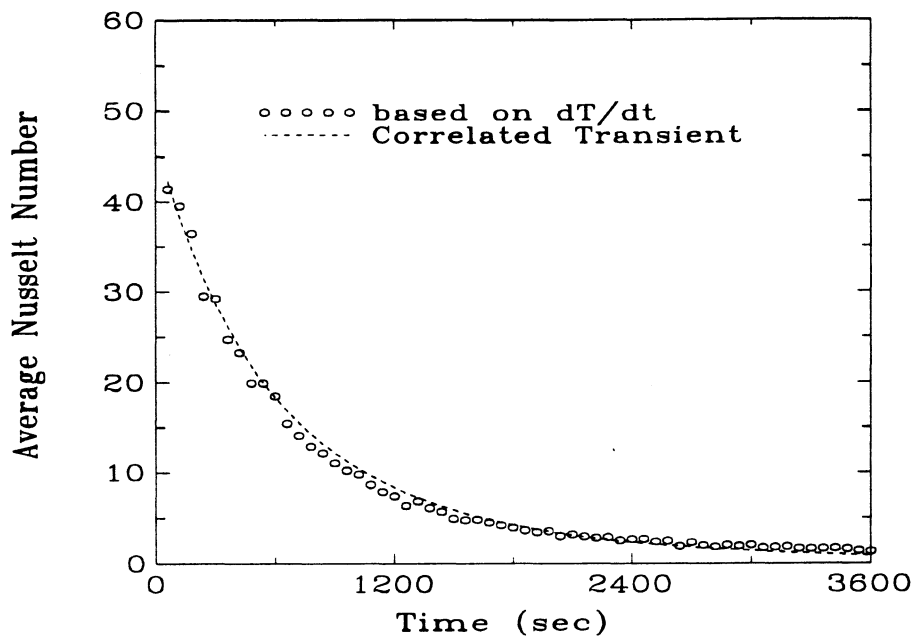


Figure 4.28: Measured and correlated (Equation 4.31) average Nusselt numbers (one minute time average results over three runs).

It is also of interest to determine the ability of the correlation given by Equation 4.31 to predict the bulk temperature response. The resulting bulk temperature response, found by integrating Equation 4.31, is compared with the measured bulk temperature in Figure 4.29. The agreement between the measured and predicted bulk temperature is excellent and well within the uncertainty of the bulk temperature measurements (given by the horizontal bars in the figure).

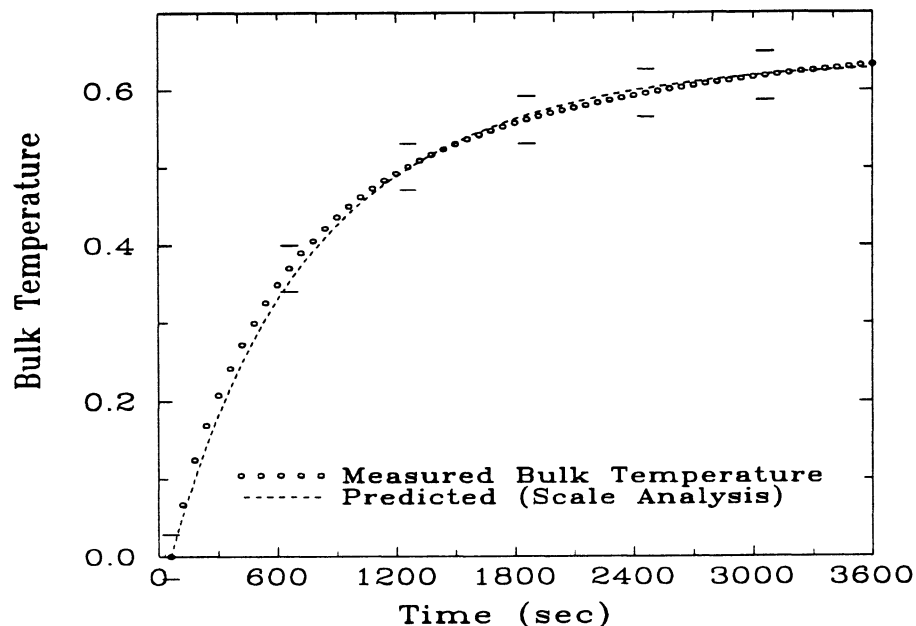


Figure 4.29: Measured and predicted bulk temperature responses including uncertainty bars for measured temperature (one minute time average results over three runs).

## 4.5 Conclusions

An experimental apparatus has been constructed to study the transient heat transfer from a single loop coil tube heat exchanger immersed in water. The source is a copper coil tube with an integral resistance heating element. The enclosure consists of a borosilicate based glass cylinder with acrylic head and base plates. The entire enclosure is insulated to minimize heat loss. Any resultant heat losses are characterized by a power law relationship fitted from cool-down data. The variables monitored during the

experiment include: source temperature, ambient temperature, enclosure bulk temperature, and electrical power supplied to the coil. A new technique for measuring the bulk temperature of fluid in the enclosure has been developed.

The first boundary condition considered is a constant heat flux source. Direct current power is supplied to the heat source and the transient response of enclosure bulk temperature observed. The bulk temperature, based on an energy balance, is also computed. Both the measured and energy balance based bulk temperatures agree within 0.6 C (1.08 F) after six hours of heating. The difference throughout the entire transient is within the error bounds predicted by uncertainty analysis (0.67 C, 1.2 F). The results of the constant current boundary conditions lend confidence in the measurement technique developed to predict the enclosure bulk temperature.

A constant temperature boundary condition is imposed in an effort to validate the two-dimensional numerical computations. A feedback control system is used to maintain the source at "constant" temperature. Both bulk temperature and average Nusselt number (based on measured power and time rate change in bulk temperature) are observed. The measured temporal response of the average Nusselt number is quite different than the response predicted by numerical computations.

A simple shadowgraph flow visualization technique is used to gain a better understanding of the flow field. The visualization technique confirms the existence and time duration of the pure conduction regime as predicted numerically and by scale analysis. The shadowgraphs also showed the influence of a source temperature that is not constant. (The scheme used to control the power to the heat source maintains the source temperature in a range of  $\sim 1.1$  C, 2 F about the setpoint while the actual temperature of the source oscillates about the setpoint.) The shadowgraphs show a dramatic impact of the oscillating

temperature boundary condition on the flow field. The oscillating temperature boundary condition causes a higher degree of mixing in the flow field. The mixing results in a heat transfer profile that appears to decay throughout the entire transient. The parameters identified by scale analysis to correlate the decay period are applied to the observed temporal response of the average Nusselt number. After modifying the single coefficient, excellent agreement is obtained between the observed heat transfer and that predicted by scale analysis.

## References

---

*Measurement Uncertainty*, ANSI/ASME PTC 19.1-1985 Part 1, 1986.

Coleman, H. W., Steele, W. G. Jr., "Experimentation and Uncertainty Analysis for Engineers", John Wiley, (1989).

Hale, G. M. and Querry, M. R., "Optical Constants of Water in the 200 nm to 200  $\mu\text{m}$  Wavelength Region", *Applied Optics*, pp. 555-563, 12(3), (1973).

Keenan, J. H., Keyes, F. G., Hill, P. G., and Moore, J. G., Thermodynamic Properties of Water Including Vapor, Liquid, and Solid Phases, John Wiley & Sons, (1978).

Morgan, V. T., "The Overall Convective Heat Transfer from Smooth Circular Cylinders", *Advances In Heat Transfer*, 11, pp. 199-263 (1975).

Siegel, R. and Howell, J. R., "Thermal Radiation Heat Transfer", *Hemisphere Publishing*, p. 425, (1981).

## **5 Conclusions and Recommendations**

This chapter draws conclusions on the work performed during the course of this research effort. In addition, recommendations are made for directions and areas of focus in future research related to this topic.

### **5.1 Conclusions**

A primitive variable formulation of the finite element method is used to simulate two transient source driven enclosure problems: a vertical flat plate in a rectangular enclosure and a coil tube heat exchanger in an cylindrical enclosure. Although the geometries are quite different, the temporal response of heat transfer from the sources are similar. The temporal heat transfer is characterized by three distinct regimes: pure conduction, quasi-steady, and decay. In each geometry scale analysis techniques are used to predict the time duration of the pure conduction and quasi-steady regimes. Scale analysis is also used to identify parameters to correlate the decay period.

In addition to the numerical computations, physical experiments were undertaken to validate the results obtained from simulation of the cylindrical enclosure geometry. Measured quantities include: heat exchanger surface temperature, ambient temperature, enclosure bulk temperature, and average Nusselt number.

#### **5.1.1 Vertical Flat Plate In A Rectangular Enclosure**

The temperature field in the rectangular enclosure with a vertical flat plate maintained a strong level of stratification throughout the entire transient. Early in the transient, a plume of heated fluid rises above the vertical plate and eventually reaches the top of the enclosure. After reaching the enclosure top, the plume drives across the cavity to the

sidewalls. The remainder of the charging transient is characterized by a front of warm fluid spanning the width of the enclosure and moving from the top of the enclosure to the bottom.

The temporal behavior of the velocity field is relatively acquiescent. The velocity field is characterized by a single clockwise rotating vortex which initially forms just above the heated plate. The structure of the flow field remains essentially unchanged with only the center of the vortex moving near the plate as the velocities peak and then away from the plate as the velocities decay.

The heat flux results are characterized by three distinct regimes: pure conduction, quasi-steady, and decay periods. Scale analysis techniques successfully predict the time duration of the pure conduction and quasi-steady regimes. The viscous flow solutions compare well with the limiting cases of pure conduction and infinite medium solutions at early and middle portions of the transient, respectively. Scale analysis techniques are also used to identify a grouping of parameters that allow the decay period to be correlated with a single constant for the entire range of Rayleigh numbers considered.

The length of the heated plate relative to the enclosure size has an influence on the heat transfer results. The enclosure must be at least one and one half times as large as the plate length in order for a quasi-steady regime to be established. As the enclosure size becomes larger, relative to the heated plate, the quasi-steady regime is maintained for a longer period; however, all enclosures eventually reach the end of the quasi-steady regime as the temperature in the enclosure begins to rise significantly and the heat transfer begins to decay.

### 5.1.2 Coil Tube In A Cylindrical Enclosure

The temperature field in the cylindrical enclosure geometry is much more complicated than in the rectangular enclosure geometry. The temperature field develops with a mushroom shaped plume rising above the coil tube source. The plume tends to oscillate back and forth above the heat source with thermals of warm fluid occasionally being ejected from the sides of the mushroomed plume. Very little stratification is induced in the enclosure throughout the transient. The enclosure temperature distribution could be described as somewhere between fully mixed and fully stratified.

The velocities in the cylindrical enclosure are also much more complex than in the case of the rectangular enclosure. Initially, counter-rotating vortices form on either side above the coil tube source. There is a relatively strong zone of fluid flow down the core of the enclosure. The core flow penetrates to the base of the enclosure early in the transient; however, the flow in the core flow also reverses direction and moves upward. This is believed to be caused by inertial effects coupled with oscillating behavior of the heated plume rising above the coil tube source. In the region above the heat exchanger, there are both clockwise and counter-clockwise eddies being formed and dissipated throughout the transient.

Interestingly, the heat flux response is analogous to the rectangular enclosure case. Although the two geometries are drastically different, the same heat transfer regimes exist and the same analysis techniques apply. The heat transfer results early in the transient compare well with pure conduction solutions. The quasi-steady regime is in good agreement with the heat transfer from a long horizontal cylinder in an infinite medium. Scale analysis techniques are used to identify a group of parameters to correlate the decay

period with a single constant for all ranges of Rayleigh numbers considered.

### **5.1.3 Experimental Analysis**

An experimental apparatus is developed to study the transient natural convection from a single coil tube heat source in a cylindrical enclosure. Measured variables include: source surface temperature, ambient temperature, enclosure bulk temperature, and average Nusselt number from the source. Both constant heat flux and constant temperature source boundary conditions are considered.

The primary purpose for using the constant heat flux source boundary condition is to validate the bulk temperature measurement technique. A constant direct current supply of energy is provided to the heat source and the temporal response of bulk temperature is observed. The bulk temperature measured and bulk temperature based on an energy balance compare within 1.08 F (0.6 C) after a six hour heating period. The measured and energy balance based bulk temperatures are in good agreement throughout the entire transient. The constant heat flux results lend confidence in this new bulk temperature measurement technique.

The motivation in considering the constant temperature source boundary condition is validation of the numerical computations. The numerical computations consider the same cylindrical geometry in a two dimensional axi-symmetric configuration. The measured temporal response of the average Nusselt number does not agree with the numerically predicted response. Flow visualization techniques lend insight into explaining the differences between the measured and computed heat transfer response. The author believes the primary reason for the difference in the heat transfer responses is due to fluctuations in the source temperature about the set point and the three dimensional

character of the experimental flow. The fluctuations in the source temperature causes a greater degree of mixing in the enclosure. The higher degree of mixing prevents the heat transfer response from maintaining the plateau indicative of the quasi-steady regime; therefore, the measured heat transfer response appears to decay from the initial condition. A grouping of parameters identified to correlate the decay period is applied to the measured heat transfer response. After modifying the single coefficient in the parameter grouping, excellent agreement is found with the measured temporal response of the heat transfer. The agreement with the predicted bulk temperature (found by integrating the correlated heat transfer) and the measured bulk temperature is excellent as well.

## **5.2 Recommendations**

After completing the investigation of transient heat transfer from sources in enclosure, the author would like to make recommendations for future both numerical and experimental work.

### **5.2.1 Vertical Flat Plate In A Rectangular Enclosure**

The computational domain in the rectangular enclosure with a heated vertical flat plate geometry assumed a line of symmetry coincident with the plane of the plate. The symmetry assumption reduces the computational domain in half; however, there are potential problems arising from the symmetry assumption. First, the flat plate source position is limited to the center of the cavity (in the horizontal direction). Second, the line of symmetry will not allow the computations to capture any oscillating phenomena of the heated plume rising above the plate. Finally, the computational domain neglects all end effects (in the depth direction) by assuming two-dimensional behavior.

The first recommendation in addressing the limitations of the symmetric geometry is to extend the domain to include the entire two-dimensional enclosure. Forgoing the symmetry assumption will allow investigation into the existence of oscillating behavior in the rising thermal plume above the plate. Simulating the entire enclosure will also allow the source position to be varied to off-center positions. The plate could be located near a sidewall to observe the effect of the bounding near wall on the heat transfer and fluid flow from the plate. Does the region between the plate and sidewall become stagnant when the plate is positioned very close to the wall? What is the penalty in the overall heat transfer? Do the same temporal heat transfer regimes exist?

### **5.2.2 Coil Tube In A Cylindrical Enclosure**

In considering the location and configuration of the heat source, flow stability questions arise. The numerical computations performed for this geometry assumed axis symmetric fluid flow and heat transfer. The basis for this assumption arises from the boundary conditions on the enclosure (adiabatic) and the source (isothermal). A logical extension of this dissertation is to extend the computations to include the third dimension. With the same boundary conditions, do convection cells form above the heat source in a three-dimensional domain (similar to the cells which form in the classic Bénard stability problem)? If cellular patterns form, how do they influence the heat transfer from the source? Do the cells have an adverse or auspicious impact on the level of stratification in the enclosure during charging?

The parametric studies considered in this investigation should be extended to consider optimizing the heat transfer from the heat exchanger source. The objective is to minimize the time required to charge the enclosure. It is apparent from first principles and the scale

analysis estimates, the coil diameter should be as large as possible and the coil positioned as low as possible in the enclosure. What is not as apparent is the impact on the heat transfer of the near wall on the fluid flow around the source. Does the sidewall or base of the enclosure impede or choke the natural circulation flow around the heat exchanger? Is there a perceivable penalty on the magnitude of the heat flux from the source?

Most thermal storage applications rely on charging the storage volume through fluid-fluid heat exchangers immersed in the enclosure (tank). With this type of storage strategy, there is a significant azimuthal temperature variation on the surface of the heat exchanger due to fluid on the heat exchanger interior losing its energy as it moves through the coil. In this case, the heat transfer and fluid flow from the immerse coil is fully three dimensional. What influence do flow rates on the interior of the heat exchanger have on the heat transfer and fluid dynamic behavior? Can the heat exchanger position be moved to mitigate the effect of the azimuthal temperature variation. For example, can the heat exchanger be tilted such that the "cool" end of the exchanger be positioned lower in the cavity to maintain a maximum temperature difference throughout the transient?

With a three-dimensional domain, it is possible to study the influence of heat exchanger geometry. It would be of interest to investigate the performance of various heat exchanger geometries in charging the storage tank. Does the coil tube heat exchanger perform better than a bayonet type heat exchanger? Are other geometries better suited to charging the storage tank or inducing stratification in the enclosure? What is the effect of tilting the source in the enclosure?

In the context of solar thermal storage, it is desirable to maintain a high degree of temperature stratification in the storage tank. The simulation results indicate that temperature stratification is not being induced in the enclosure; rather, the fluid in the

enclosure is somewhere between a fully mixed and a stratified state. It would prove useful to pursue methods to induce stratification. Inducing stratification may be accomplished by using physical barriers appropriately positioned within the enclosure. For example, a fine mesh screen positioned above and parallel to the coil tube heat exchanger would help to reduce the momentum of upward and downward directed convective currents; thereby, reducing participation of the entire enclosure in the mixing process during charging. The mixing process may also be squelched by positioning a solid barrier in the path of the plume which rises above the heat exchanger. These techniques are expected to induce stratification. A consequence of the stronger stratification is a reduced time to charge the enclosure.

In the current investigation, only an energy charging mode is considered. In actual applications, we are often just as interested in the discharge or simultaneous charge/discharge problem. How long does it take to stratify the tank when charging is "turned off"? What happens when charging resumes? What do the flow and temperature fields look like when we have a second coil to discharge the energy simultaneously when charging? If the energy being discharged = energy charging, what does the "steady" flow and temperature field look like?

The computations were limited to the high end of the laminar regime. In working thermal storage tanks, higher Rayleigh numbers are often encountered which raises questions about turbulent flows. What closure techniques are appropriate to simulate the transient turbulent flow in this geometry? What are the constants in the closure models? These questions should be answered in conjunction with experiments performed in the turbulent range of Rayleigh numbers.

### 5.2.3 Experimental Analysis

A critical component in the experimental analysis is the heat exchanger source. The mathematical boundary conditions imposed on the heat exchanger is a step change in temperature, initially, and a uniform isothermal temperature at all other times. Both conditions are difficult to impose in an experimental setting. The observed initial response of the heat exchanger is a ramped change in source temperature followed by a mildly non-uniform isothermal boundary condition at later times. Steps should be taken to minimize the temperature non-uniformity of the source and accurately measure the average temperature of the source.

The heat exchanger contains a small diameter heating element coiled inside the copper tube by approximately five turns. The non-uniformity of the heat source is due to overlap of the heating element coiled inside copper heat tube housing. The overlap can be reduced by special ordering a slightly shorter length heating element. Temperature non-uniformity may also be minimized by using a different type of heating element. For example, a larger diameter heating element with a single turn could be positioned inside the copper tube and fastened with low temperature solder. The solder will not only fix the heating element position but also increase the thermal communication with the copper tube by eliminating the air void fraction on the tube interior. Another approach to address the temperature non-uniformity is to use a different heating element. If a heating element can be constructed from ferromagnetic material, it is possible to use a magnetic field in conjunction with the ferromagnetic heat source to achieve a constant uniform temperature source. This technique would eliminate blockage effects caused by the support structure associated with the current heat exchanger design.

Precise measurements of the source temperature (heat exchanger) are required to accurately estimate the average Nusselt number. If the heat exchanger temperature is completely uniform, a single point temperature measurement is acceptable; however, if the heat exchanger is not entirely uniform in temperature, an average temperature of the source is desired. In the current configuration, only two thermocouples are used to estimate the surface temperature. A possible method to obtain a true average heat exchanger surface temperature is based on the principles of thermocouples. The heat exchanger surface is copper. If the heat exchanger is plated with a thin layer of dissimilar metal, a thermocouple junction over the entire heat exchanger surface is created. If a T-type of thermocouple is sought, constantan (55% Cu - 45% Ni) would have to be applied to the copper heat exchanger surface. The application of this alloy would probably require a sputtering process; consequently, the cost associated with this approach may be prohibitive. The most cost effective would be a plating process; however, only pure metals can be applied in plating processes. Temperature - voltage relationships for the new "thermocouple" would have to be determined.

Another important factor related to determining the average Nusselt number from the heat exchanger is the electrical power measurement technique. The difficulty arises in trying to measure the true RMS current of the chopped alternating current waveform such that the true power can be found. Measuring the true RMS current of a continuously changing chopped waveform is very difficult. An alternative is to employ direct current as the power source for the heat exchanger. Advantages include: relatively easy and accurate current measurements and reduced electromagnetic noise. The primary disadvantage is the cost of a direct current power supply needed to supply the required voltage (minimum of 240 VDC) to the heat exchanger.

The two largest sources of error in measuring the bulk temperature of fluid in the enclosure are: expansion of the enclosure and non-linearity in the fluid temperature-specific volume relationship. Expansion of the enclosure may be mitigated by selecting materials with extremely low expansion properties. The cylindrical portion of the enclosure was made of Duran<sup>®</sup>. Duran<sup>®</sup> is a borosilicate based glass with moderately low expansion properties. Selecting a glass with a fused silica base will provide extremely low expansion properties. Another source of expansion in the current enclosure construction is the acrylic top and base plates. Thermal expansion in these two components was larger than desirable. Minimum enclosure expansion will be achieved by selecting both the cylinder portion and upper and lower plates with glass having a fused silica base.

Enclosure expansion represents the greatest source of uncertainty in measuring the bulk temperature. Expansion will exist even when employing low expansion fused silica glasses; therefore, identifying techniques to correct the results for enclosure expansion will improve the bulk temperature measurements. A possible method for determining the enclosure expansion is to measure the expansion directly by using strain gages. Assuming the cylinder portion of the enclosure is the largest source of enclosure volume, two-dimensional rosette strain gages can be applied to determine both the vertical and circumferential expansion of the glass. With a direct measurement of the enclosure expansion, the observed fluid volume expansion can be corrected to arrive at corrected bulk temperature estimates.

Two methods are available which would minimize the error associated with a non-linear temperature-specific volume relationship. The first method is to select a working fluid with a linear temperature-specific volume relationship. The second method is to maintain water as the working fluid but limit its use to a narrower temperature range.

Interestingly, the author could not locate any prior investigations on the natural convection heat transfer from a toroid body, similar to the heat exchanger employed here. It would be useful to investigate the heat transfer from the toroid in an "infinite" medium for various radius ratios ( $r_x/R_x$ ). Aside from being an interesting fundamental heat transfer problem, the infinite medium results from the toroid would be the appropriate quantity to compare with the quasi-steady regime heat transfer for the toroid in an enclosure.